Engineering Journal

American Institute of Steel Construction

Second Quarter 2018 Volume 55, No. 2

Engineering Journal

American Institute of Steel Construction

Dedicated to the development and improvement of steel construction, through the interchange of ideas, experiences and data.

Engineering Journal (ISSN 0013-8029) is published quarterly. Subscriptions: Members: one subscription, $40 per year, included in dues; Additional Member Subscriptions: $40 per year. Non-Members U.S.: $160 per year. Foreign (Canada and Mexico): Members $80 per year. Non-Members $160 per year. Published by the American Institute of Steel Construction at 130 E. Randolph Street, Suite 2000, Chicago, IL 60601.

Periodicals postage paid at Chicago, IL and additional mailing offices. **Postmaster:** Send address changes to *Engineering Journal* in care of the American Institute of Steel Construction, 130 E. Randolph Street, Suite 2000, Chicago, IL 60601.

Subscriptions: subscriptions@aisc.org, 312.670.2400

Archives: Search at **www.aisc.org/ej**. Article downloads are free for current members and are avaialable for a nominal fee for non-members.

Behavior of Deep, Wide-Flange Steel Beam-Column Members in Seismic Applications

FRIDA PETTERSSON, GIAN A. RASSATI, JAMES A. SWANSON and
THOMAS M. BURNS

ABSTRACT

This study involves a parametric analytical investigation of the behavior of deep columns with one-sided reduced beam section (RBS) connections for application in special moment frames (SMFs). Earlier studies led to the prequalification of RBS moment connections for column sizes up to W14 sections; however, the use of deeper columns in SMFs would be advantageous because of their ability to economically control drift. Information on deep column behavior using an RBS moment connection is limited, and this study investigates this behavior using a total of 40 assemblies designed according to the 2016 AISC *Seismic Provisions*. Four column sections were investigated—W14×426, W24×192, W27×194 and W30×191—each subjected to five levels of axial load, two levels of panel zone strength, and modeled conservatively without floor slab restraint. The results show that although the twist of the column increases with increasing column depths, all assemblies subjected to load below the column's design axial capacity still exhibited plastic hinge formation in the RBS. Additionally, the results show that for each column section investigated, the magnitude of twist decreases with an increase of the axial load on that section. Results also show that columns fitted with a doubler plate twist more than the corresponding configurations without a doubler plate. The study concluded (1) that increased column depth does not have a negative impact on the behavior of the connection as long as the axial loads in the columns are below 80% of the design capacity and (2) that deep columns can be considered as a valid alternative to W12 and W14 sections that are commonly used for RBS connections in SMFs, as long as they are properly detailed.

Keywords: deep columns, beam-columns, SMF, RBS, panel zone strength.

INTRODUCTION

After the Northridge earthquake in 1994, where damage in welded moment-resisting connections was discovered, numerous new beam-to-column connection details for steel special moment frames (SMFs) were developed (Ricles et al., 2004). One of these was the reduced beam section (RBS) connection, where portions of the beam flanges are trimmed away near the beam ends. The RBS connection forces yielding to occur in the reduced section of the beam, away from the face of the column, which contributes to ensuring the strong column–weak beam behavior that is required for SMFs (Engelhardt et al., 1996).

The SAC project, which investigated the performance of steel moment-resisting frame connections after the Northridge earthquake, mostly focused on the experimental testing of RBS connections with W12 and W14 columns (FEMA, 2000). Columns that are generally stocky are shown to perform well under seismic loading because they preserve their structural integrity at large inelastic deformations (NEHRP, 2011). However, deeper columns are more effective and economical at controlling drift in SMFs but can be susceptible to undesirable buckling behaviors (NIST, 2016). Several deeper column sections were tested in the SAC project, but the tests showed that stability problems occurred when RBS connections were used with deep columns (FEMA, 2000). Weak-axis and local buckling failure modes play a prominent role on deeper, more slender columns, and therefore the test results and conclusions reached based on stocky columns may not be generally applicable. Published research on the behavior of connections to deep, slender columns is limited, thereby requiring a more thorough body of work as was begun recently through a multiyear, federally funded research effort (NEHRP, 2011).

Due to their flexural stiffness, deep columns can effectively control drift in special moment frames (SMFs) while potentially yielding significant cost efficiencies over commonly used stocky column sections. Earlier research found that using a W27 column section in lieu of a W14 column section could result in a material savings of 6 to 8% for a typical 10-story building (Shen et al., 2002).

Because existing research on the behavior of connections to deep columns is very limited, this study presents a parametric analytical investigation of the behavior of deep

Frida Pettersson, MSCE, Tyréns AB, Umeå, Sweden. Email: frida.pettersson@tyrens.se

Gian A. Rassati, Ph.D., University of Cincinnati, Cincinnati, OH. Email: gian.rassati@uc.edu (corresponding)

James A. Swanson, Ph.D., University of Cincinnati, Cincinnati, OH. Email: james.swanson@uc.edu

Thomas M. Burns, PhD, University of Cincinnati, Cincinnati, OH. Email: burnstm@ucmail.uc.edu

Paper No. 2016-05R

columns with a one-sided RBS connection for applications in an SMF. The geometry and boundary conditions of the analytical model were based on experimental tests by Engelhardt et al. (1998) that used a one-sided RBS connection. A total of 40 assemblies were designed according to the 2016 AISC *Seismic Provisions* (AISC, 2016b). Column sections investigated were W14×426, W24×192, W27×194 and W30×191. The columns were subjected to five levels of axial load and had medium or weak panel zone strength. For this study, performed at the University of Cincinnati (Pettersson, 2015), the finite element software ABAQUS (Simulia, 2014) was used to develop high-definition finite element assemblies, which were subjected to a constant vertical load and a monotonically increasing shear/moment combination on the connected beam. The dimensions of the RBS cut complied with the requirements contained in AISC 358, *Prequalified Connections for Special and Intermediate Steel Moment Frames for Seismic Applications* (AISC, 2016a), and the assemblies did not include the lateral restraint provided by a floor slab.

The main objectives of the study are to (1) evaluate the effect of column depth on the seismic performance of connections in SMFs using RBS connections; (2) evaluate the effect of panel zone strength on the seismic performance of RBS connections to deep columns in SMFs, focusing on weak and balanced panel zone strengths; and (3) evaluate the effect of various levels of axial loads on the seismic performance of RBS connections using deep columns in SMFs.

Only connections to the strong axis of the column were included in this study, using RBS connections with a W36×150 beam in each case. The impact of residual stresses on column twist was also investigated for cases with and without doubler plates in column sections.

PREVIOUS RESEARCH

At the University of California, San Diego, Gilton et al. (2000) studied how the performance of RBS moment connections was affected by column depth in experimental and analytical studies. Three specimens were tested with one-sided connections without any floor slab. Two of the tests were ended prematurely because of the twisting and out-of-plane bending of the column. These specimens reached 0.03 radian of plastic rotation without any fracture in the welds before the tests were stopped. During the third test, a brittle fracture developed along the k-line of the column just before a plastic rotation of 0.03 radian was reached. All tested specimens experienced twist in the column, and in order to reduce the torsion of the column, it was recommended that bracing should be provided for the column or near the RBS region in the beam.

Shen et al. (2002) analytically investigated the use of deep columns in SMFs. Their work focused on two major parts. The first part was to conduct pushover analyses of two frames and compare their seismic behavior, where one frame used W14 column sections and the other used W27 column sections. The second part was to analytically reproduce the experiment by Gilton et al. (2000) and investigate the effects of different column depths. Shen et al. also expanded the study to models that used more realistic boundary conditions than those used by Gilton et al. Conclusions from the study were that deep column connections should be able to provide the strength required for prequalified connections if realistic boundary conditions were used, including accounting for lateral and torsional supports of columns at the floor level, provided by floor systems. The authors concluded that the cyclic behavior of an RBS connection to a deep column was similar to the behavior of the same connection with a W14 column when a floor slab was provided on at least one side of the beam. Altogether, the study by Shen et al. could not find any reasons to prevent the use of deep columns in moment frames.

At Lehigh University, Ricles et al. (2004) analytically and experimentally investigated the effect of column depth on the seismic behavior of both cruciform and one-sided RBS connections to deep columns. The project showed that when a floor slab is present, or when adequate lateral bracing is provided, both the twisting of the deep columns and the lateral movement of the beam in the RBS are reduced, and good performance can be achieved with deep columns if the column section satisfies the strong column–weak beam criterion. Other conclusions from the project included the importance of the panel zone strength, where a weaker panel zone increased the potential for a ductile fracture of the connection while stronger panel zones increased the column twist. The authors recommend a balanced panel zone, which can be achieved by using the AISC *Seismic Provisions*. The authors also studied the effect of axial load on the connection behavior, noting the axial load had a very small effect on global behavior and local fracture potential.

In 2006, Newell and Uang (2006) published a report on a series of experimental tests and ancillary numerical analyses on the cyclic behavior of steel columns subject to high axial loads and large drift demands. The finite element analyses indicated that significant local buckling occurred in W27×146 and W27×194 columns at 5% drift under three axial loading schemes ($0.35P_y$, $0.55P_y$, $0.75P_y$). The authors concluded that the cyclic response of W27 columns under high axial loads shows considerably more degradation than W14 columns.

FINITE ELEMENT ANALYSIS

Model Validation

This study used a variation on the modeling procedure presented by Ruffley (2011). This procedure calls for the use of eight-node, solid brick elements with reduced integration

Table 1. Material Data			
Member	**Material**	**Yield/Ultimate Stress (ksi)***	**Plastic Strain**
Column	A572-50	49.9 (y)	0
		74.5 (u)	0.125
Beam W36×150	Unknown	41.4 (y)	0
		58.7 (u)	0.190
Continuity plate	A572-50	52.3 (y)	0
		52.6 (p)	0.00530
		85.9 (u)	0.119
Shear tab PL⅜×6×30	A572-50	52.3 (y)	0
		52.6 (p)	0.00530
		85.9 (u)	0.119
Doubler plate	A572-50	52.3 (y)	0
		52.6 (p)	0.00530
		85.9 (u)	0.119
* (y) = yielding; (p) = stress at the end of plateau; (u) = ultimate stress.			

and hourglass control to create a fine mesh in the connection area up to twice the beam depth away from the connection. Ruffley suggested the use of a progressively coarser mesh for the rest of the length of the beam, as well as for the column away from the panel zone. Considering that this study focuses on the influence of the behavior of the column on the connection response, a finer mesh was created to model the column away from the panel zone as well so that buckling, stress concentrations, and other localized phenomena could be better predicted. To validate the modeling procedure, one of the specimens tested by Engelhardt et al. (1996) was replicated using ABAQUS. Specimen DB2 consisted of a 134-in.-long W36×150 beam connected to a 136-in.-long W14×426 column with a one-sided RBS connection. The material properties reported by the authors were incorporated into the finite element model and are summarized in Table 1. In particular, the yield stress values used for the beam and the column members were recorded in the experiments by Engelhardt (1998), and the remaining material data used in the model were those obtained from Ruffley (2011) as a curve-fit of experimental data on similar material.

The results from the reproduced model were very similar to the experimental results, as can be seen in Figure 1, where the moment versus plastic rotation response of the experiment is compared against the monotonic simulation with excellent results. Additionally, the model showed significant yielding in the flanges and web within the reduced section coupled with buckling failure, which was consistent with the experimental results. An additional comparison was run between models with and without the explicit modeling of the erection bolts in the shear tab. Very minor differences were found, and in order to reduce computational time, the explicit modeling of the bolts was excluded in all subsequent models in this study.

Finite Element Models for the Study

Each of the models that were developed for this study followed the same approach described for the baseline model. The beam and the connection details were maintained identical to the baseline study configuration for all cases, and the parameters used for the study were the size of the column; whether a web doubler plate was provided; and the amount of axial force, varying in 20% increments from $0.2\phi P_n$ to $1.0\phi P_n$. Each specimen was modeled with five external restraints as shown in Figure 2. Lateral bracing was provided near the RBS section and at 84.0 in. from the beam connection [to replicate the experiment by Engelhardt (1998)] and at the beam compression flange outside of the RBS cut, which is an AISC 358-16 requirement for RBS connections. Columns are restrained from twisting freely by the presence of floor slabs and orthogonal floor beams, as well as by their own torsional stiffness; however, after an investigation of different torsional boundary conditions for the column, it was deemed most conservative to leave all torsional rotations free to take place. The column was perfectly pinned at the base, and a vertical roller was provided at the top to allow axial deformations of the column. The tip of the beam was restrained from displacing out-of-plane as well as from twisting.

The column sizes were picked to complement data in previous research and to ensure, whenever possible, the

existence of strong column–weak beam behavior. Initial imperfections were introduced in all column sections based on the application of a linear combination of selected buckling modes for the column such that the fabrication tolerances for out-of-straightness would be upheld. For cases where a doubler plate was used, the panel zone was designed according to the AISC *Seismic Provisions* (2016b). All cases used 1.0-in.-thick continuity plates. Five axial loads levels were investigated: $0.2\phi P_n$, $0.4\phi P_n$, $0.6\phi P_n$, $0.8\phi P_n$ and $1.0\phi P_n$. Although the highest axial load level may seem impractical from a design perspective, it was used for comparative purposes with respect to load-displacement and column twist behavior. For axial loads of $0.2\phi P_n$ and $0.4\phi P_n$, all cases satisfied the strong column–weak beam criterion, while only the W14×426 and W30×191 passed for $0.6\phi P_n$. No case satisfied the strong column–weak beam criterion for axial loads of $0.8\phi P_n$ and higher. Table 2 shows which cases satisfied the strong column–weak beam criterion.

An important parameter in the evaluation of the response of connections to deep columns is the amount of twist that

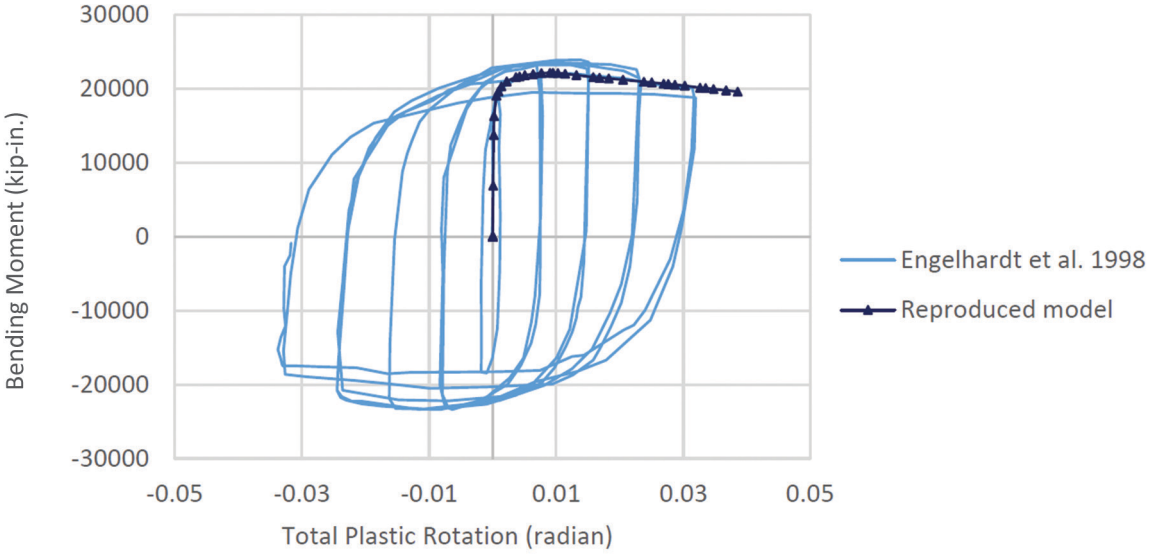

Fig. 1. Bending moment vs. total plastic rotation comparison.

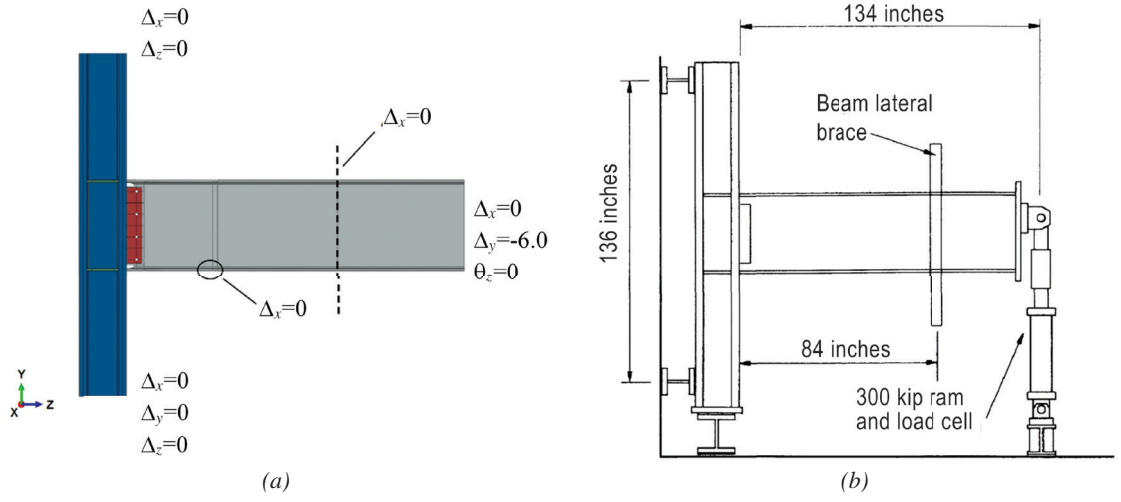

Fig. 2. (a) ABAQUS model with applied restraints and (b) test setup (Engelhardt et al.,1998).

Table 2. Strong Column–Weak Beam Criterion Satisfied				
Load	**W14×426**	**W24×192**	**W27×194**	**W30×191**
$0.2\phi P_n$	Yes	Yes	Yes	Yes
$0.4\phi P_n$	Yes	Yes	Yes	Yes
$0.6\phi P_n$	Yes	No	No	Yes
$0.8\phi P_n$	No	No	No	No
$1.0\phi P_n$	No	No	No	No

the columns undergo, potentially due to the lack of symmetry of the connection. The column twist was measured using the displacements at the tips of opposite column flanges as shown in Figure 3; the displacements were taken at the mid-height of the beam section, and their combination was divided by the diagonal distance between the points. This approach allowed for consideration of the movement of the whole section as opposed to only measuring the twist of the column flange connected to the beam relative to the column web, which resulted in column twist values that were negligible with respect to overall twisting rotations. In order to reduce the influence of the column size on this parameter, the twist angle was then scaled using the ratio of the flexural modulus to the torsional modulus. Scaling the column twist in such a fashion, while causing the parameter to lose its direct physical meaning, allowed a direct comparison of all cases investigated in this study, thus facilitating the process of drawing general conclusions.

In addition to the modeling of imperfections in the column, residual stresses were also considered in order to obtain a more realistic simulation of the column response. An equation for approximating the longitudinal residual stresses is presented in the AWS *Welding Handbook* (2001) and is reproduced here in Equation 1, where σ_x is the longitudinal residual stress in psi, σ_m is the maximum residual stress along the centerline of the weld (*k*-zone) in psi, y is the distance from the centerline of the weld (*k*-zone) in inches, and f is the half-width of the tensile residual stress zone, expressed in inches:

$$\sigma_x(y) = \sigma_m \left[1 - \left(\frac{y}{f}\right)^2\right]^{-\frac{1}{2}\left(\frac{y}{f}\right)^2} \quad (1)$$

Due to the similarity in distribution of residual stresses due to welding and those due to differential cooling/rolling processes, as well as the mathematical appeal of the AWS expression, this approach was used even for the case of a rolled section, likening the fillet weld size to the *k*-zone. Straight-line approximations of the residual stress were entered into the models by defining an initial stress condition for each element along the column length. When comparing this approach to residual stresses experimentally measured by Beedle and Tall (1960), this approach provides slightly higher residual stresses, which ensures a conservative approach.

The impact of residual stresses in the column sections was investigated in a sensitivity analysis that only included the W14×426 and W30×191 column sections subjected to $0.8\phi P_n$ axial load. Cases with and without a doubler plate were included for both column sections. Figure 4 shows the comparison of the load versus displacement graphs for the four cases studied. The graphs show a slight difference in initial stiffness. However, the cases with residual stresses

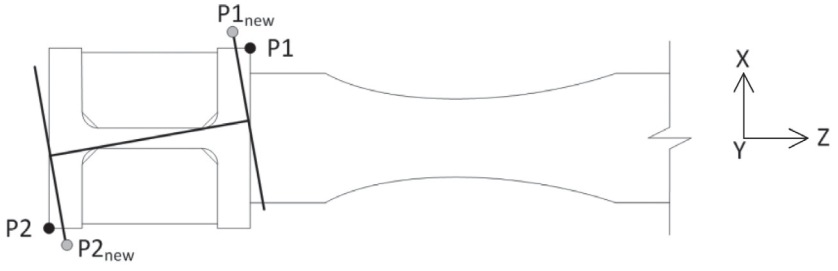

Fig. 3. Column twist.

Table 3. Peak Comparison for Residual Stress Cases				
Column	Residual Stress	Doubler Plate	Max Load (kips)	Beam Tip Displacement (in.)
W14×426	Excluded	No	161.6	2.12
		Yes	161.3	2.03
W14×426	Included	No	161.7	2.23
		Yes	161.1	2.20
W30×191	Excluded	No	160.8	2.39
		Yes	161.1	2.12
W30×191	Included	No	161.3	2.66
		Yes	160.9	2.11

reach a maximum load similar to the one reached in the cases without residual stresses. The peak capacity for all cases is reached within a range of 2.03- to 2.66-in. beam tip displacement as shown in Table 3. The only visible difference in the cases investigated is in the onset of yielding, which takes place sooner when residual stresses are considered but has little influence on the overall response of the connection. This conclusion is also supported by the results in Newell and Uang (2006), where it was shown that the effect of residual stresses on the high-axial load, high-drift demand behavior of columns is negligible.

Figure 5 shows the calculated twist versus story drift for the comparison of cases with residual stresses included and excluded. Note that the scale of the vertical axes for the graphs in Figure 5 is different: The W30 column twists considerably more than the W14; nevertheless, the general trend is noteworthy. For the cases with a web doubler plate, the scaled column twist appears largely unaffected by the inclusion of residual stresses as story drift begins to exceed approximately 2%. Cases without a doubler plate show a slightly more noticeable variation when residual stresses are included. Figure 5 shows that the scaled column twist appears to be smaller in cases that include residual stresses as the story drift begins to exceed approximately 2%.

Because these comparisons showed only minor differences in overall behavior, it was deemed appropriate to exclude residual stresses from the remainder of the study.

RESULTS

All cases with an applied axial load of less than $1.0\phi P_n$ reached similar maximum capacities of approximately 161 kips of applied transverse force and peaked at a similar beam tip displacement of about 2.0 in. as shown in Figure 6. This level of applied force is consistent with what caused the formation of a full plastic hinge in the reduced section in the control model. The only cases that differed were the ones with $1.0\phi P_n$ axial load for the three deep sections, which are represented by the six curves that unload prematurely in Figure 6. In these six cases, the columns underwent local inelastic buckling due to the combined action of shear from the connection and applied axial load before a plastic hinge could fully form in the beam. From the load versus displacement responses, no clear differences are visible among these cases regardless of panel zone strength. It was concluded that different levels of axial load do not affect the response significantly until very high axial loads are applied.

Figure 7 shows the scaled column twist versus the story drift for all cases studied, where the cases with a doubler plate have a solid marker. Three distinct groups of curves can be identified in that plot. The cluster of curves near the horizontal axis represent the response of the connections using the W14 column and show very little twist of the assemblies as drift increases. The intermediate group of curves represents the response of all connections to W24, W27 and W30 columns, in ascending order of sensitivity to twist, for all cases of axial load except the $1.0\phi P_n$ case. This shows that the scaled twist of the column sections increases with an increasing column depth. The six curves associated with large twists are the cases where column inelastic local buckling occurs before a full plastic hinge can form in the beam. The same chart also shows that the twist decreases with increasing axial loads until the design axial load is reached for the deeper column sections.

Furthermore, it was noted that cases with a web doubler plate undergo more twisting than the corresponding cases without a doubler plate. This is due to the combination of loss of symmetry induced by the doubler plate and a reduction in the concentration of plastic strains in cases with a doubler plate, as opposed to larger concentrations of plastic strains in weak panel zones, which result in a less severe local buckling in the RBS region and therefore a reduction in the torsional loading and the column twist. This phenomenon was also noted in Ricles et al. (2004), where the authors

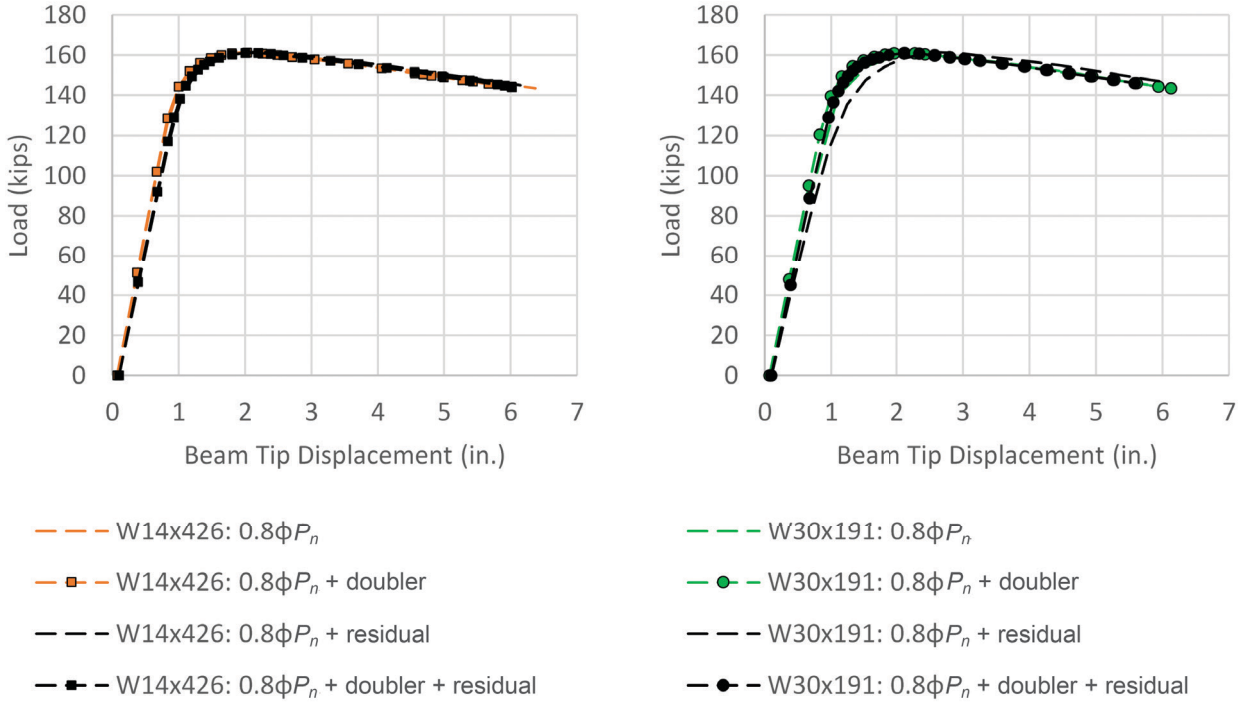

Fig. 4. Load vs. displacement curves for residual stress comparison.

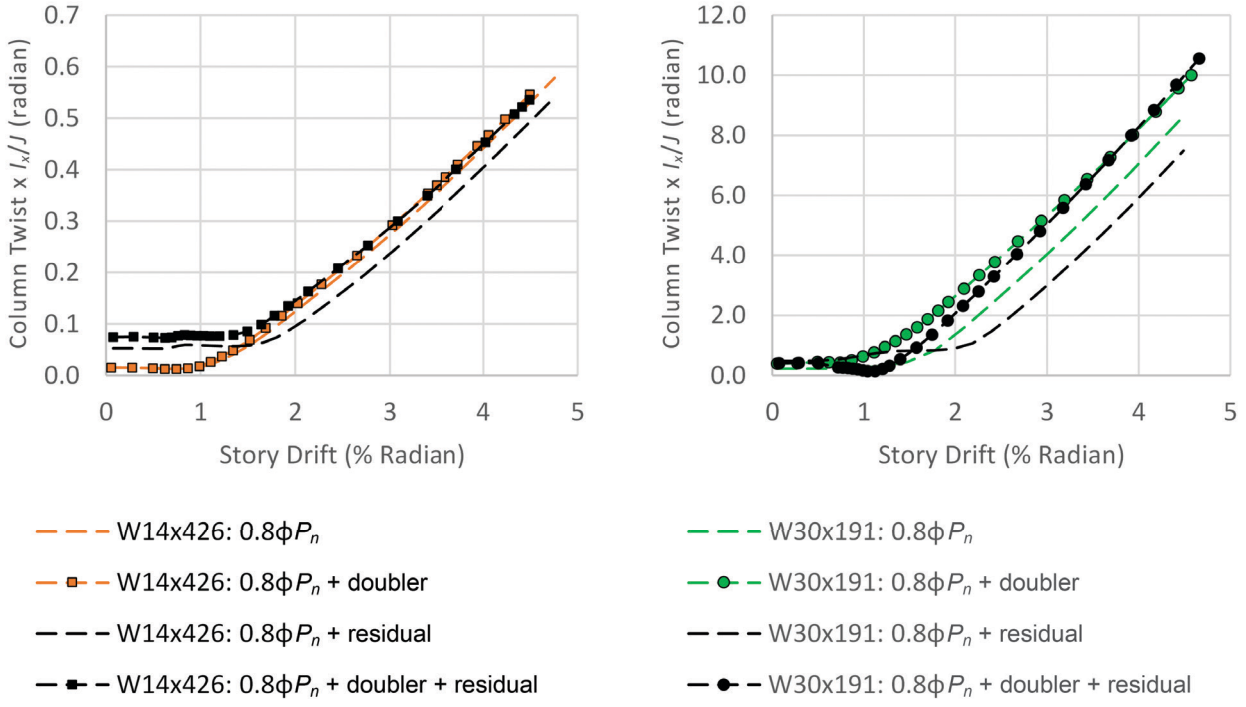

Fig. 5. Scaled twist vs. story drift curves for residual stress comparison.

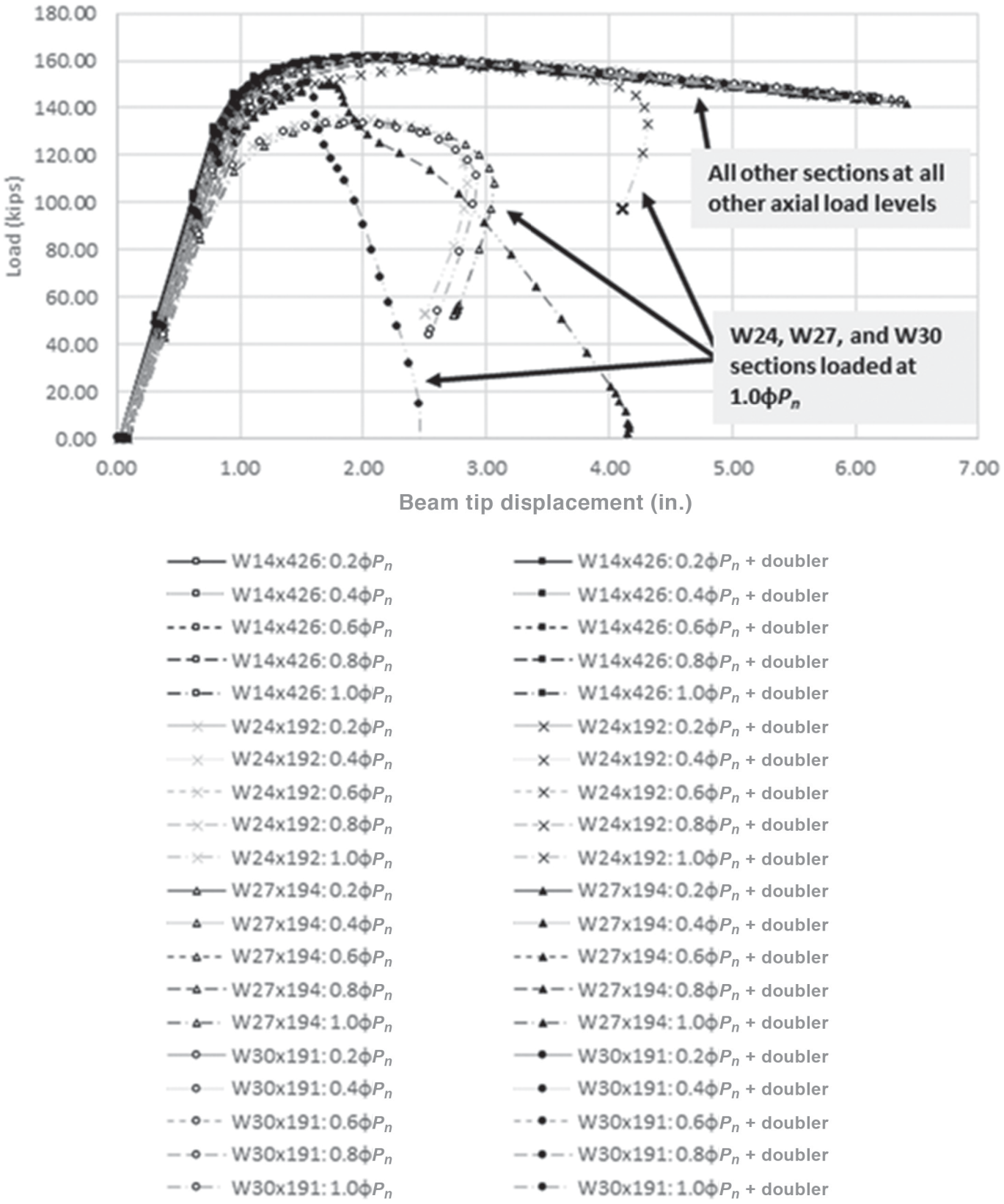

Fig. 6. Load vs. displacement curves for all cases.

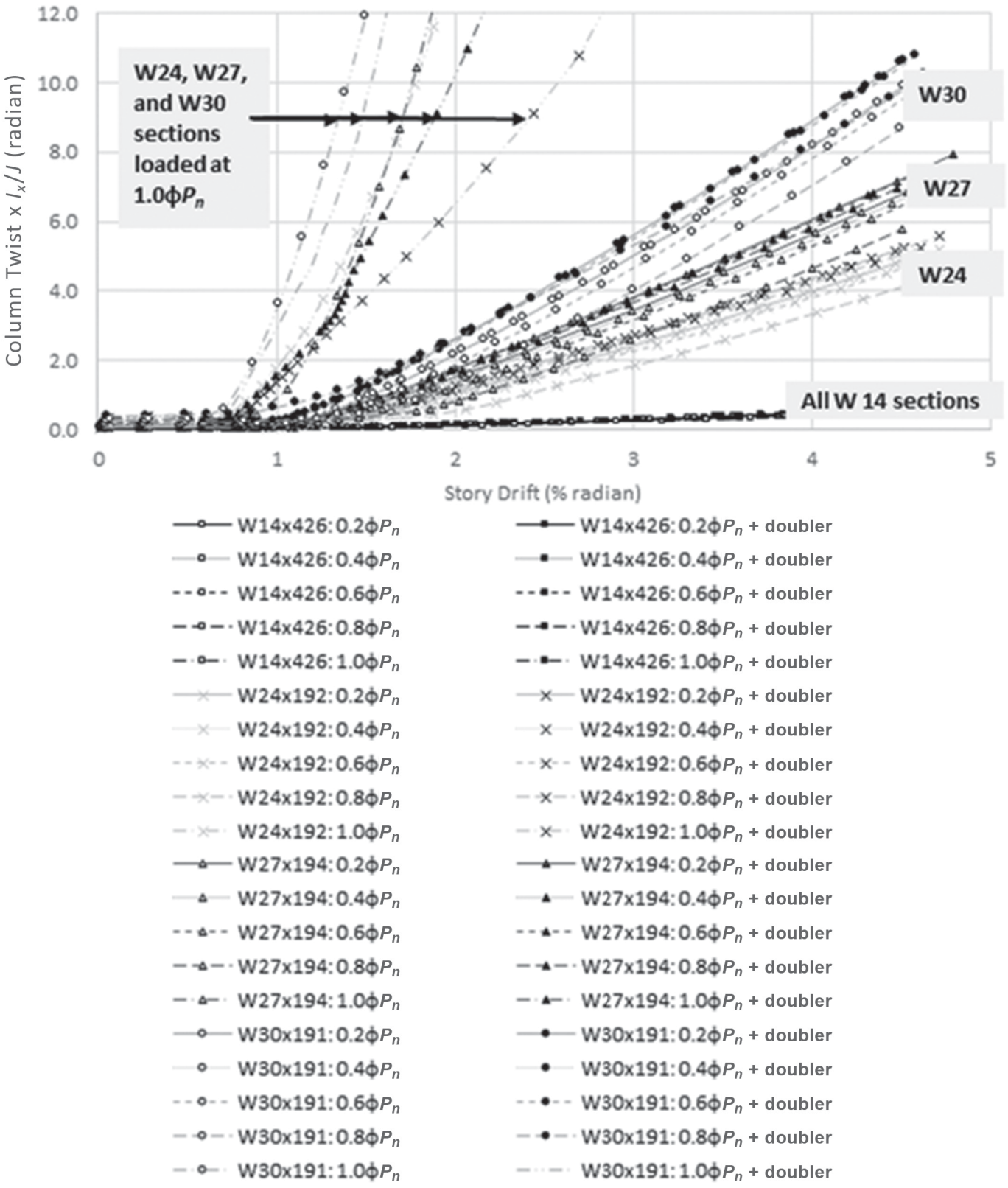

Fig. 7. Scaled twist vs. story drift curves for all cases.

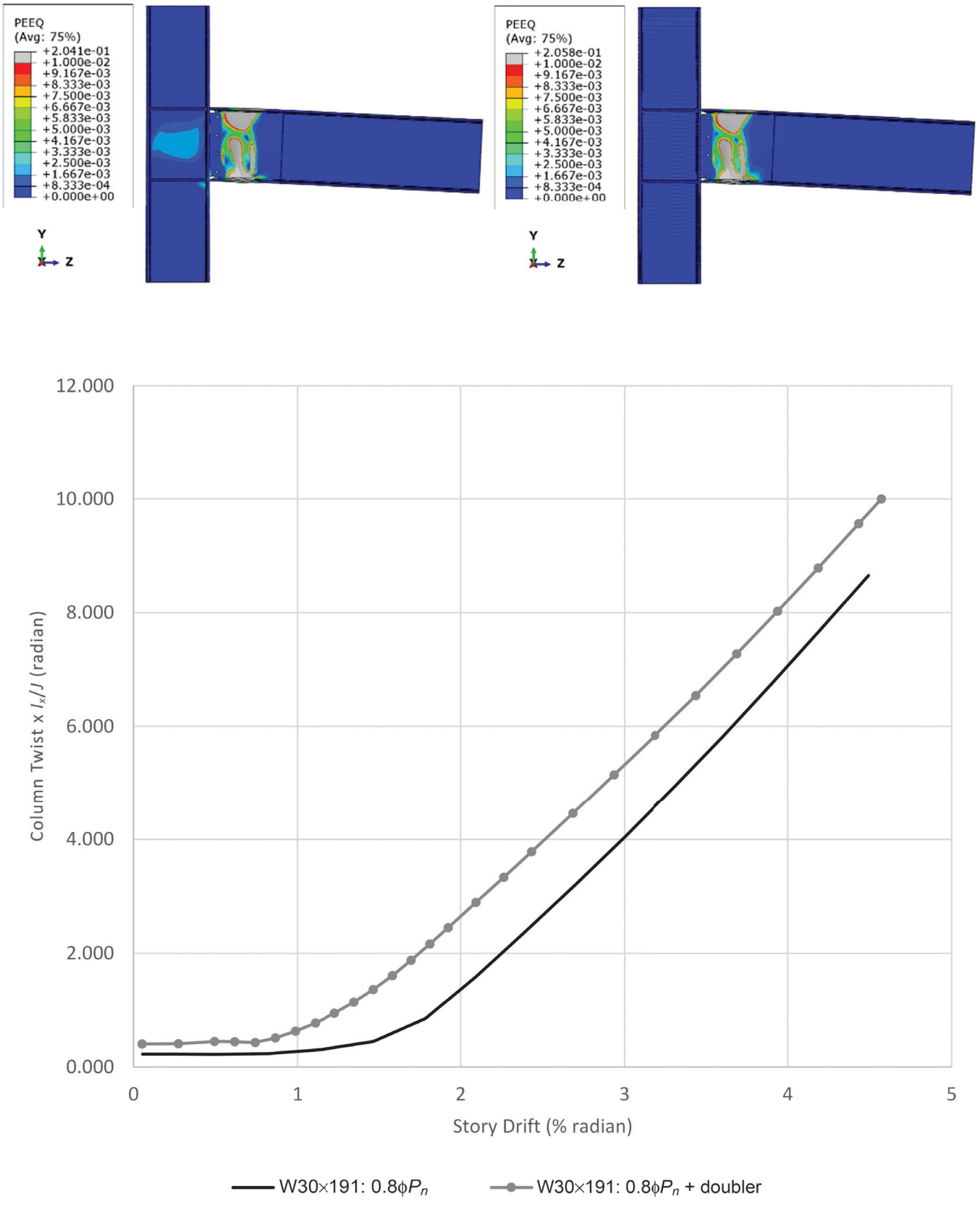

Fig. 8. W30×191 Assembly with 0.8ϕP_n axial load with PEEQ contours and drift vs. scaled twist. Unreinforced column web (top left) and with web doubler plate (top right).

also recommended against an unreinforced panel zone due to an increased potential for a ductile fracture of the connection. To further clarify this point, the difference in yielding demands in the panel zone for the case of a W30×191 column with $0.8\phi P_n$ axial load is shown in Figure 8, where the left assembly shows the unreinforced panel zone case and the one on the right is the specimen with a web doubler plate (which has been hidden for clarity). Figure 8 also shows the effects of the presence of the doubler plate on column twist for the same cases. When the doubler plate is present, the column begins twisting at relatively low drift demands, whereas yielding in the panel zone pushes the onset of twisting to higher demands.

CONCLUSIONS

Based on the results from the finite element models with varying column depths, varying levels of axial load, and medium and weak panel zones, it has been found that:

- Up to axial loads of $0.8\phi P_n$, the column depth does not appear to have any negative impact on the behavior of one-sided RBS connections. Even in the most conservative restraint configuration—without accounting for the presence of framing or of a floor slab—twisting of the column never rises to be a concern, allowing the connected beam to develop a plastic hinge in the RBS region as intended.
- When an axial force equal to the design axial load is applied to a deep column, the beam cannot fully develop its plastic strength as the column undergoes premature inelastic local buckling because of the combination of shear from the connection and applied axial force. Conversely, the W14 section investigated can withstand a force equal to the design axial load while concurrently resisting the shear force and bending moment combination required to develop a plastic hinge in the beam.
- Based on the results shown, it can be concluded that column twisting increases as the column depth increases. Column twisting decreases with increasing column axial loads, and columns reinforced with a doubler plate twist more than the corresponding cases with unreinforced webs. The cases with a reinforced web and low applied column axial forces exhibit the largest twist, while also undergoing the least amount of panel zone yielding. This shows an inverse relationship between panel zone yielding and amount of column twist. However, yielding in the column increases the risk of a ductile fracture in the column and threatens the strength of the connection.
- The presence of residual stresses does not appreciably change the behavior of the columns in the four cases studied under $0.8\phi P_n$ axial load.

This study shows that, especially when considering the restraint against twisting provided by the presence of orthogonal framing elements and floor systems, as well as of floor slabs, the use of deep columns in one-sided RBS moment connections does not lead to undesirable connection responses when column axial forces are below 80% of the column design axial capacity. Therefore, deep columns can be considered as a valid alternative to reduce the overall drift of a SMF, as long as proper detailing is provided to prevent hinging and local instability in columns as described in previous research (Newell and Uang, 2006).

The results presented warrant further analytical and experimental investigations in order to increase the reliability of RBS moment connections to deep columns, especially regarding the behavior of two-sided RBS connections, the effect of column twist on the fracture potential of the connection, the influence of column depth in weak-axis RBS connections, and the use of alternative column sections.

REFERENCES

AISC (2016a), *Prequalified Connections for Special and Intermediate Steel Moment Frames for Seismic Applications*, ANSI/AISC 358-16, American Institute of Steel Construction, Chicago, IL.

AISC (2016b), *Seismic Provisions for Structural Steel Buildings,* ANSI/AISC 341-16, American Institute of Steel Construction, Chicago, IL.

AWS (2001), *Welding Handbook,* American Welding Society, Miami, FL.

Beedle, L.S. and Tall, L. (1960), "Basic Column Strength," *Journal of the Structural Division*, ASCE, Vol. 86, No. ST5, pp. 139–173.

Engelhardt, M.D., Winneberger, T.J., Zekany, A.J. and Potyraj, T.J. (1996), "The Dogbone Connection, Part II," *Modern Steel Construction*, AISC, August.

Engelhardt, M.D., Winneberger, T.J., Zekany, A.J. and Potyraj, T.J. (1998), "Experimental Investigation of Dogbone Moment Connections," *Engineering Journal*, AISC, Vol. 35, No. 4, pp. 128–139.

FEMA (2000), "Recommended Seismic Design Criteria for New Steel Moment-Frame Buildings," FEMA 350, Federal Emergency Management Agency, Washington DC.

Gilton, C., Chi, B. and Uang, C.M. (2000), "Cyclic Response of RBS Moment Connections: Weak-Axis Configuration and Deep Column Effects," Report No. SAC/BD-00/03, University of California, San Diego, CA.

NEHRP (2011), "Research Plan for the Study of Seismic Behavior and Design of Deep, Slender Wide Flange Structural Steel Beam-Column Members," NIST GCR 11-917-13, Gaithersburg, MD.

Newell, J. and Uang, C. (2006), "Cyclic Behavior of Steel Columns with Combined High Axial Load and Drift Demand," Report No. SSRP-06/22, Department of Structural Engineering, University of California, San Diego, CA.

NIST (2016), "Seismic Design of Steel Special Moment Frames: A Guide for Practicing Engineers," GCR 16-917-41 (2nd Ed.), NEHRP Seismic Design Technical Brief No. 2, produced by the Applied Technology Council and the Consortium of Universities for Research in Earthquake Engineering for the National Institute of Standards and Technology, Gaithersburg, MD.

Pettersson, F. (2015), "A Study on the Behavior of Deep, Slender Wide Flange Steel Beam-Column Members in Seismic Applications," M.S. Thesis, University of Cincinnati, Cincinnati, OH.

Ricles, J.M., Zhang, X., Lu, L.W. and Fisher, J. (2004), "Development of Seismic Guidelines for Deep-Column Steel Moment Connections," Report No. 04-13, Lehigh University, Bethlehem, PA.

Ruffley, D.J. (2011), "A Finite Element Approach for Modeling Bolted Top-and-Seat Angle Components and Moment Connections," M.S. Thesis, University of Cincinnati, Cincinnati, OH.

Shen, J.H., Astaneh, A. and McCallen, D.B. (2002), "Use of Deep Columns in Special Steel Moment Frames," Steel Tip Report No. 24, Structural Steel Educational Council, Moraga, CA.

Simulia (2014), *ABAQUS v14 Theory Manual*, Simulia Inc., Providence, RI.

Design Formulation for Critical Buckling Stress of Steel Columns Subjected to Nonuniform Fire Loads

MEHRDAD MEMARI and HUSSAM MAHMOUD

ABSTRACT

Assessing the stability of steel building frames exposed to fire conditions is challenging due to the need to consider elevated temperature properties of steel, nonuniform heating of structural members, and large deformational demands on the frames. There has been significant progress recently in simulating the response of structural members and systems under fire loads using finite element methods. As a result, simple design equations have been developed for predicting the buckling strength of columns under uniform elevated temperature. The equations have been shown to provide accurate predictions and have been adopted by design provisions. There is a need, however, for conducting additional analysis while expanding upon previous work to allow for the development of additional design provisions for column buckling while accommodating varying temperature profiles. This study introduces a framework for conducting stability analyses of W-shape steel columns subjected to demands imposed by fire loads considering nonuniform longitudinal temperature profiles. Results from the analyses show good agreement with available strength design equations of steel columns at ambient and elevated temperatures. An equation is proposed to compute the Euler elastic buckling stress in case of nonuniform longitudinal distribution of temperature. In addition, another equation is proposed to calculate the critical buckling stress of steel columns subjected to nonuniform longitudinal temperature demands. The efficiency of the proposed equations is investigated when two additional nonuniform longitudinal temperature profiles are considered.

Keywords: W-shape steel columns, stability analysis, critical buckling stress, fire, nonuniform longitudinal temperature profile.

RESEARCH BACKGROUND

Significant progress has recently been made in the development of analytical, numerical and experimental tools that can be used to evaluate the response of steel structural members and frames to fire loading. Because columns are key components in resisting gravity loads in a building system, their stability has been the focus of several previous studies (Franssen et al., 1998; Takagi and Deierlein, 2007; Agarwal and Varma, 2011; Morovat et al., 2014). A review of the literature indicates that many experimental studies have been conducted to investigate stability of isolated steel columns under elevated temperatures (e.g., Vandamme and Janss, 1981; Franssen et al., 1998; Ali and O'Connor, 2001). Extensive numerical studies also have been performed to assess the instability of isolated steel columns exposed to fire loads (e.g., Takagi and Deierlein, 2007; Tan and Yuan, 2009; Quiel and Garlock, 2010; Agarwal and Varma, 2011; Agarwal et al., 2014).

Mehrdad Memari, Postdoctoral Fellow, Department of Civil and Environmental Engineering, Colorado State University, Fort Collins, CO. E-mail: Mehrdad.Memari@colostate.edu

Hussam Mahmoud, Associate Professor, Department of Civil and Environmental Engineering, Colorado State University, Fort Collins, CO. E-mail: Hussam.Mahmoud@colostate.edu (corresponding)

Paper No. 2016-18R

Previous experimental fire tests shows that steel columns are typically exposed to nonuniform longitudinal temperature distribution due to the different gas layers in a compartment (Wittheveen and Twilt, 1981; Wang, 2002; Stern-Gottfried et al., 2010; Moinuddin et al., 2011). In addition to experimental work, numerical evaluations conducted by Zhang et al. (2014) demonstrated through simulation of actual fire plumes that the gas temperature for a localized fire are highly nonuniform and that the temperature gradients in steel columns along their length are very evident. Memari and Mahmoud (2014) and Memari et al. (2014) conducted nonlinear finite element analyses to evaluate the performance of steel moment-resisting frames under fire and fire following earthquakes, respectively. These studies highlighted the importance of improving understanding of the buckling response of steel columns subjected to nonuniform longitudinal temperature. All these studies confirmed the presence of thermal gradient along column length and showed that thermal gradient can have a significant negative effect on the response of steel columns exposed to localized fire. The following brief discussion of two of the most recent and relevant studies on steel column buckling under fire (Takagi and Deierlein, 2007; Agarwal and Varma, 2011) will set the stage for introducing the present study for computing the onset of instability of W-shape steel columns under the effects fire loads.

Takagi and Deierlein (2007) evaluated the AISC *Specification* (AISC, 2005) and Eurocode 3 (CEN, 2005) provisions for the design of isolated W-shape steel columns under elevated temperatures that were uniform along the column

length. Numerical models of columns were developed using shell elements, which accounted for residual stresses, local buckling, and material inelasticity. Temperature-dependent material properties were adopted from Eurocode 3 (CEN, 2005). Initial imperfections in the form of out-of-straightness were also considered in the numerical models. It was concluded that the recommendation of the AISC *Specification* (AISC, 2005) to use the ambient temperature design equations in Chapter E for design of axial members under elevated temperatures, modifying only the material properties for elevated temperatures, was highly nonconservative. The outcome of this study was the design equation for W-shape steel columns under uniform longitudinal temperature that currently appears in Appendix 4, Equation A-4-2, of the AISC *Specification* (AISC, 2010; AISC, 2016).

Following the significant work by Takagi and Deierlein (2007), Agarwal and Varma (2011) subsequently conducted comprehensive finite element analyses to evaluate the effects of slenderness and rotational restraints on the buckling response of W-shaped steel columns subjected to uniform elevated temperatures. Shell elements were used to create numerical models of columns because of their ability to capture local buckling and inelastic flexural-torsional buckling and to accommodate the specified residual stress distribution. Initial geometric imperfections, representing out-of-straightness, were included in the models as well as local imperfections. As with the earlier Takagi and Deierlein (2007) study, temperature-dependent stress-strain curves from Eurocode 3 (CEN, 2005) were implemented in the numerical models. This study resulted in new design equations for steel columns with uniform longitudinal temperature distribution considering an equivalent bilinear material behavior. The effects of rotational restraints, provided by continuity with cooler columns above and below the column of interest in a structural frame, were also included in the proposed design equations.

The studies by Takagi and Deierlein (2007) and Agarwal and Varma (2011) provided a solid foundation for evaluating steel columns under fire. These studies showed that the computational efforts associated with analyzing the stability of columns at elevated temperatures were quite substantial. To minimize these efforts, the two aforementioned studies introduced a number of assumptions and simplifications to reduce the number of analyses so that the computational effort for developing the design equations is minimized. For instance, the effects of nonuniform longitudinal temperature, various boundary conditions, and out-of-plumbness imperfection effects were excluded from the studies. Therefore, there remains a need for simple design equations that can be utilized to evaluate the instability of columns under nonuniform longitudinal fire loads while accounting for material inelasticity and geometric nonlinearity associated with column behavior under elevated temperature conditions.

In the current study, a set of equations is proposed for predicting the instability of W-shape steel columns subjected to nonuniform longitudinal temperature profiles caused by fire. To do so, a nonlinear finite element approach is employed that takes into account the temperature-dependent residual stress distribution in steel hot-rolled W-shape sections, initial out-of-straightness and out-of-plumbness in steel members, temperature-dependent material properties, and specified boundary conditions. The results of the finite element analysis (FEA) are first verified against comparison with previous studies. Afterward, equations are proposed for predicting the Euler elastic buckling stress as well as the critical buckling stress as a function of the Euler elastic stress in steel columns subjected to fire loads, represented by nonuniform longitudinal temperature distributions.

ANALYSIS FRAMEWORK

A finite element approach is implemented to predict the onset of instability of steel columns subjected to variable temperature distribution along their length. The Euler-Bernoulli beam theory is employed to consider constant temperature throughout the cross-section of the column. This approach is an extension of studies conducted by Carol and Murcia (1989), Memari and Attarnejad (2010), and Memari et al. (2017). In this method, a finite element is assumed to have a nonuniform longitudinal temperature distribution with T_i and T_j being the nodal temperatures at either end as shown in Figure 1. Because the elastic modulus of structural steel is a function of temperature and degrades at elevated temperatures, the nodal temperature at each end of the finite element will result in temperature-dependent modulus of elasticity $E(T_i)$ and $E(T_j)$ in accordance with Figure 1(a). A linear variation of temperature-dependent modulus of elasticity is assumed along the length of the finite element per Equation 1, in which ζ is determined according to Equation 2. The entire column can be then divided into a sufficient number of elements such that the linear variation along each finite element allows the nonlinear variation along the entire length of the column to be captured.

$$E(x) = E(T_i)\left(1 + \frac{\zeta x}{L}\right) \tag{1}$$

where

$$\zeta = \frac{E(T_j)}{E(T_i)} - 1 \tag{2}$$

In this approach, three sets of equations are considered, including kinematic, second-order equilibrium, and constitutive law equations. In accordance with the deformed state of the finite element, shown in Figure 1(b), the kinematic equations, relating the displacements to the strain and

rotation fields are developed in a matrix and compact form per Equations 3 and 4, respectively, as follows:

$$\begin{bmatrix} -(u_j - u_i) \\ \dfrac{w_j - w_i}{L} - \theta_i \\ \theta_j - \dfrac{w_j - w_i}{L} \end{bmatrix} = \int_0^L \begin{bmatrix} 1 & 0 \\ 0 & 1 - \dfrac{x}{L} \\ 0 & \dfrac{x}{L} \end{bmatrix} \begin{bmatrix} \varepsilon \\ \phi \end{bmatrix} dx \quad (3)$$

$$u = \int_0^L \Omega^T \gamma \, dx \quad (4)$$

where ε and ϕ are the axial strain at the neutral axis of the cross-section and curvature, respectively, and other variables in Equation 3 are shown in Figure 1(b). In Equation 4, u demonstrates a vector of relative displacements and rotations, Ω is a transformation matrix that converts strains to displacements and rotations, and γ is the vector of strains.

The cross-sectional axial force, $N(x)$, and bending moment, $M(x)$, can be determined based on applied nodal axial force, N_i, and nodal moments, M_i and M_j, using equilibrium equations per Equation 5 and its compact form according to Equation 6. To include the second-order (P-δ) effects, a vector of forces due to the deformed state of the finite element, shown in Figure 1(c), is added to the nodal equilibrium equations as shown:

$$\begin{bmatrix} N(x) \\ M(x) \end{bmatrix} = \begin{bmatrix} 1 & 0 & 0 \\ 0 & 1 - \dfrac{x}{L} & \dfrac{x}{L} \end{bmatrix} \begin{bmatrix} N_i \\ M_i \\ M_j \end{bmatrix} + \begin{bmatrix} 0 \\ -N_i w_2(x) \end{bmatrix} \quad (5)$$

$$R(x) = \Omega f + R_2(x) \quad (6)$$

where $w_2(x)$ is the out-of-straightness curvature of the beam-column finite element that causes the P-δ effects. In Equation 6, $R(x)$ is a vector of internal cross-sectional forces developed at the inclusion of second-order effects, $R_2(x)$. The vector f represents the applied nodal forces and moments and Ω is a matrix that correlates the applied nodal forces to those developed internally in the cross-section. It can be seen that the matrix Ω appears in both the kinematic and equilibrium equations. In addition, the cross-sectional strain and curvature must be related to the cross-sectional forces and moments per Equation 7 (compact form, Equation 8) under the assumption that the element responds elastically to nodal forces:

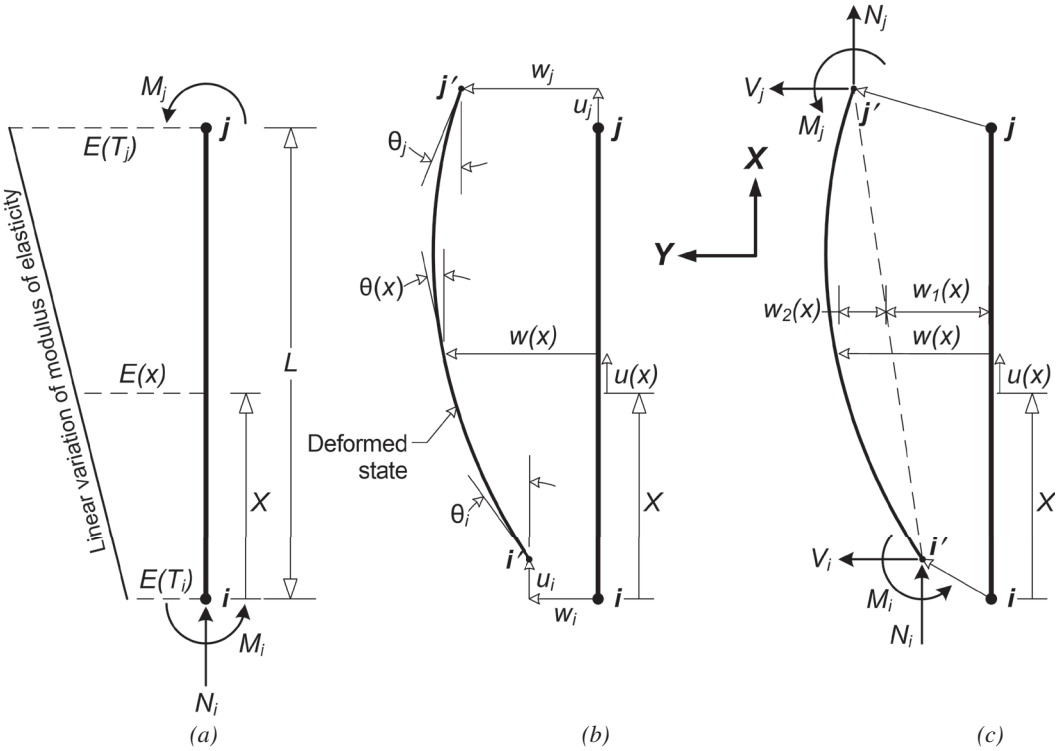

Fig. 1. (a) A finite element subjected to nonuniform longitudinal temperature and three applied external nodal forces; (b) the deformed state of the finite element with all nodal deformation variables; (c) the deformed state of the finite element with all nodal force variables.

$$\begin{bmatrix} N(x) \\ M(x) \end{bmatrix} = \begin{bmatrix} E(x)A & 0 \\ 0 & E(x)I \end{bmatrix} \begin{bmatrix} \varepsilon \\ \phi \end{bmatrix} \tag{7}$$

$$R(x) = k_s(x)\gamma \tag{8}$$

where A and I are the cross-sectional area and moment of inertia, respectively, and $k_s(x)$ is the cross-sectional stiffness matrix. The remaining variables were defined previously. It is noted that the longitudinal variation in the modulus of elasticity, caused by the nonuniform temperature distribution, is reflected in Equation 9 by substituting the longitudinal linear variation of the elastic modulus, Equation 1. This is one of the most important features of the presented framework because a constant modulus of elasticity would imply no variation in temperature along the length. Equation 9 clearly indicates that the section stiffness varies along the length of element as a function of the elastic modulus:

$$k_s(x) = E(T_i)\left[1 + \frac{\zeta x}{L}\right]\begin{bmatrix} A & 0 \\ 0 & I \end{bmatrix} \tag{9}$$

The first-order stiffness and geometric stiffness matrices necessary for the stability analysis can be extracted from the three sets of kinematic, equilibrium, and material law equations by substituting the equilibrium, Equation 6, and constitutive, Equation 8, equations into the kinematic equation, Equation 4. Further details are provided in Memari (2016) and Memari et al. (2017). In summary, the stiffness and geometric stiffness matrices of a beam-column finite element are developed to reflect nonuniform temperature variation along the length of the discrete elements when considering a uniform temperature distribution through the cross-section. Figure 2 shows a schematic description of the finite element model of a steel column under an arbitrary longitudinal distribution of temperature. It is noted that all columns analyzed in this study are divided into 50 identical elements in length. The assemblage of stiffness matrices (first-order and geometric) of all 50 elements resulted in the stiffness matrix of the whole column.

No initial imperfection is introduced to the column in the linear elastic analysis; however, sources of initial imperfection including out-of-straightness, as shown in Figure 2(a), and out-of-plumbness are independently considered in the geometry of the columns in the nonlinear inelastic analysis. The out-of-straightness is modeled by introducing a single sinusoidal curve along the column length such that a maximum displacement of $0.001L_c$—per Commentary Section C2 in the AISC *Specification* (AISC, 2016)—is located at mid-height of column, where L_c is the length of column. The effect of out-of-plumbness is also included explicitly in the finite element analysis. Specifically, an initial out-of-plumbness of $0.001L_c$—below the allowable limit of $0.002L_c$ per Commentary Section C2 in the AISC *Specification*—is assumed at the top of the column, and the lateral nodal displacement for the remaining nodes is calculated assuming a straight column. Following this step, the lateral nodal displacements are multiplied by the applied axial force to compute the corresponding nodal moments, which are then assembled with the applied axial force to form the entire action vector on the column. Figures 2(b) and 2(c) show how the nonuniform longitudinal temperature profile and angle of finite elements are incorporated in formation of stiffness matrices.

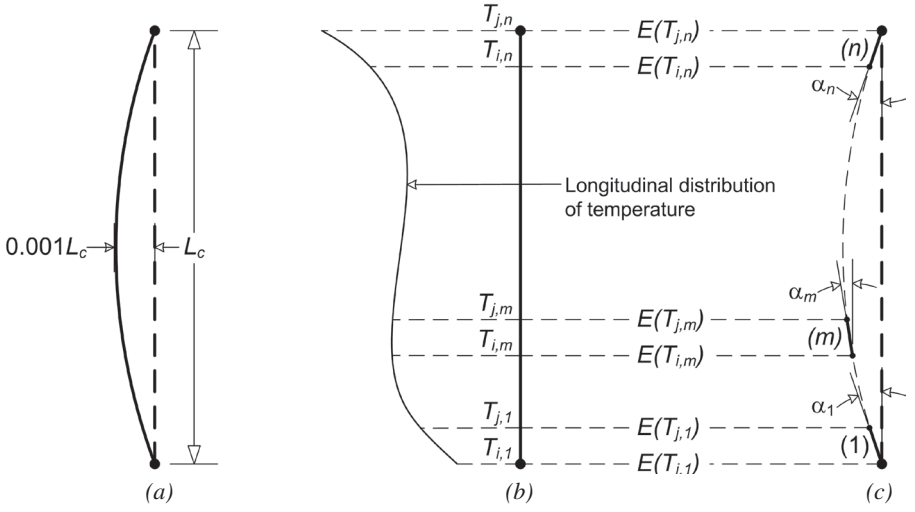

Fig. 2. (a) The inclusion of out-of-straightness initial imperfection with a single sinusoidal curve along the length of column; (b) nonuniform longitudinal distribution of temperature in the column; (c) schematic explanation of finite element analysis considering angle of elements.

Table 1. Longitudinal Variation of Mechanical Properties of Structural Steel According to Nonuniform Temperature Profiles					
			χ_{prop}, Longitudinal Reduction of Mechanical Properties between Cool and Hot Ends of Steel Column (%)		
Profile	Temperature at Cool End, °F (°C)	Temperature at Hot End, °F (°C)	Modulus of Elasticity, ksi	Yield Stress, ksi	Proportional Limit
1	68 (20)	572 (300)	20.0	0.0	38.7
2	392 (200)	932 (500)	33.3	22.0	55.4
3	572 (300)	1112 (600)	61.3	53.0	70.6
4	752 (400)	1472 (800)	87.1	89.0	88.1

The stress-strain curve is assumed to have an elastic–perfectly plastic behavior at ambient temperature, 68°F (20°C). At elevated temperatures, the transition from elastic to inelastic material behavior utilized has a significant effect on the calculated critical buckling stress of steel columns (Takagi and Deierlein, 2007; Agarwal and Varma, 2011). Therefore, the modulus of elasticity is only considered in the elastic buckling analysis, while three mechanical properties of structural steel are considered in the inelastic instability analysis of columns exposed to elevated temperatures: modulus of elasticity, E, proportional limit, F_p, and yield stress, F_y. Temperature-dependent mechanical properties of structural steel are modeled as in Eurocode 3 (CEN, 2005), as shown in Figure 3(a). This material modeling approach was also implemented by Takagi and Deierlein (2007). The variations in E, F_p and F_y as a function of temperature, described by β_E, β_p and β_y, respectively, from Eurocode 3 stress-strain curves are shown in Figure 3(b). In addition, it is noted that the temperature-dependent material properties according to Eurocode 3 inherently capture creep effects.

TEMPERATURE PROFILES

A uniform temperature is assumed across the W-shape steel section in accordance with design recommendations by the AISC *Specification* (AISC, 2016), Takagi and Deierlein (2007), and Agarwal and Varma (2011). The uniform longitudinal temperature profiles will be used for validation analyses. In the current study, four various nonuniform longitudinal temperature profiles are considered in the steel columns as shown in Table 1, which summarizes longitudinal reduction of temperature-dependent mechanical properties from the cool end to the hot end of a steel column. The temperature intervals were selected such that they

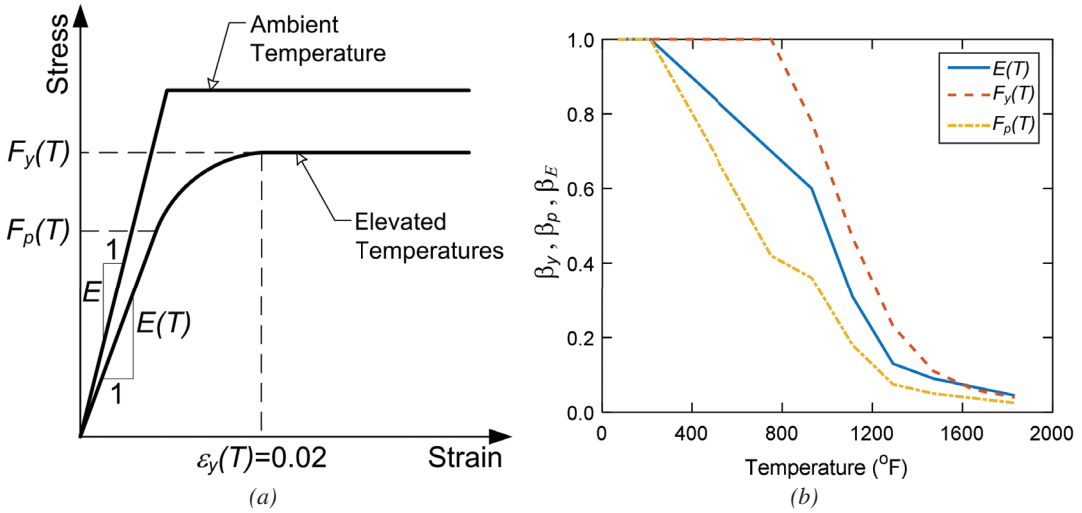

Fig. 3. Schematic explanation of material modeling: (a) Eurocode 3; (b) variations in modulus sof elasticity, yield stress, and proportional limit in accordance with Eurocode 3 (CEN, 2005).

capture various rates of longitudinal change in temperature-dependent mechanical properties of structural steel according to Equation 10:

$$\chi_{prop} = \frac{Q(T_{cool-end}) - Q(T_{hot-end})}{Q(T_{cool-end})} \quad (10)$$

where $Q(T_{cool-end})$ and $Q(T_{hot-end})$ represent temperature-dependent mechanical properties at the cool and hot ends of the steel column, respectively, and χ_{prop} indicates the longitudinal reduction of mechanical properties between the cool and hot ends of the steel column.

These four nonuniform longitudinal temperature distributions are suited for the evaluation of instability of steel columns under different levels of variation in mechanical properties of structural steel as shown in Figure 4. It is emphasized that these nonuniform longitudinal temperature profiles are not the results of any heat transfer analysis.

The pattern of temperature distribution along the length of a column is also an important parameter to be considered. A quick glance into the solution of the governing one-dimentional partial differential equation (PDE) for heat transfer through conduction, Equation 11, shows heat distribution to follow a parabolic function along the length of steel member at time t:

$$\frac{\partial T(x,t)}{\partial t} = \alpha(T)\frac{\partial^2 T(x,t)}{\partial x^2} \quad (11)$$

where T is temperature in °F (°C), x is the coordinate axis along the length of column, and $\alpha(T)$ is thermal diffusivity as a function of temperature. Hence, it is essential to evaluate instability of steel columns with parabolic distribution of temperature along their length. However, because the requirements in code provisions to solve conduction heat-transfer PDE problems and obtain a parabolic distribution of temperature along the length of the member pose difficulties in real applications, a linear longitudinal distribution of temperature will be also considered. This is done to evaluate the difference in the results when using the two different patterns of temperature distribution and assess that the effect of using a linear distribution on the results is within what might be considered acceptable. This will also allow for understanding the difference resulting from using a simplified linear distribution on instability analysis of steel columns under fire. These two patterns of nonuniform longitudinal temperature profiles are shown in Figure 5.

Both parabolic and linear longitudinal distributions of temperature in steel columns can be calculated according to Equation 12, in which η is determined per Equation 13, as follows:

$$T(x) = T_{cool-end}\left(1 + \frac{\eta x}{L_c}\right)^b \quad (12)$$

$$\eta = \frac{T_{hot-end}}{T_{cool-end}} - 1 \quad (13)$$

where x is the coordinate axis along the length of column from 0 to L_c, $T_{cool-end}$ and $T_{hot-end}$ represent temperature at the cooler and hotter ends of the column, and b determines the degree of polynomial such that it is 2 for parabolic and 1 for linear functions. Table 2 summarizes values for η in Equation 12 for all four longitudinal temperature profiles shown in Figure 5.

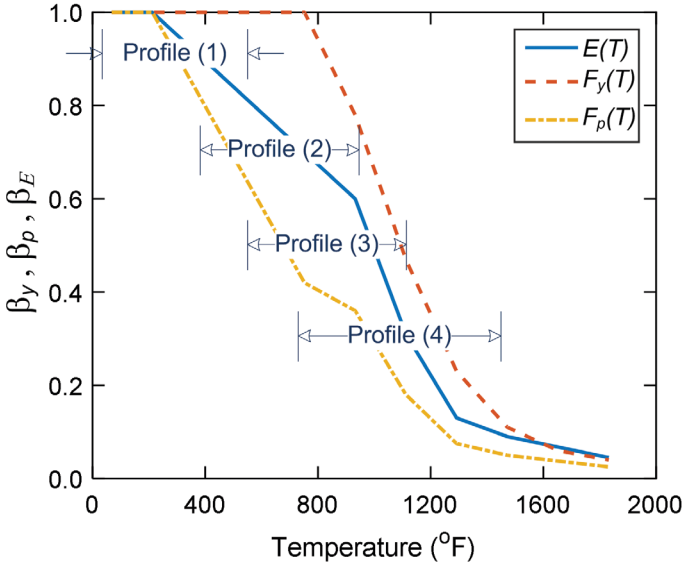

Fig. 4. Temperature intervals in the nonuniform longitudinal temperature profiles.

Table 2. Values of η for Both Parabolic and Linear Temperature Profiles	
Profile	**η**
1	14
2	1.5
3	1.0
4	1.0

LINEAR ELASTIC ANALYSIS

This section presents details of the linear elastic finite element analysis used to obtain the Euler elastic critical stress for a column subjected to nonuniform longitudinal temperature distribution. A modal analysis (eigenvalue analysis) is performed to determine eigenvalues (elastic buckling force) and eigenvectors (elastic buckling mode shapes). Furthermore, the effective length factor of column buckling can be calculated for the first mode shape and higher. To solve the buckling eigenvalue problem, Equation 14 needs to be considered as follows:

$$\left[K_E + \mu K_G\right]\{X\} = \mu\{X\} \tag{14}$$

where μ will return the eigenvalue and $\{X\}$ is the corresponding eigenvector. For the column elastic buckling analysis, K_E represents the first-order stiffness matrix, and K_G is the second-order (geometric) stiffness matrix. A nontrivial solution exists for Equation 14 if and only if

$$\left|K_E + \mu K_G\right| = 0 \tag{15}$$

It is essential to validate both stiffness matrices of a steel column by running an eigenvalue problem with known results. To do so, a uniform longitudinal temperature

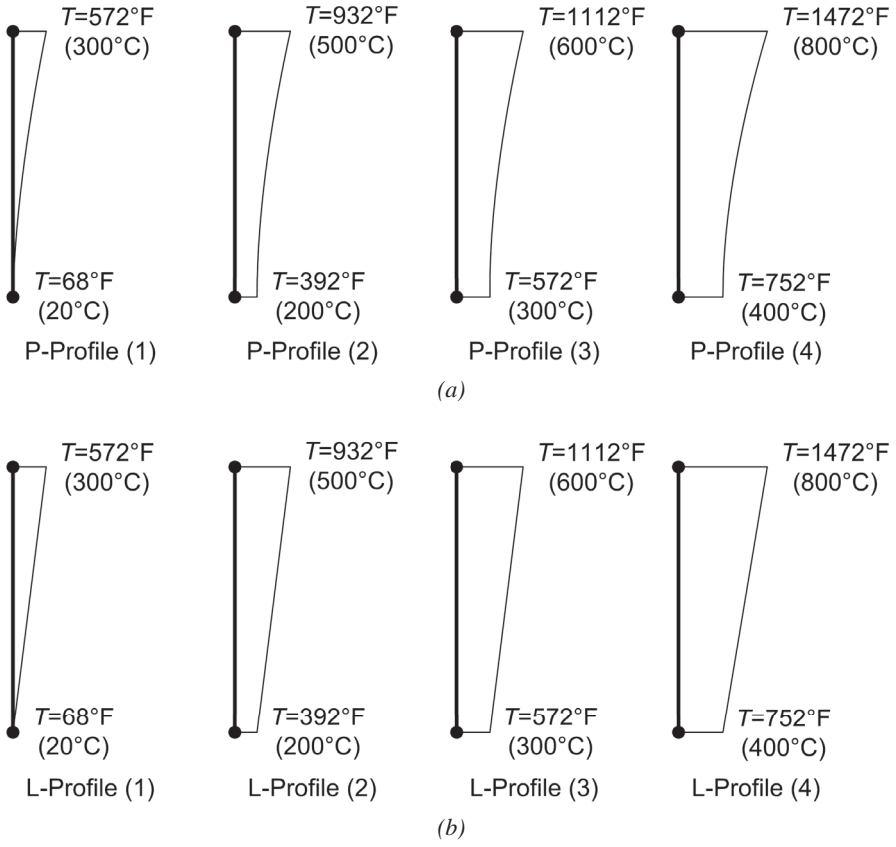

Fig. 5. (a) Parabolic and (b) linear nonuniform distribution of temperature along the length of column.

distribution—for example, 572°F (300°C)—is considered to compute the Euler elastic buckling stress for a column with a pinned-pinned boundary condition. This will allow for direct comparison between the results of the eigenvalue problem and the equation of Euler elastic buckling stress, Equations 16 and 17, as follows:

$$F_e(T) = \frac{\pi^2 E(T)}{\lambda^2} \tag{16}$$

$$\lambda = \frac{KL_c}{r} \tag{17}$$

where $F_e(T)$ is the Euler elastic buckling stress as a function of temperature, $E(T)$ is the temperature-dependent modulus of elasticity, λ is slenderness of column, K is the effective length factor, L_c is the length of column, and r is the radius of gyration of the column section. Figure 6 shows that Euler elastic buckling stress about both strong and weak axes of a W14×90 steel section using finite element analysis is in excellent agreement with the results of the Euler equation (Eq. 16). This validates both the first-order and geometric stiffness matrices generated based on the proposed finite analysis approach in the current study.

In the linear elastic analysis, the effects of both uniform and nonuniform longitudinal temperature profiles, along with boundary conditions on elastic buckling force and mode shapes of steel columns, are assessed. In the context of this study, only the first eigenvalue (Euler elastic buckling force) and the first three eigenvectors (mode shapes) are discussed here. The first three mode shapes of instability of the steel column with various parabolic longitudinal temperature profiles and boundary conditions are shown in Figure 7. It should be noted that the black dashed lines show instability mode shapes when the uniform longitudinal temperature distribution is used. It is observed that nonuniform longitudinal temperature distributions change the instability mode shape of steel column although this change is insignificant in profiles 1, 2 and 3. Table 1 shows that longitudinal reduction of material stiffness (elastic modulus) is up to 61.3% in profiles 1, 2 and 3. However, profile 4 shows a significant change in mode shapes of instability in comparison to those produced using uniform longitudinal temperature distribution or nonuniform temperature in profiles 1, 2 and 3. This can be attributed to the fact that the modulus of elasticity has a longitudinal variation of 87.1% in profile 4. This difference is larger in higher mode shapes of instability for example, the third mode shape shown in Figure 7. In general, the three mode shapes indicate that maximum deflection along column length is shifted toward higher temperature zones (i.e., softer material) while naturally accounting for the effect of boundary conditions.

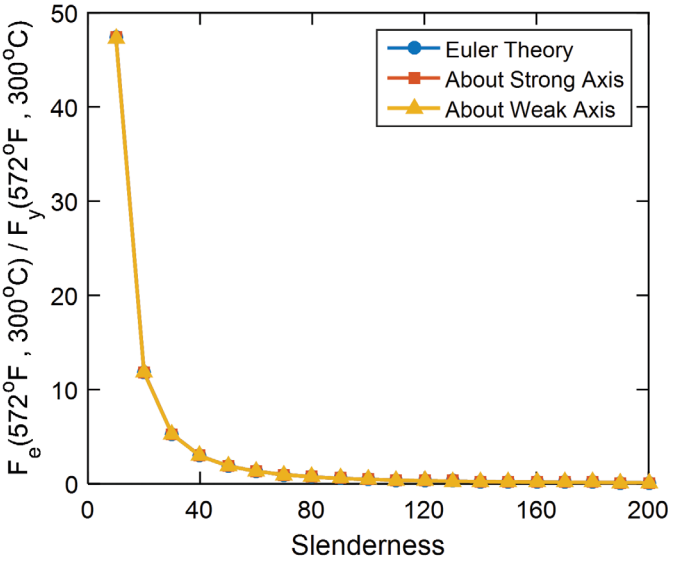

Fig. 6. Euler elastic buckling stress computed by finite element approach presented in this study and the Euler equation.

It is also important to assess the effects of parabolic and linear variation of temperature distribution along the length of column on the mode shapes of instability. Figure 8 shows the mode shapes of instability for both parabolic and linear longitudinal variation of temperature using fixed-fixed and pinned-fixed boundary conditions. Figure 8(a) shows the first three mode shapes of instability for linear longitudinal temperature distribution and fixed-fixed boundary conditions, while Figure 8(b) displays them for a parabolic longitudinal temperature profile and fixed-fixed boundary condition. In addition, Figures 8(c) and 8(d), respectively, show the first three mode shapes of instability for linear and parabolic longitudinal variation of temperature considering a pinned-fixed boundary condition (BC). The results of the analysis show that at least under elastic conditions, parabolic and linear longitudinal variations of temperature make no difference on mode shapes of instability. This will be further investigated in the section discussing nonlinear inelastic stability analysis.

The effective length factor, K, for the first mode shape is calculated based on curvature (second derivative of deformation) change along the length of column. The results of the calculations are summarized in Table 3. The effective length factors listed in the table for uniform longitudinal temperature profiles correspond to the values available in the literature. As shown in Table 3, the effective length factors change slightly in profiles 1, 2 and 3 as expected because the change in mode shapes was minimal due to these profiles. The change in effective length factors is relatively significant in profile 4, which confirms mode shapes observed previously in Figure 7. It is noted that the calculated effective length factors in accordance with Table 3 are in compliance with

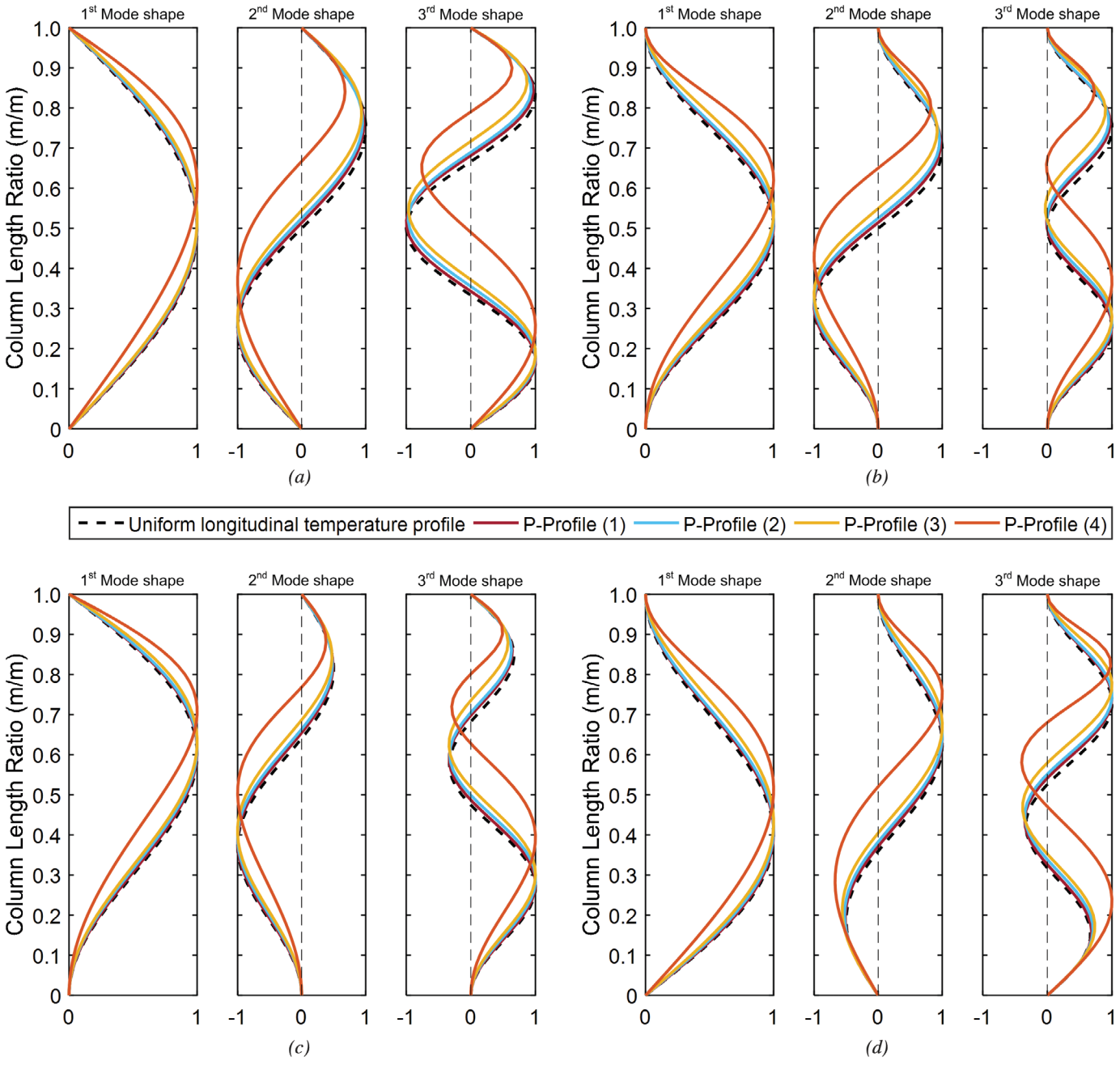

Fig. 7. The first three mode shapes of instability in the steel column with various parabolic longitudinal temperature distributions: (a) pinned-pinned; (b) fixed-fixed; (c) fixed-pinned; (d) pinned-fixed boundary conditions.

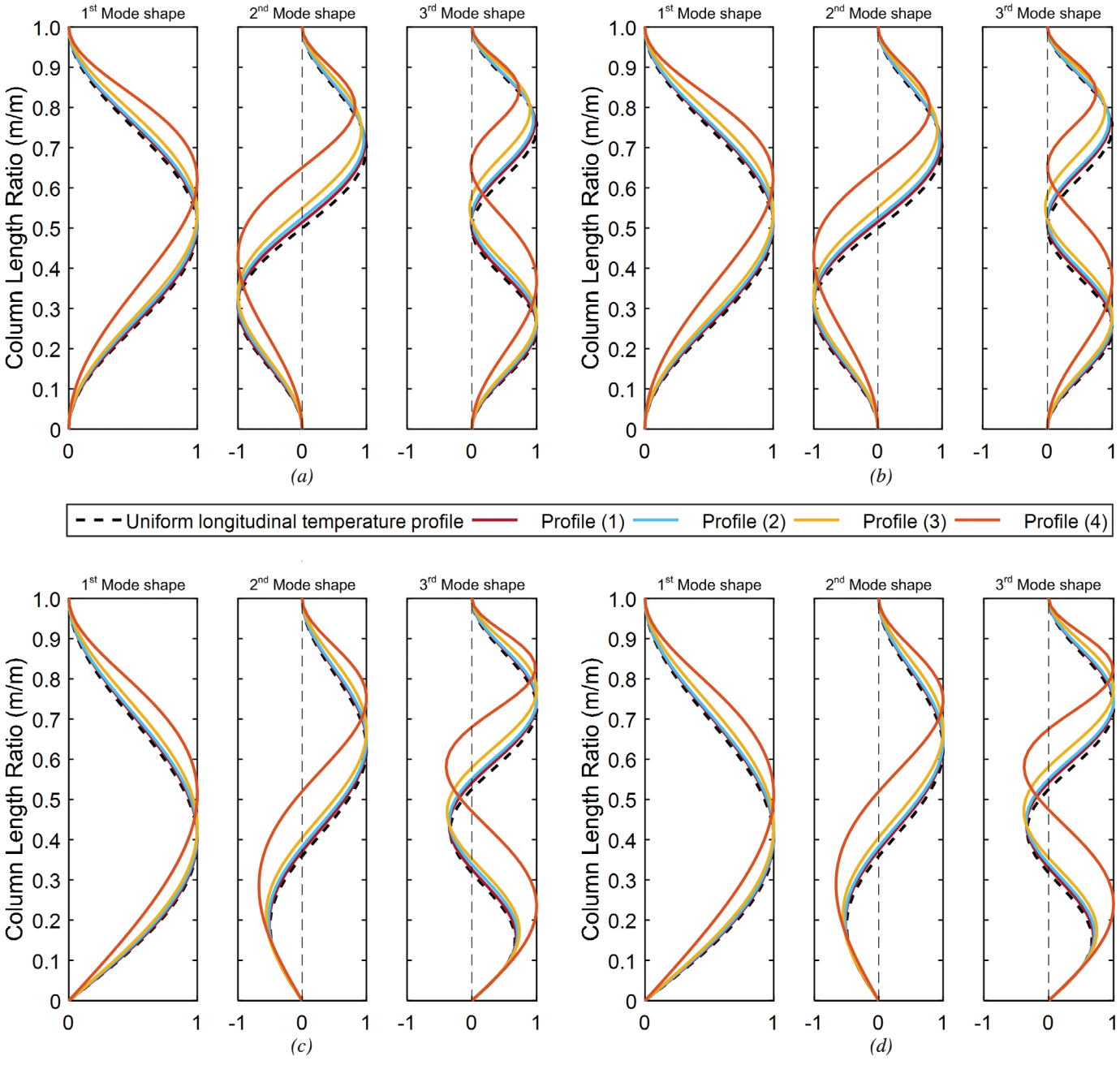

Fig. 8. Comparison between (a) linear temperature distribution and fixed-fixed BC, (b) parabolic temperature distribution and fixed-fixed BC, (c) linear temperature distribution and pinned-fixed BC, and (d) parabolic temperature distribution and pinned-fixed BC.

Table 3. Effective Length Factors, *K*, for Parabolic and Linear Longitudinal Variation of Temperature								
	Pinned-Pinned		Fixed-Fixed		Fixed-Pinned		Pinned-Fixed	
Profiles	Parabolic	Linear	Parabolic	Linear	Parabolic	Linear	Parabolic	Linear
Uniform longitudinal	1.00		0.50		0.70		0.70	
1	1.00	1.00	0.52	0.52	0.70	0.68	0.70	0.70
2	1.00	1.00	0.50	0.50	0.68	0.68	0.72	0.72
3	1.00	1.00	0.54	0.52	0.68	0.68	0.74	0.74
4	1.00	1.00	0.48	0.46	0.56	0.56	0.80	0.80

the expected ratio of elastic buckling stress for fixed-fixed, fixed-pinned, and pinned-fixed to that of the pinned-pinned boundary condition with minimal difference.

The effects of various nonuniform longitudinal temperature profiles are also studied in order to determine an appropriate equation for the Euler elastic buckling stress. This analysis is performed using nonuniform longitudinal linear temperature profiles and a pinned-pinned boundary condition. The results shown in Figure 9 indicate that the Euler elastic buckling stress varies from one profile to another. The ratio of Euler elastic buckling stress to yield stress corresponding to maximum temperature increases from profile 1, with smaller high temperature, to profile 4, with larger high temperature at the boundaries.

In this section, an equation is proposed to predict Euler elastic buckling stress in a steel W-shape column subjected to nonuniform longitudinal temperature distribution. The format of the equation (Equation 18) is identical to that of the Euler elastic buckling equation (Equation 16); however, an equivalent modulus of elasticity (shown in Equation 19) is considered instead of a constant modulus of elasticity to account for nonuniform longitudinal temperature profiles as follows:

$$F_e(T) = \frac{\pi^2 E_{eq}}{\lambda^2} \tag{18}$$

$$E_{eq} = e^{\left[\xi_1 \ln(E_{cool-end}) + \xi_2 \ln(E_{hot-end})\right]} \tag{19}$$

where $E_{cool\text{-}end}$ and $E_{hot\text{-}end}$ are modulus of elasticity at the cool and hot ends of the column, respectively. In addition, ξ_1 and ξ_2 are two unknowns determined by using multilinear regression analysis based on both parabolic and linear longitudinal temperature distributions per Equation 20:

$$\xi_1 = 0.4815, \xi_2 = 0.5226 \tag{20}$$

Therefore, the Euler elastic buckling stress can be predicted according to Equation 21 for nonuniform longitudinal temperature profiles. It is noted that the effective length factor of uniform longitudinal temperature distribution was

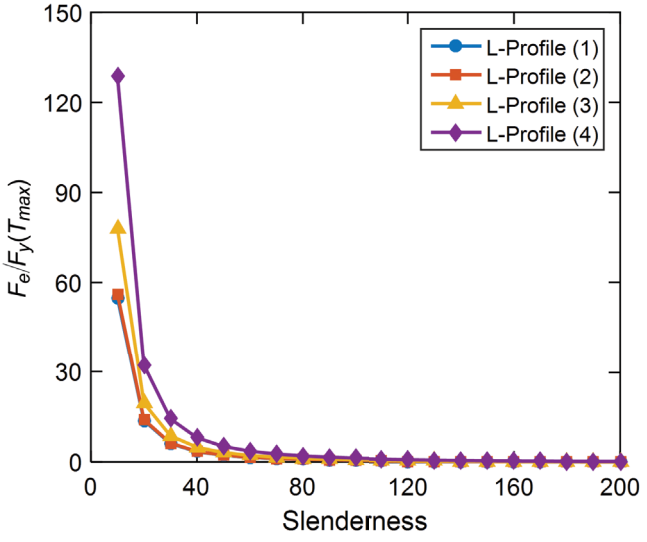

Fig. 9. The effects of various longitudinal temperature profiles on Euler elastic buckling stress.

inherently considered in the regression analysis; therefore, the K factor for ambient temperature must be used in the proposed equation. Figure 10 shows the accuracy of Equation 21 in predicting the Euler elastic buckling stress for longitudinal temperature profiles 1 and 3 when considering pinned-pinned and fixed-pinned boundary conditions, respectively. It is observed that the error in the proposed equation for profile 1 with a pinned-pinned boundary condition is less than 4% in comparison with the results of finite element analysis. In addition, the proposed equation predicts the Euler elastic buckling stress for profile 3 with an error between 13 and 16% compared with the results of finite element analysis.

$$F_e(T) = \frac{\pi^2}{\lambda^2} e^{\left[0.4815\ln(E_{cool-end})+0.5226\ln(E_{hot-end})\right]} \qquad (21)$$

It should be emphasized that the proposed equation was extracted based on the analyses conducted on the nonuniform longitudinal temperature profiles considered in the current study. This equation can also provide a prediction of Euler elastic buckling stress in other cases of nonuniform longitudinal temperature profiles. This will be investigated later by conducting an analysis on a steel column subjected to two other nonuniform linear longitudinal temperature profiles, called profiles 5 and 6.

NONLINEAR INELASTIC ANALYSIS

To determine the critical buckling stress causing column instability, the applied compressive force is increased incrementally until the onset of buckling in the column. A compact W14×90 section, fabricated from ASTM A572-Grade 50 steel, is selected for the nonlinear inelastic analysis. As indicated in the AISC *Specification* (AISC, 2016), columns with slenderness ratio λ less than $4.71\sqrt{\frac{E}{F_y}}$ at ambient temperature are susceptible to inelastic buckling, while columns with slenderness greater than $4.71\sqrt{\frac{E}{F_y}}$ buckle elastically. Therefore, it is important that this distinction be captured in the finite element analysis of the column. This is realized by defining two independent limit states. For the inelastic buckling, the onset of compressive yielding at the cross-section of the steel column, based on the temperature-dependent yield stress at any section, is chosen as the limit state for the inelastic buckling. Furthermore, the calculated stress in the cross-section is influenced not only by the applied load, but also by any residual stresses that might be present, modeled by the residual stress field shown in Figure 11. It is assumed that the maximum thermally induced residual stresses are 10 ksi (~70 MPa) at ambient temperature (Takagi and Deierlein, 2007). The reduction factor for

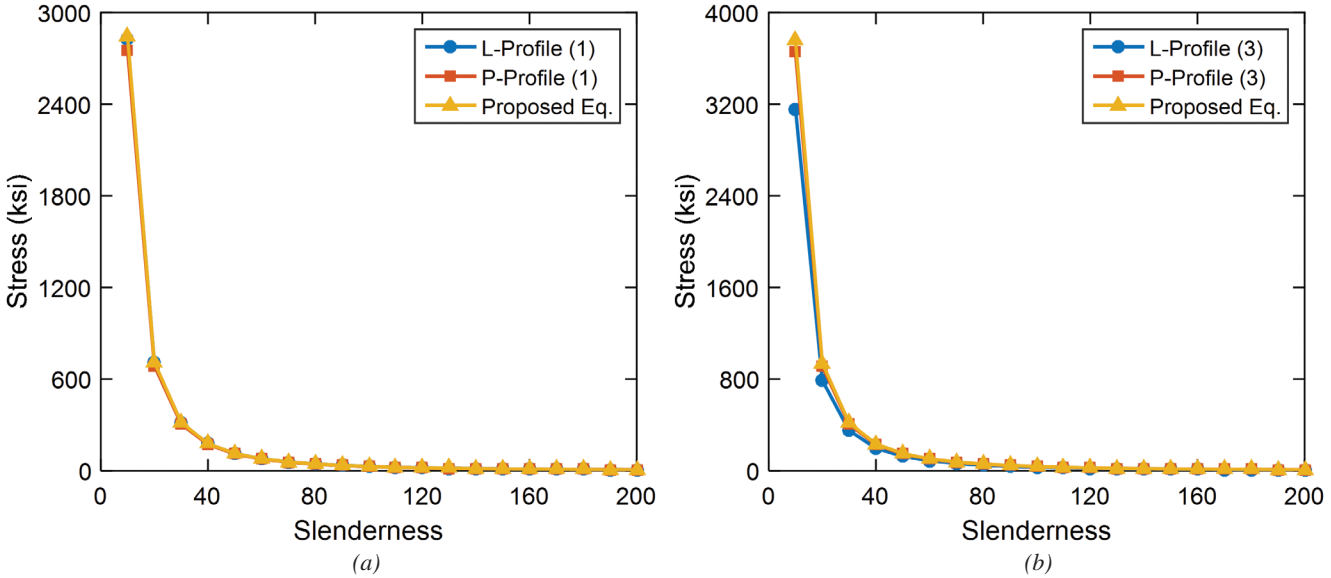

Fig. 10. Euler elastic buckling stress computed by finite element analysis and proposed equation based on (a) pinned-pinned boundary condition in profile 1 and (b) fixed-pinned boundary condition in profile 3.

yield stress at elevated temperatures is also used to reduce the intensity of the residual stresses in the cross section. This assumption was also made by Takagi and Deierlein.

To determine the elastic buckling, the lateral stiffness of the column at a given loading increment is computed; it is then compared to the initial lateral stiffness of the column, which is calculated based on first increment of loading. Initial assessment of the developed formulation indicates that the onset of elastic buckling is reached when the column loses 96% or more of its initial lateral stiffness. A set of analyses is conducted to verify the analysis approach in the current study. This includes examination of buckling of a pinned-pinned column at ambient and uniform longitudinal elevated temperatures using the W14×90 steel column considered previously. Details of the column evaluated are shown in Figure 12(a). The material model utilized is shown in Figure 3 for ambient and elevated temperatures. This matches the assumptions made in the AISC *Specification* (AISC, 2016) for column buckling stress in Section E and Appendix 4 for ambient and elevated temperatures, respectively. Furthermore, while column initial out-of-straightness is considered, the effect of out-of-plumbness is neglected in the verification analysis because it is not reflected in the AISC *Specification* for critical buckling stress of members under compressive forces.

At ambient temperature, the results of the finite element analysis are compared to the column buckling stress, F_{cr}, determined with AISC *Specification* Equations E3 and E4 (AISC, 2016). As shown in Figure 12(b), excellent agreement is observed between the critical buckling stresses computed using finite element analysis and that of the AISC *Specification* design equation. Verification of column stability at elevated temperatures is utilized by the column buckling equations at elevated temperature, proposed by Takagi and Deierlein (2007), available in AISC *Specification* Appendix 4. The comparison is conducted at two temperatures of 752°F (400°C) and 1472°F (800°C). Very good agreement is also observed between the results obtained by finite element formulation and the equation available in AISC *Specification* Appendix 4, as shown in Figures 12(c) and 12(d).

A parametric study is performed on a steel column with pinned-pinned boundary conditions, shown in Figure 13, using four nonuniform longitudinal temperature profiles, according to Figure 5. Figure 14 shows the critical buckling stress of a pinned-pinned steel column subjected to various nonuniform longitudinal temperature profiles. It is observed that there is an insignificant difference between the critical buckling stress of parabolic and linear nonuniform longitudinal temperature profiles. In addition, various nonuniform temperature profiles result in different buckling response with respect to the column slenderness. Figure 14 also shows that the ratio of critical buckling stress to yield

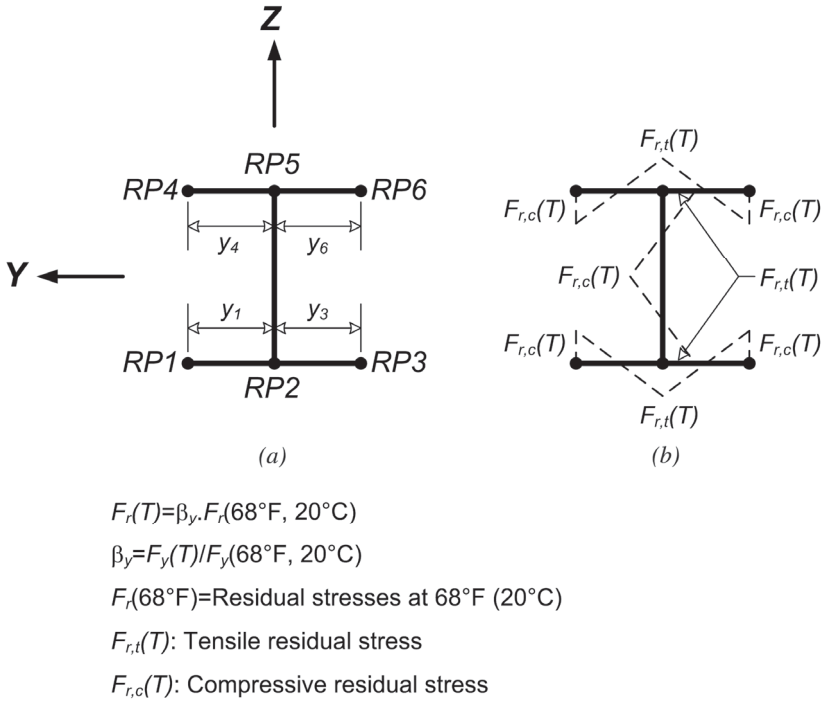

Fig. 11. (a) Six reference points (RPs) and (b) distribution of residual stresses in a W-shape hot-rolled steel section.

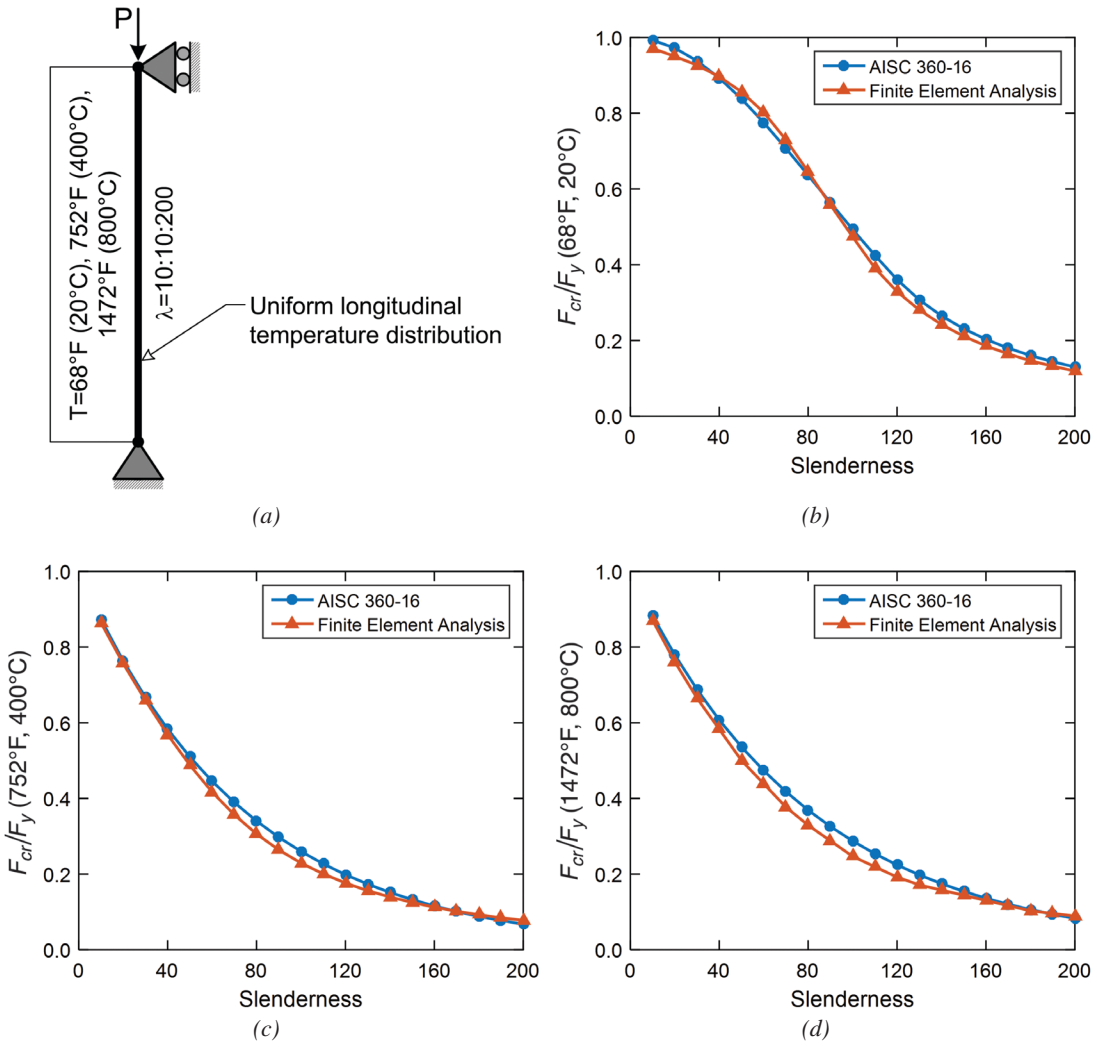

Fig. 12. (a) Steel column subjected to a uniform longitudinal temperature and buckling stress computed using AISC Specification *(AISC, 2016) and finite element analysis at (b) ambient temperature, (c) 752°F (400°C), and (d) 1472°F (800°C).*

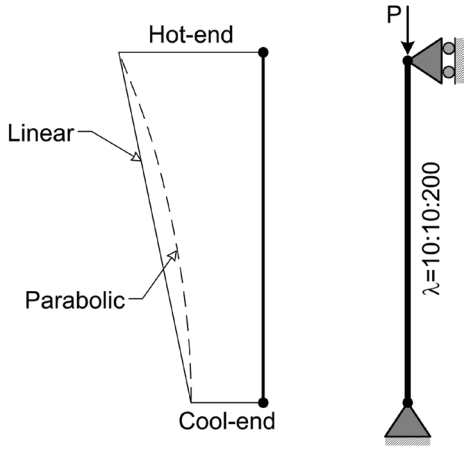

Fig. 13. (a) Nonuniform parabolic and linear longitudinal temperature profiles; (b) pinned-pinned column with various slenderness ratios.

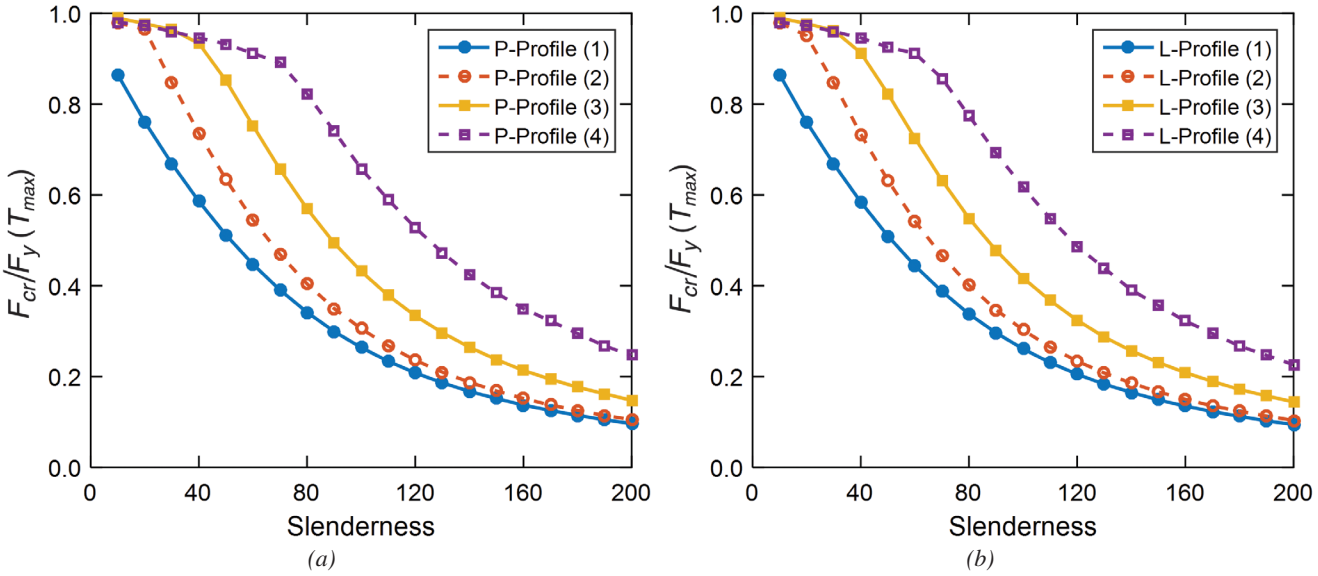

Fig. 14. Critical buckling stress in the pinned-pinned steel column with (a) parabolic and (b) linear nonuniform longitudinal temperature profiles.

stress corresponding to maximum temperature in the column increases with an increase in the maximum temperature of the column as this ratio decreases from profile 4 to profile 1.

PROPOSED DESIGN EQUATION

This section discusses a proposal for an equation to predict the critical buckling stress of steel columns subjected to nonuniform longitudinal temperature profiles. The proposed equation allows structural engineers to estimate the nominal strength of steel columns subjected to fire loads. The proposed equation has a similar format to the current equation listed in AISC *Specification* Appendix 4 (AISC, 2016) proposed by Takagi and Deierlein (2007). Two coefficients, p and q, are added to the current design equation in the AISC *Specification* to consider longitudinal variation of mechanical properties of structural steel shown in Equation 22:

$$F_{cr}(T) = \left[(0.42p) \sqrt[q]{\left(F_y(T_{\max}) / F_e(T) \right)^q} \right] F_y(T_{\max}) \qquad (22)$$

where $F_e(T)$ is calculated according to Equation 21. Two coefficients, p and q, depend on temperature profiles as listed in Tables 4 and 5. The term $F_y(T_{max})$ corresponds to the yield stress at the hot end of the column. In addition, coefficients p and q can be considered as unity for uniform longitudinal temperature profiles to convert Equation 22 to the current available design equation in AISC *Specification* Appendix 4.

As shown in Figure 15, the proposed equation is in

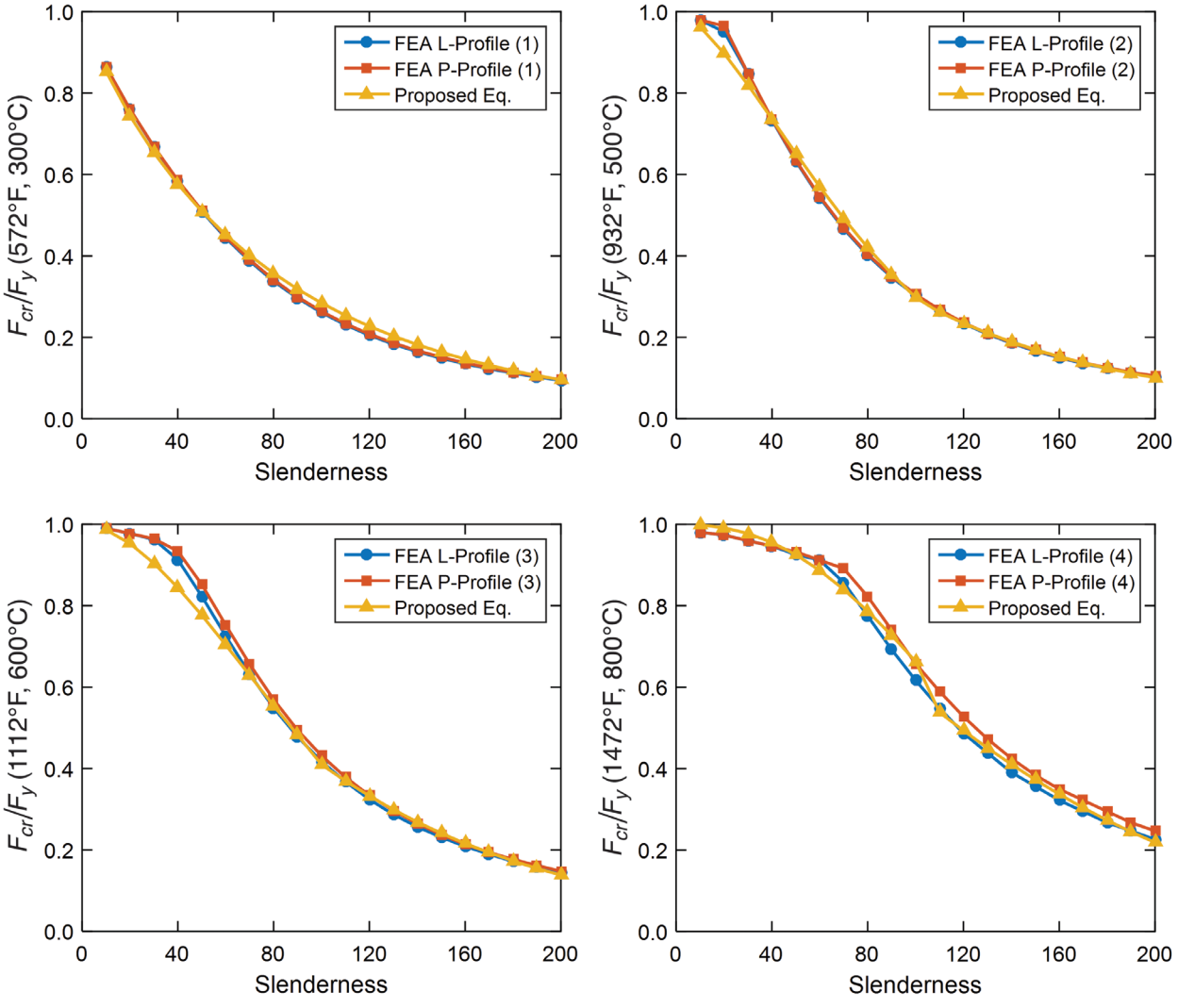

Fig. 15. Critical buckling stress computed by FEA and the proposed equation.

Table 4. p and q Coefficients for $\lambda \le 4.71\sqrt{\frac{E(T_{max})}{F_y(T_{max})}}$			
Profile	**Longitudinal Variation of Yield Stress (%)**	***p***	***q***
1	0.0	0.90	0.90
2	22.0	1.05	1.50
3	53.0	1.30	1.80
4	89.0	1.30	2.40

Table 5. p and q Coefficients for $\lambda > 4.71\sqrt{\frac{E(T_{max})}{F_y(T_{max})}}$			
Profile	**Longitudinal Variation of Yield Stress (%)**	***p***	***q***
(1)	0.0	0.90	0.90
(2)	22.0	0.90	0.90
(3)	53.0	1.18	1.15
(4)	89.0	1.20	1.50

Table 6. Longitudinal Variation of Mechanical Properties of Structural Steel According to Two New Nonuniform Temperature Profiles					
			Longitudinal Variation of Mechanical Properties between Cool and Hot Ends of Steel Column (%)		
Profile	**Temperature at Cool End, °F (°C)**	**Temperature at Hot End, °F (°C)**	**Modulus of Elasticity, ksi**	**Yield Stress, ksi**	**Proportional Limit**
5	68 (20)	1472 (800)	91.0	89.0	95.0
6	932 (500)	1272 (700)	78.3	70.5	79.2

excellent agreement with the results of the finite element analysis (FEA). The comparison between the predicted critical buckling stresses calculated using the proposed equation and the results of the finite element analysis indicates a relative error of less than 10% in all cases. The accuracy of the proposed equation will be evaluated later using two other nonuniform longitudinal temperature profiles—profiles 5 and 6.

ADEQUACY EVALUATION OF THE PROPOSED EQUATIONS

This final section investigates the adequacy of the proposed equations in the current study by considering two new nonuniform longitudinal temperature profiles as shown in Table 6. In profile 5, longitudinal temperature varies from ambient temperature 68°F (20°C) to 1472°F (800°C) in a linear fashion. However, boundaries of profile 6 have ambient temperatures of 932°F (500°C) and 1272°F (700°C), which varies with a linear pattern along the length of the column. These two longitudinal temperature profiles were selected such that profile 5 represents an extreme longitudinal variation of temperature, and profile 6 allows for interpolating all coefficients introduced in the proposed equations. The characteristics of each profile are shown in Table 6. It is noted that the pinned-pinned mechanical boundary condition is also considered in the current analysis according to Figure 13.

A linear elastic analysis is conducted to compute the Euler elastic buckling stress using finite element analysis. In addition, the Euler elastic buckling stress is calculated using Equation 21. As indicated previously, this equation only considers the modulus of elasticity as a function of temperature at both ends of the column. The results of the analysis are shown in Figure 16 for profiles 5 and 6. It is observed that the proposed equation for Euler elastic buckling stress underestimates the stress with an approximate 35% relative error in profile 5. However, the relative error is about

2% in profile 6 when predicting the Euler elastic buckling stress. Because the analysis is elastic, these two errors are constant for all ranges of slenderness for profiles 5 and 6. It is concluded that the proposed equation for the Euler elastic buckling analysis (Eq. 21) demonstrates a good adequacy for nonuniform longitudinal temperature profiles, which falls within the range of nonuniform profiles considered in the current study according to Table 1.

A set of nonlinear inelastic analysis is also conducted to assess the adequacy of the proposed equation for determining the critical buckling stress of steel columns subjected to nonuniform longitudinal temperature profiles. To do so, the critical buckling stress is computed using both the finite element analysis and the proposed Equation 22. It should be noted that coefficients p and q are determined for these two new profiles based on a variation of yield stress using linear interpolation as necessary. The results of analysis are shown in Figure 17 for profiles 5 and 6. It is seen that the proposed Equation 22 underestimates the critical buckling stress for slenderness greater than 100 on average with an

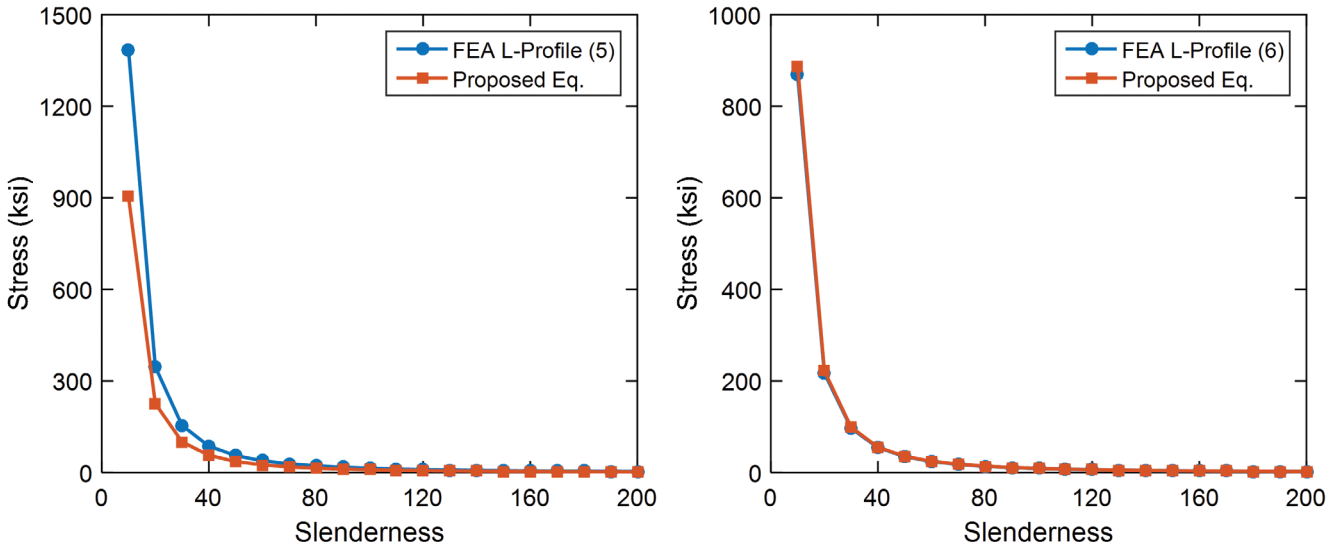

Fig. 16. Adequacy of the proposed equation to predict Euler elastic buckling stress.

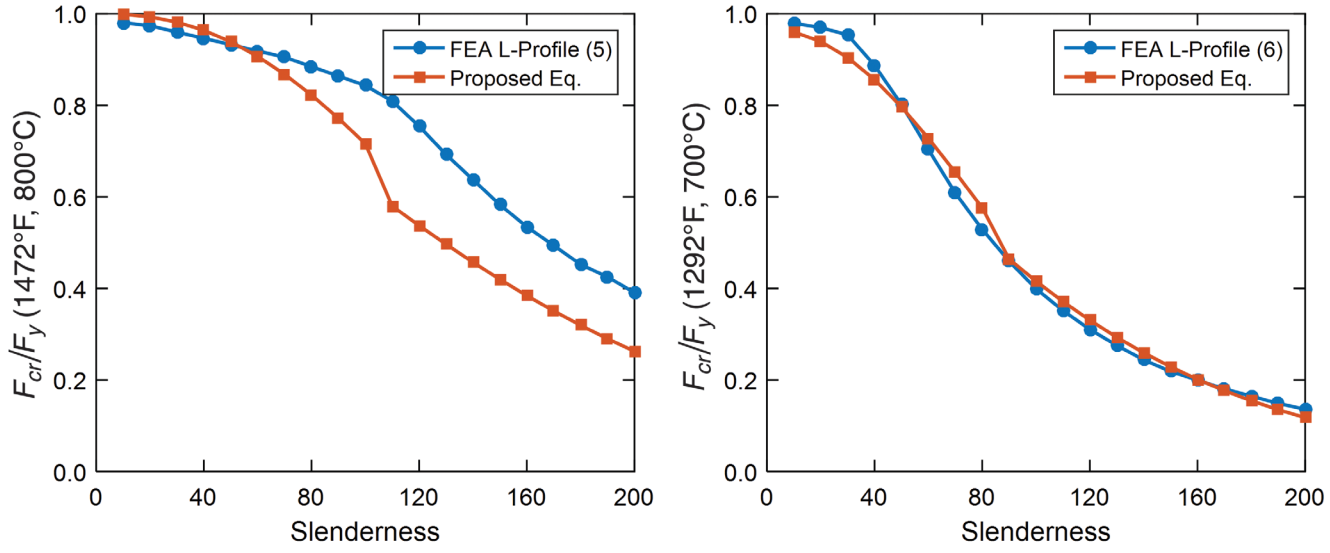

Fig. 17. Adequacy of the proposed equation to predict the critical buckling stress in the steel columns subjected to nonuniform longitudinal temperature profiles.

approximate 30% relative error for profile 5. However, the maximum relative error for predicting the critical buckling stress is about 13% for profile 6, while the average relative error for predicting the critical buckling stress is approximately 5% for all ranges of slenderness. It is concluded that the proposed equation for the critical buckling stress, Equation 22, provides good adequacy for nonuniform longitudinal temperature profiles for the range of nonuniform profiles considered in the current study in accordance with Table 1. Moreover, a comparison between the design equations available in AISC *Specification* Appendix 4 (AISC, 2016) and the one proposed in the current study reveals that the current equation in the AISC *Specification* cannot accurately predict the buckling stress for nonuniform longitudinal temperature profiles if either the average or maximum temperatures are used.

SUMMARY AND CONCLUSION

In this article, a nonlinear finite element approach was introduced for assessing the response of steel columns under fire loads. This methodology included P-δ and P-Δ effects, residual stresses in W-shape hot-rolled steel sections, temperature-dependent mechanical properties of material, various boundary conditions, and nonuniform temperatures along the length of the column. Four various nonuniform longitudinal temperature profiles were considered to allow for evaluating the effects of various rates of change in temperature-dependent mechanical properties of structural steel, including modulus of elasticity, yield stress, and proportional limit.

The following preliminary conclusions can be drawn from the linear elastic analysis:

- The Euler elastic buckling stress of W-shape steel columns, computed by finite element analysis, is in excellent agreement with results of the classical Euler elastic buckling equation. This verified both first-order and geometric stiffness matrices generated based on the finite element method.
- It is observed that the mode shapes of instability change from uniform to nonuniform longitudinal temperature profiles. This change is relatively significant in nonuniform longitudinal profile 4. In addition, the mode shapes indicate that maximum deflection along column length is shifted toward higher temperature zones (i.e., softer material) while naturally accounting for the effect of boundary conditions.
- The effective length factors for nonuniform longitudinal temperature profiles show a small change in profiles 1, 2 and 3 versus uniform longitudinal temperature as expected because the change in mode shapes is minimal. The change in effective length factors is relatively significant in profile 4.
- Insignificant difference is observed between parabolic and linear temperature profiles in the elastic response with respect to Euler elastic buckling stress, mode shapes of instability, and effective length factor.
- An equation is proposed to predict Euler elastic buckling stress in W-shape steel columns subjected to nonuniform longitudinal temperature distribution. The results of proposed equation indicate good agreement with the solution of the eigenvalue problem.
- Adequacy of the proposed equation is assessed using two new nonuniform longitudinal temperature profiles. It is concluded that the proposed equation reveals a good adequacy for nonuniform longitudinal temperature profiles, which falls within the range of nonuniform profiles considered in the present study.

The following conclusions can be drawn from the nonlinear inelastic analysis:

- The initial imperfections, including out-of-straightness and out-of-plumbness, are independently considered in the geometry of the columns analyzed.
- Good agreement is observed between results of the finite element approach and available strength design equations for steel columns at ambient and uniform longitudinal elevated temperatures per the AISC *Specification* (AISC, 2016).
- A design equation is proposed to estimate the critical buckling stress of W-shape steel columns for the case of nonuniform longitudinal temperature profiles.
- The proposed equations show a good agreement with the results of nonlinear finite element analysis. The comparison between the predicted critical buckling stresses calculated using the proposed equation and the results of the FEA indicated a relative error of less than 10% in all cases.
- The adequacy of the proposed equation is assessed using two other nonuniform longitudinal temperature profiles—namely, profiles 5 and 6. It is observed that the proposed equation can have a good adequacy for nonuniform longitudinal temperature profiles, especially within the range of nonuniform profiles studied in the present article.

REFERENCES

Agarwal, A., Choe, L. and Varma, A.H. (2014), "Fire Design of Steel Columns: Effects of Thermal Gradients," *Journal of Constructional Steel Research*, Vol. 93, pp. 107–118.

Agarwal, A. and Varma, A.H. (2011), "Design of Steel Columns at Elevated Temperatures Due to Fire: Effects of Rotational Restraints," *Engineering Journal*, Vol. 48, No. 4, pp. 297–314.

AISC (2005), *Specification for Structural Steel Buildings*, ANSI/AISC 360-05, American Institute of Steel Construction, Chicago, IL.

AISC (2010), *Specification for Structural Steel Buildings*, ANSI/AISC 360-10, American Institute of Steel Construction, Chicago, IL.

AISC (2016), *Specification for Structural Steel Buildings*, ANSI/AISC 360-16, American Institute of Steel Construction, Chicago, IL.

Ali, F. and O'Connor, D. (2001), "Structural Performance of Rotationally Restrained Steel Columns in Fire," *Fire Safety Journal*, Vol. 36, pp. 679–691.

Carol, I. and Murcia, J. (1989), "Nonlinear Time-Dependent Analysis of Planar Frames Using an Exact Formulation—I. Theory," *Computers and Structures*, Vol. 33, No. 1, pp. 79–87.

CEN (2005), *Eurocode 3: Design of Steel Structures—Part 1-2: General Rules—Structural Fire Design*, European Committee for Standardization.

Franssen, J.M., Talamona, D., Kruppa, J. and Cajot, L.G. (1998), "Stability of Steel Columns in Case of Fire: Experimental Evaluation," *Journal of Structural Engineering*, Vol. 124, No. 2, pp. 158–163.

Memari, M. (2016), "Performance of Steel Structures Subjected to Fire Following Earthquake," Ph.D. Dissertation, Colorado State University, Fort Collins, CO.

Memari, M. and Attarnejad, R. (2010), "An Innovative Timoshenko Beam Element," *Proceedings of the 10th International Conference on Computational Structures Technology*, Civil-Comp Press, Stirlingshire, U.K.

Memari, M. and Mahmoud, H. (2014), "Performance of Steel Moment Resisting Frames with RBS Connections under Fire Loading," *Engineering Structures*, Vol. 75, pp. 126–138.

Memari, M., Mahmoud, H. and Ellingwood, B. (2014), "Post-Earthquake Fire Performance of Moment Resisting Frames with Reduced Beam Section Connections," *Journal of Constructional Steel Research*, Vol. 103, pp. 215–229.

Memari, M., Mahmoud, H. and Ellingwood, B. (2017), "Stability of Steel Columns Subjected to Earthquake and Fire Loads," in press, *Journal of Structural Engineering.*

Moinuddin, K.A.M., Al-Menhali, J.S., Prasannan, K. and Thomas, I.R. (2011), "Rise in Structural Steel Temperatures during ISO 9705 Room Fires." *Fire Safety Journal*, Vol. 46, No. 8, pp. 480–496.

Morovat, M., Engelhardt, M., Helwig, T. and Taleff, E. (2014), "High-Temperature Creep Buckling Phenomenon of Steel Columns Subjected to Fire," *Journal of Structural Fire Engineering*, Vol. 5, No. 3, pp. 189–202.

Quiel, S.E. and Garlock, M.E. (2010), "Closed-Form Prediction of the Thermal and Structural Response of a Perimeter Column in a Fire," *The Open Construction and Building Technology Journa*l, Vol. 4, No. 1, pp. 64–78.

Stern-Gottfried, J., Rein, G., Bisby, L.A. and Torero, J.L. (2010), "Experimental Review of the Homogeneous Temperature Assumption in Post-Flashover Compartment Fires," *Fire Safety Journal*, Vol. 45, No. 4, pp. 249–261.

Takagi, J. and Deierlein, G.G. (2007), "Strength Design Criteria for Steel Members at Elevated Temperatures," *Journal of Constructional Steel Research*, Vol. 63, No. 8, pp. 1,036–1,050.

Tan, K.H. and Yuan, W.F. (2009), "Inelastic Buckling of Pin-Ended Steel Columns under Longitudinal Non-Uniform Temperature Distribution," *Journal of Constructional Steel Research*, Vol. 65, No. 1, pp. 132–141.

Vandamme, M. and Janss, J. (1981), "Buckling of Axially Loaded Steel Columns in Fire Conditions," *IABSE Proceedings*, P-43/81, IABSE Periodica 3/1981, pp. 81–95.

Wang, Y.C. (2002), *Steel and Composite Structures: Behaviour and Design for Fire Safety*, Taylor and Francis, Spon Press, New York, NY.

Witteveen, J. and Twilt L. (1981), "A Critical View on the Results of Standard Fire Resistance Tests on Steel Columns," *Fire Safety Journal*, Vol. 4, No. 4, pp. 259–270.

Zhang, C., Gross, J.L., McAllister, T.P. and Li, G.Q. (2014), "Behavior of Unrestrained and Restrained Bare Steel Columns Subjected to Localized Fire," *Journal of Structural Engineering*, Vol. 141, No. 10.

Experimental Evaluation of a Procedure for SMF Continuity Plate and Weld Design

ADEL MASHAYEKH and CHIA-MING UANG

ABSTRACT

The AISC *Seismic Provisions* require that continuity plates in a special moment frame (SMF) welded moment connection be connected to the column flanges by complete-joint-penetration groove welds. Tran et al. (2013) have proposed a design procedure that allows the designer to evaluate the required forces in the continuity plates such that more economical welds (e.g., fillet welds) can be used; the required thickness of the continuity plates also need not be the same as that prescribed in the AISC *Seismic Provisions*. With some minor modifications to the original design procedure, two one-sided reduced beam section moment connection specimens were designed and constructed for experimental verification of the proposed design procedure. To evaluate the effect of potential column kinking on the fillet-welded joints between the continuity plates and the column flanges, weaker panel zones that still satisfied the code requirement were used. Although the AISC *Seismic Provisions* implicitly assume that continuity plates should remain essentially elastic, the continuity plate thickness of one specimen was intentionally undersized to evaluate the effect of continuity plate yielding on the connection performance. Test results showed that using fillet welds is feasible; no damage was observed in these fillet welds, and the connection performance was not affected by the type of weld joints used. The design procedure also indicates the significant effect of in-plane moment in the continuity plate's strength check, especially when shallow columns are used.

Keywords: special moment frames, reduced beam section, continuity plates, complete-joint-penetration weld, fillet weld.

INTRODUCTION

Beam-to-column moment connections play a vital role in the seismic performance of steel special moment frames (SMFs). Following capacity design principles, the intent of AISC 341-16, *Seismic Provisions for Structural Steel Buildings* (AISC, 2016a), is to ensure that system ductility is provided primarily through flexural yielding of beams, flexural yielding of columns at the base, and limited yielding of column panel zones. When beam flanges are directly connected to the column flanges in the strong-axis direction, continuity plates (i.e., transverse stiffeners) in the column, at the beam flange levels, are often needed to transfer the large concentrated beam flange forces to the column. Continuity plates also play an important role in reducing the stress concentration that occurs at the beam flange complete-joint-penetration (CJP) groove welds (FEMA 2000a, 2000b). AISC 341-16 requires that continuity plates be connected to the column flanges with CJP welds; groove welds or fillet welds can be used on the column web side. The requirement of CJP welds is based mainly on available test data, where almost all welded moment connection specimens tested in the United States—especially those tested after the 1994 Northridge, California, earthquake—were fabricated with this weld detail. Not having a mechanics-based design procedure that allows the designer to quantify the required forces in the continuity plates is another reason for requiring expensive CJP welds in AISC 341-16.

According to the 2010 AISC *Seismic Provisions*, AISC 341-10 (AISC, 2010a), continuity plates are not required when the column flange thickness, t_{cf}, meets the following two requirements:

$$t_{cf} \geq 0.4\sqrt{1.8 b_{bf} t_{bf} \frac{R_{yb} F_{yb}}{R_{yc} F_{yc}}} \quad (1)$$

$$t_{cf} \geq \frac{b_{bf}}{6} \quad (2)$$

where b_{bf} and t_{bf} are the beam flange width and thickness, F_{yb} and F_{yc} are the beam and column yield stresses, and R_{yb} and R_{yc} are the beam and column yield stress adjustment factors, respectively. When required, the continuity plate thickness shall be at least equal to 50 and 100% of the beam flange thickness for one-sided and two-sided connections, respectively. Note that Equation 1 is a carryover from older codes (ICBO, 1994), except for the R_y factors. Specifically, this equation was derived based on the assumption that the bolted beam web, as in pre-Northridge moment connections,

Adel Mashayekh, Ph.D., Staff 2 Structures, Simpson Gumpertz & Heger, Inc., San Francisco, CA. Email: amashayekh@sgh.com

Chia-Ming Uang, Ph.D., Professor, Department of Structural Engineering, University of California, San Diego, La Jolla, CA. E-mail: cmu@ucsd.edu (corresponding)

Paper No. 2017-03

was not effective in sharing a portion of the beam moment such that each beam flange would be strained to 1.8 times the beam flange yield strength (Bruneau et al., 2011). Equating this required beam flange force to the flange local bending strength of the column specified in Section J10.1 of AISC 360, *Specification for Structural Steel Buildings* (AISC, 2016c), results in Equation 1. Equation 2 was established based on low-cycle fatigue consideration (Ricles et al., 2000; FEMA, 2000b).

Two changes were made in AISC 341-16. First, the continuity plate thickness requirement is relaxed from 100% to 75% of the beam flange thickness for two-sided connections (Lee et al., 2005). Second, Equation 1 was eliminated and replaced by a more general requirement. For connections in which the beam flanges are welded to the column flange, the required beam flange force, P_b, can be computed from the maximum probable moment, M_f, at face of column as follows:

(a) When beam webs are bolted connected to the column:

$$P_b = \frac{M_f}{\alpha_s d^*} \tag{3}$$

(b) When beam webs are welded to the column:

$$P_b = \frac{0.85 M_f}{\alpha_s d^*} \tag{4}$$

where

M_f = maximum probable moment at face of column as defined in AISC 358-16, *Prequalified Connections for Special and Intermediate Steel Moment Frames for Seismic Applications* (AISC, 2016b), for a prequalified moment connection or as determined from qualification testing

d^* = distance between centroids of beam flanges or beam flange connections to the face of the column

α_s = LRFD-ASD force level adjustment factor
= 1.0 for LRFD and 1.5 for ASD

The 0.85 factor in Equation 4 was based on Tran et al. (2013). The required beam flange force is then checked against all the applicable limit states stipulated in AISC 360-16, Section J10, to determine if continuity plates are needed.

In this paper, welds that connect a continuity plate to the column flanges and the web are referred to as the flange weld and web weld, respectively.

OBJECTIVE

Although some improvements have been made in AISC 341-16, the design of continuity plates and their welds is still prescriptive in nature. That is, the thickness of continuity plate is prescribed, and a CJP weld is required for the flange weld. Based on the relative stiffness (or flexibility) between the column flange being pulled out of its plane and the continuity plates being loaded mainly in shear in its own plane by the beam flange force, Tran et al. (2013) developed a flexibility-based procedure that allows the designer to calculate the required forces in both the continuity plate as well as flange and web welds, thus providing more freedom to size the thickness and design welded joints for the continuity plates. The objective of this study was to provide an experimental verification of this proposed design procedure.

PROPOSED DESIGN PROCEDURE

The procedure proposed by Tran et al. (2013) and subsequently modified in this study is summarized herein. Representing the beam flange force as

$$P_b = C_{pf} R_{yb} b_{bf} t_{bf} F_{yb} \tag{5}$$

AISC 341-10 assumed that the beam flange force adjustment factor, C_{pf}, was equal to 1.8 to establish the minimum column flange thickness requirement shown in Equation 1. While this assumed value is reasonable for pre-Northridge–type welded flange-bolted web moment connections, where the bolted web is ineffective in contributing to the moment resistance, Tran et al. showed that this assumption, and hence Equation 1, is conservative for some post-Northridge moment connections like the reduced beam section (RBS) or welded unreinforced flange-welded web (WUF-W) moment connections in AISC 358, where the beam web is directly welded to the column flange with a CJP weld. Based on finite element analysis, the following C_{pf} values were recommended by Tran et al.:

For RBS connection: $C_{pf} = 1.25$ (6a)

For WUF-W connection: $C_{pf} = 1.75$ (6b)

When continuity plates are required, the beam flange axial force, P_b, is apportioned to each continuity plate based on the following equation (Tran. et al., 2013):

$$P_{cp} = \frac{P_b}{2}\left(\frac{b_{bf} - t_{pz} - 2t_{cf}}{b_{bf}}\right)\left(\frac{B_{cf}}{B_{cf} + B_{cp}}\right) \tag{7}$$

where

B_{cf} = column flange out-of-plane flexibility coefficient

B_{cp} = continuity plate in-plane flexibility coefficient

P_{cp} = normal force transmitted to one continuity plate

b_{bf} = beam flange width

t_{cf} = column flange thickness

t_{pz} = panel zone thickness

(See Tran et al. for the derivation of Equation 7.) Following the procedure, the required forces can be computed along three edges of the continuity plate. To ensure that

the continuity plates have sufficient in-plane stiffness, the designer then checks the available column strength determined using the applicable limit states stipulated in AISC 360-16, Section J10 for the portion of the beam flange force that will be transmitted from the beam flange to the column web directly:

$$P_b - 2P_{cp} \le \phi R_n \tag{8}$$

Figure 1 shows that the edges of the continuity plate next to the loaded column flanges are subjected to both normal and shear forces, where the shear force from moment equilibrium is:

$$V_{cp} = \left(\frac{0.6b}{d}\right)\sum P_{cp} \tag{9}$$

The Von-Mises yield criterion is then used by Tran et al. (2013) to check the strength of the continuity plates:

$$\left(\frac{P_{cp}}{F_{ycp}A_n}\right)^2 + \left(\frac{V_{cp}}{\frac{F_{ycp}}{\sqrt{3}}A_n}\right)^2 \le 1 \tag{10}$$

where

A_n = $b_n t_{cp}$
F_{ycp} = yield stress of continuity plate
b = $b_{clip} + b_n$ (total width of continuity plate)
b_{clip} = corner clip size
b_n = net width of continuity plate
d = depth of continuity plate
t_{cp} = thickness of continuity plate

When Equation 9 is satisfied, either fillet welds or partial-joint-penetration groove welds can be used to connect the continuity plates to the column flanges. If not, Tran et al. (2013) suggested that CJP groove welds still be used because continuity plates are expected to yield. To avoid the use of CJP welds, however, an alternative is to increase the thickness of the continuity plates such that Equation 9 is satisfied.

In designing the specimens for this test program, some modifications were made to Equation 9. By ignoring the corner clips in the continuity plates in finite element analysis, Tran et al. (2013) suggested that the normal force, P_{cp}, be located at a distance $0.6b$ from the column web (see Figure 1); the moment produced by this force with an eccentricity with respect to the center of the net width of the continuity plate was ignored in checking the strength in Equation 9. To include the moment component, Dowswell (2015) suggested an *M-V-P* yield criterion, which can be rewritten as the following:

$$\left(\frac{P_{cp}e}{Z_{xn}F_{ycp}}\right) + \left(\frac{P_{cp}}{F_{ycp}A_n}\right)^2 + \left(\frac{V_{cp}}{\frac{F_{ycp}}{\sqrt{3}}A_n}\right)^4 \le 1 \tag{11}$$

where Z_{xn} is the plastic section modulus of the net section:

$$Z_{xn} = \frac{t_{cp}b_n^2}{4} \tag{12}$$

Refer to Figure 2(a) for a continuity plate in a two-sided (i.e., interior) moment connection, where corners are clipped to clear the *k*-area of the column section. Free-body diagram 3 in Figure 2(c) shows that the normal force P_{cp} acts at a distance $0.6b$ from the column web, and moment equilibrium requires that

$$V_{cp} = \left(\frac{0.6b}{d - 2b_{clip}}\right)\sum P_{cp} \tag{13}$$

Next consider free-body diagram 1 or 2. The corner clip causes the normal force at the edge of the net width to shift by an amount e^* to satisfy moment equilibrium:

$$e^* = \frac{b_{clip}V_{cp}}{P_{cp}} \tag{14}$$

Therefore, the moment produced by the eccentrically loaded P_{cp} at the center of the net width equals eP_{cp}, where

$$e = 0.6b + e^* - (b_{clip} + 0.5b_n) \tag{15}$$

The same approach can be applied to the continuity plate of a one-sided (i.e., exterior) moment connection. But the shear force calculation needs to be modified slightly.

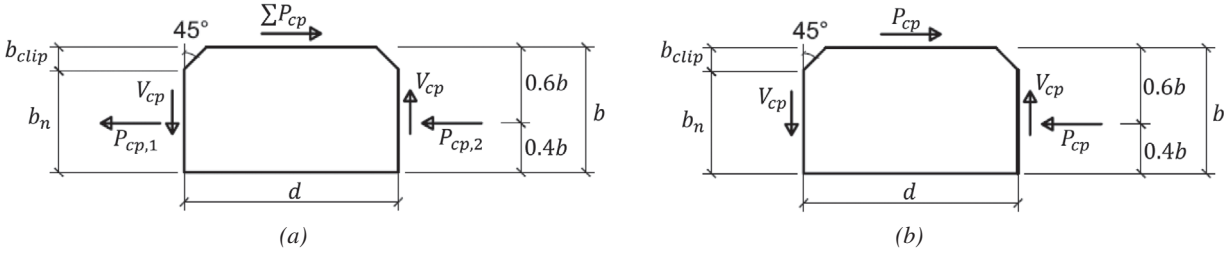

Fig. 1. Free-body diagram of a continuity plate: (a) interior connection; (b) exterior connection (Tran et al., 2013).

As shown in Figure 3, it is assumed that the normal force at the nonloaded column flange side of the continuity plate equals zero. Therefore, the shear force is

$$V_{cp} = \left(\frac{0.6b}{d - b_{clip}} \right) P_{cp} \tag{16}$$

and Equation 11, not Equation 9, was used to design the continuity plates in this test program.

TEST PROGRAM

Two full-scale RBS connection specimens were tested. Figure 4 shows the member sizes and specimen dimensions. Specimen C1 had a W30×116 beam connected to a deep column (W24×176), while a W36×150 beam was connected to a shallow column (W14×257) for specimen C2. Table 1 summarizes the steel mechanical properties; ASTM

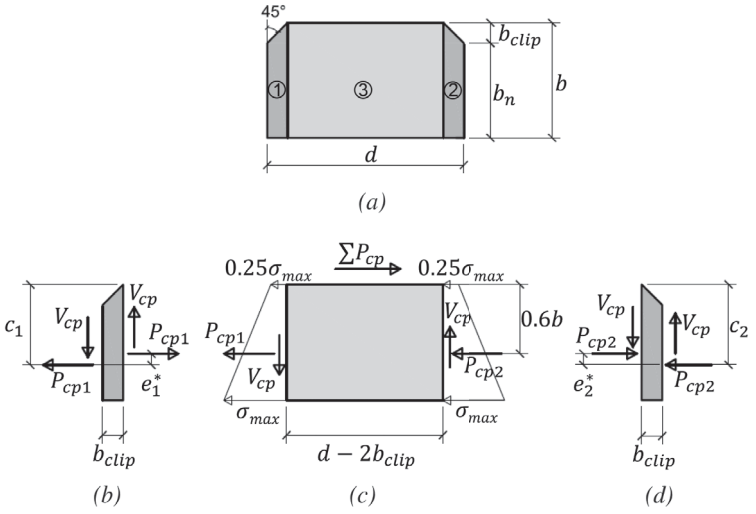

Fig. 2. Continuity plate free-body diagrams (interior connection): (a) geometry of continuity plate; (b) free-body 1; (c) free-body 3; (d) free-body 2.

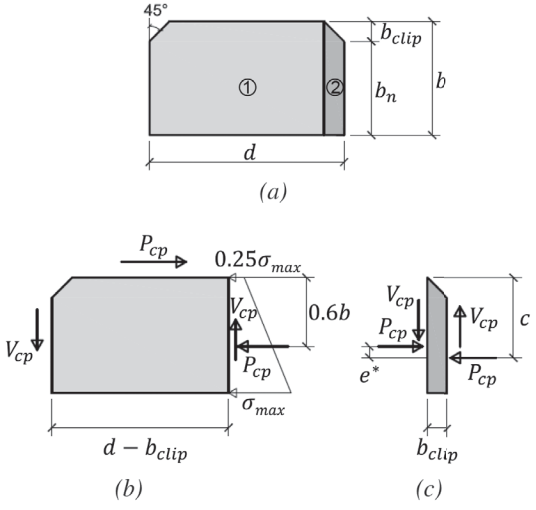

Fig. 3. Continuity plate free-body diagrams (exterior connection): (a) geometry of continuity plate; (b) free-body 1; (c) free-body 2.

A992 steel was specified for the beams and columns, and ASTM A572 Grade 50 steel was specified for the continuity plates. Figure 5 depicts the RBS dimensions and the weld details. Except for the continuity plates and their welds, both specimens were designed in accordance with AISC 341-10 (AISC, 2010a) and AISC 358-10 (AISC, 2010b). No doubler plates were required per AISC 341-10.

Member sizes as well as RBS dimensions were selected such that the demand-capacity ratios for the panel zone shear were high (0.9 and 0.95 for specimens C1 and C2, respectively). The intent of such design was to produce a large panel-zone deformation to investigate if kinking of the column flanges would adversely affect the performance of fillet welds that connected the continuity plates to the column flanges.

The required forces in the continuity plates and the fillet weld sizes per the proposed procedure are provided in Table 2. The proposed design called for a continuity plate thickness of ⅞ in. for specimen C2. AISC 341 implicitly assumes that continuity plates should remain essentially elastic. Because the effect of yielded continuity plates had never been reported in the literature, it was decided to use ⅝-in.-thick continuity plates instead. A comparison of the welds for the continuity plates based on both AISC 341-10 and the proposed procedure is also provided in the table. Self-shielded, flux-cored arc welding with an E71T-8 electrode (Lincoln/Innershield NR 232) that met the demand critical requirement of AWS D1.8 (AWS, 2009) was used for making the welds.

Table 3 summarizes the components of Equation 11 for the design of both specimens. The continuity plates of specimen C2 were significantly undersized with a demand-capacity ratio of 1.31. The shear force component was minimal for the deep-column specimen C1, mainly because the denominator $(d - 2b_{clip})$ in Equation 13 was larger. For the shallow-column specimen C2, both shear and moment components are significant. Therefore, it is not appropriate to use Equation 9 to check the strength of continuity plates.

Lateral restraint was provided near the loaded beam end for both specimens. For specimen C1, which utilized a deep column, one extra restraint was provided at a distance 15.4 in. outside the RBS region to simulate the slab restraining effect. The loading sequence in AISC 341-16, Chapter K, expressed in terms of the story drift angle for beam-to-column moment connection testing was followed. A positive drift angle corresponded tothe beam end deflection upward.

TEST RESULTS

Figure 6 shows the global response of the test specimens. Both specimens performed well and met the AISC acceptance criteria, which require that (1) the connection shall accommodate a story-drift angle of at least 0.04 rad, and (2) the measured flexural strength of the beam shall equal at least 80% of the nominal plastic moment, M_{pn}, of the connected beam at a story-drift angle of 0.04 rad.

Figure 7 shows the yielding and buckling pattern of

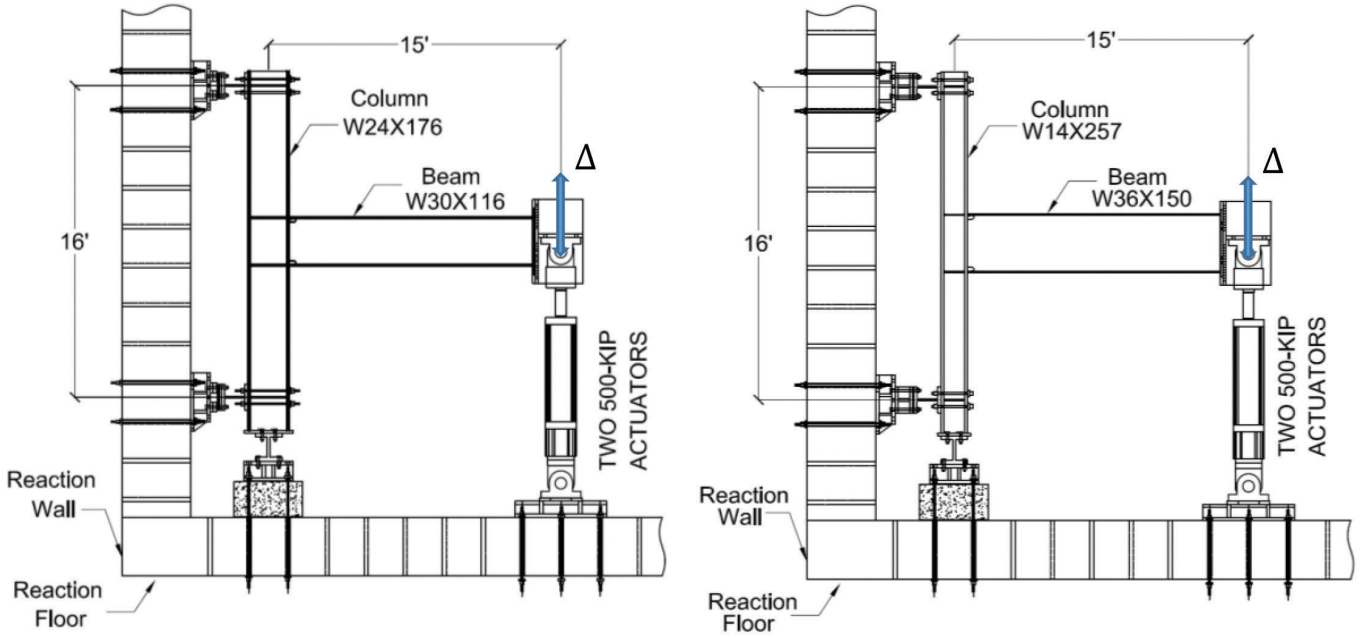

Fig. 4. Test specimens and test setup: (a) specimen C1; (b) specimen C2.

specimen C1; as expected, local buckling and lateral-torsional buckling in the beam as well as shear yielding in the panel zone were observed. Testing was stopped after completing one cycle at 5% story drift because the beam flexural strength at the column face had degraded below $0.8M_{pn}$. The panel zone of specimen C2 was designed with a higher demand-capacity ratio (0.95). Shear yielding of the panel zone was very significant (Figure 8). The panel zone shear yielding caused significant column flange kinking; localized column flange yielding due to such kinking is evidenced in Figure 9. Local buckling of the beam occurred at 4% drift, and lateral-torsional buckling was observed during the second cycle at 5% drift. One cycle at 7% drift was then imposed on the specimen before the test was stopped.

Figures 10 and 11 show the close-up views of the fillet welds connecting the continuity plates to the column flanges. Dye-penetrant testing was conducted on the fillet welds after the tests; no damage was observed. Note that significant kinking of the column flanges occurred at these weld locations for both specimens because the panel zones were intentionally designed to have large demand-capacity ratios. Figure 12 shows that the shear strain reached nine times the shear yield strain for specimen C2. The shear strain reached in specimen C1 was lower; the "unusual" nonlinear response shown in Figure 12(a) was due to twisting of the deep column (Chi and Uang, 2002).

Based on the flaking pattern of the whitewash in the connection region, it was observed that the continuity plates of specimen C2 yielded, while those of specimen C1 remained elastic; measured strains (to be presented later) further confirm this observation. Although significant yielding occurred in the continuity plates of specimen C2 due to the intentional undersize of the plate thickness, the connection performance was not affected.

Beam flanges and continuity plates were instrumented with strain gages and rosettes (see Figure 13). The measured

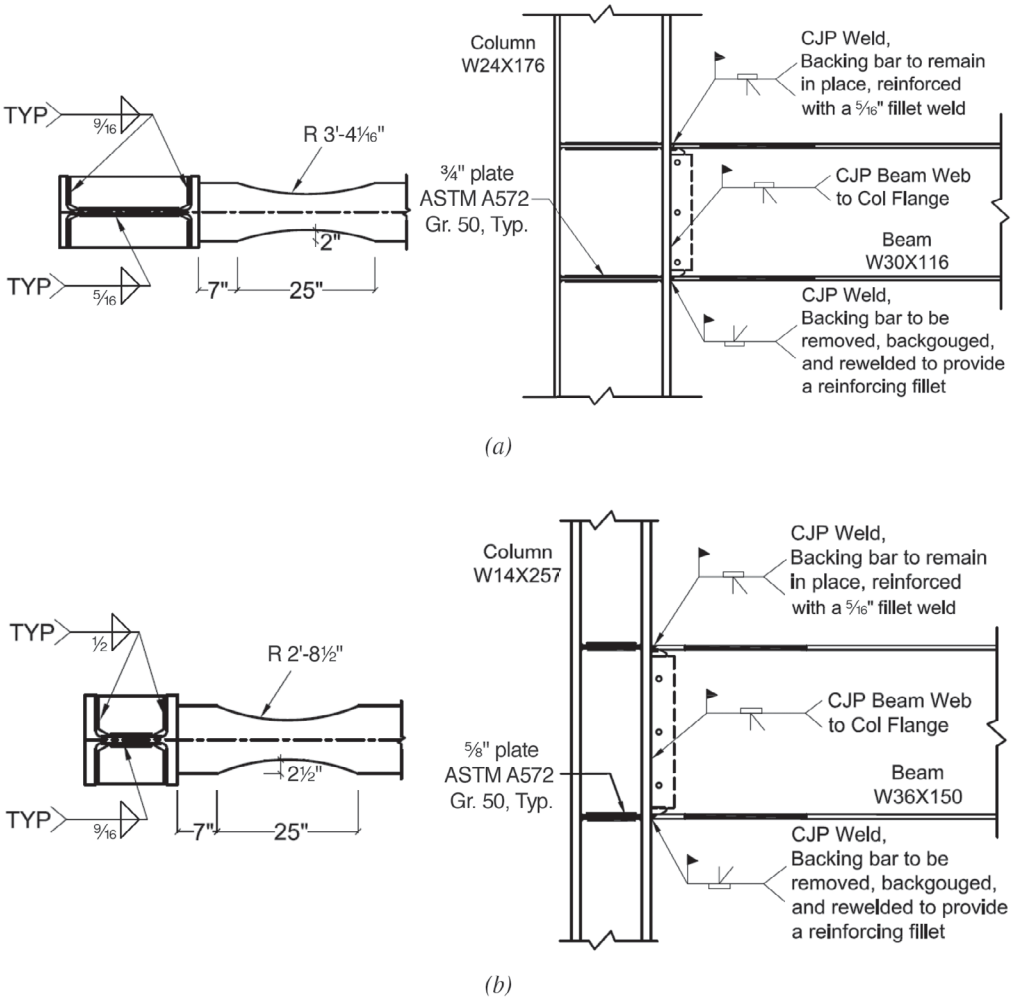

Fig. 5. RBS connection details: (a) specimen C1; (b) specimen C2.

Table 1. Steel Mechanical Properties				
Specimen No.	**Component**	**Yield Stress (ksi)**	**Tensile Strength (ksi)**	**Elongation (%)**
C1	Beam flange	56.9	75.6	34.5
	Beam web	58.5	73.2	39.5
	Column flange	57.2	70.6	39.1
	Column web	58.5	72.2	37.3
	Continuity plate	68.1	85.6	36.9
C2	Beam flange	53.5	74.9	38.3
	Beam web	57.9	74.7	38.1
	Column flange	52.3	74.3	37.7
	Column web	54.8	74.8	38.6
	Continuity plate	54.1	79.8	35.1

Table 2. Continuity Plate and Weld Design				
	Specimen C1		**Specimen C2**	
	Proposed Procedure	**AISC 341-16**	**Proposed Procedure**	**AISC 341-16**
Required continuity plate forces (kips)	$P_{cp} = 157.6$ $V_{cp} = 26.7$	N.A.	$P_{cp} = 157.0$ $V_{cp} = 62.8$	N.A.
Continuity plate thickness	¾ in.	½ in. (= $t_{bf}/2$)	⅝ in.	½ in. (= $t_{bf}/2$)
Continuity plate-to-column flange weld	Fillet weld (⅝ in.)	CJP weld	Fillet weld (½ in.)	CJP weld
Continuity plate-to-column web weld	Fillet weld (⅝ in.)	Fillet weld (⅜ in.)	Fillet weld (⅝ in.)	Fillet weld (⅜ in.)

Table 3. Continuity Plate Strength Check				
	Equation 11			
Specimen No.	**Moment Component,** $\left(\frac{P_{cp}e}{Z_{xn}F_{ycp}}\right)$	**Normal Force Component,** $\left(\frac{P_{cp}}{F_{ycp}A_n}\right)^2$	**Shear Force Component,** $\left(\frac{V_{cp}}{\frac{F_{ycp}}{\sqrt{3}}A_n}\right)^4$	**Σ**
C1	0.14	0.78	0.01	0.93
C2	0.36	0.80	0.15	1.31

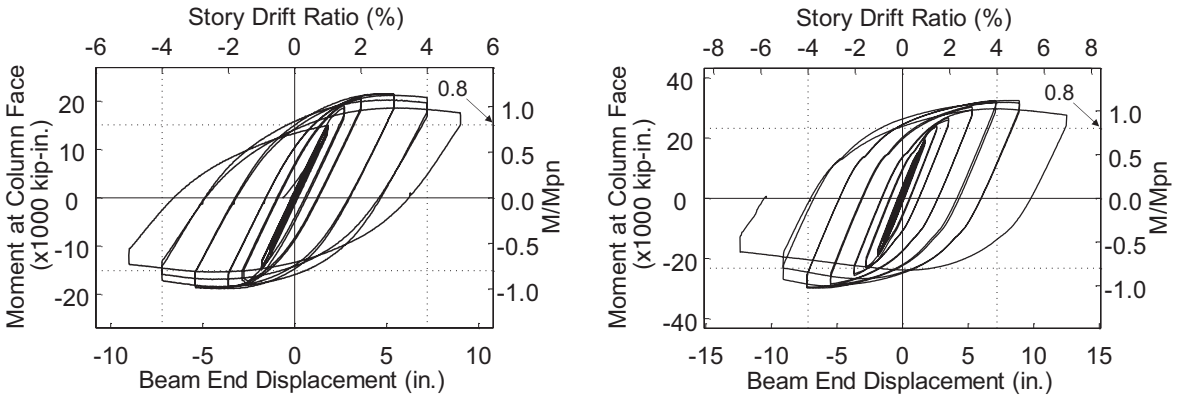

Fig. 6. Global responses: (a) specimen C1; (b) specimen C2.

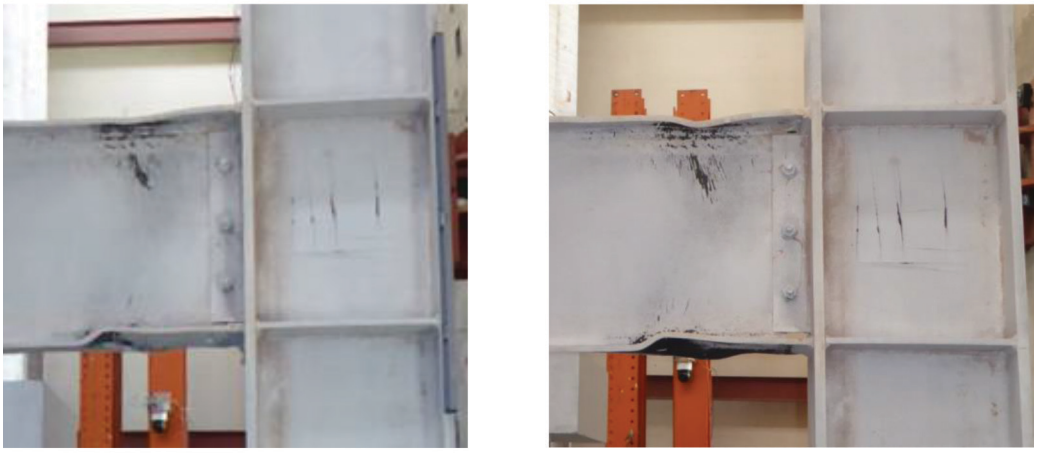

Fig. 7. Global view of specimen C1: at 0.04-rad drift (second cycle); (b) at test completion.

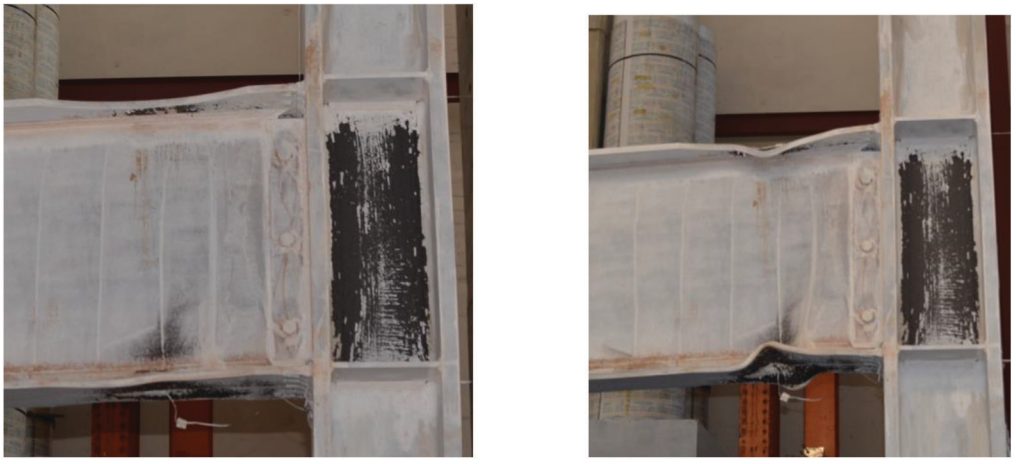

Fig. 8. Global view of specimen C2: (a) at 0.04-rad drift (second cycle); (b) at 0.07-rad drift (first cycle).

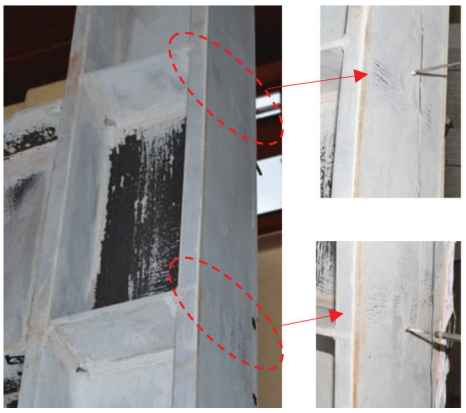

Fig. 9. Specimen C2 localized column flange yielding due to panel zone deformation.

(a) *(b)*

Fig. 10. Fillet welds of specimen C1 after test: (a) beam top flange level; (b) beam bottom flange level.

(a) *(b)*

Fig. 11. Fillet welds of specimen C2 after test: (a) beam top flange level; (b) beam bottom flange level.

normal and shear strains, after normalizing by their respective yield strains, of specimen C2 at 4% story drift are presented in Figure 14. Only one continuity plate was instrumented. For clarity, however, the normalized shear strain distributions are plotted on the other continuity plate. At a distance 3 in. away from the loaded column flange, the beam flange flexural strains reached $3.5\varepsilon_y$, where ε_y is the yield strain. On the opposite side of the loaded column flange, the continuity plate also yielded for the reason mentioned earleir; the maximum normal strain, which occurred near the free edge of the continuity plate, reached $2.63\varepsilon_y$. Along the length of the flange weld, the profile of the strain normal to the weld was consistent with that proposed by Tran et al. (2013).

Figure 14 also shows that shear strains of the continuity plate along the length of the same flange weld were high; the maximum shear strain reached $1.56\gamma_y$, where γ_y is the shear yield strain. The maximum shear strain occurred near the column web, not the free edge of the continuity plate, which is also consistent with that proposed by Tran et al. (2013), Along the length of the web weld—that is, along the column web—the shear strain reached a maximum value of $1.88\gamma_y$ at the loaded column flange end. This uneven strain distribution reflects the effect of the short distance in a shallow (W14) column that a portion of the beam flange force needed to be transferred from the continuity plate through the column web to the panel zone.

The normal strain from strain rosette R1 near the nonloaded column flange was about 0.6 times that of the strain of R6 near the loaded column flange, which indicates that a significant portion of the force was still transmitted through the continuity plate to the nonloaded column flange. Therefore, it is prudent to use the same weld size for both flange welds.

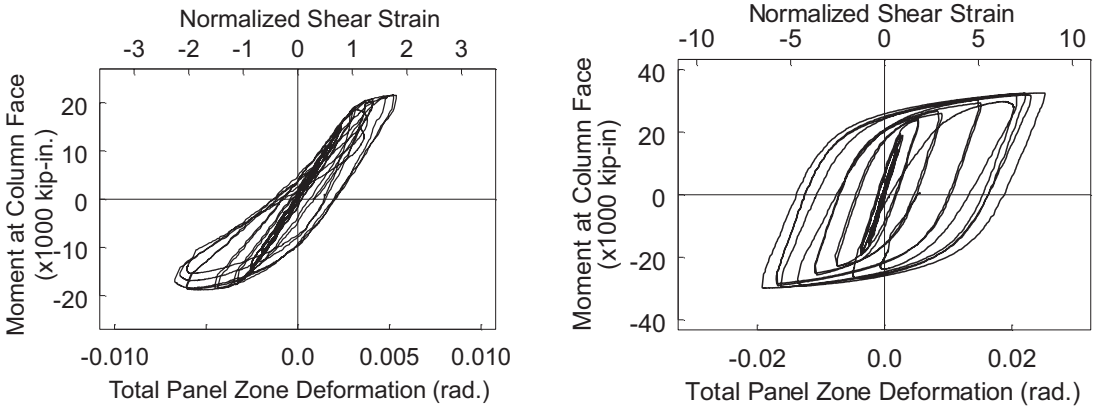

Fig. 12. Measured panel zone responses: (a) speciment C1; (b) specimen C2.

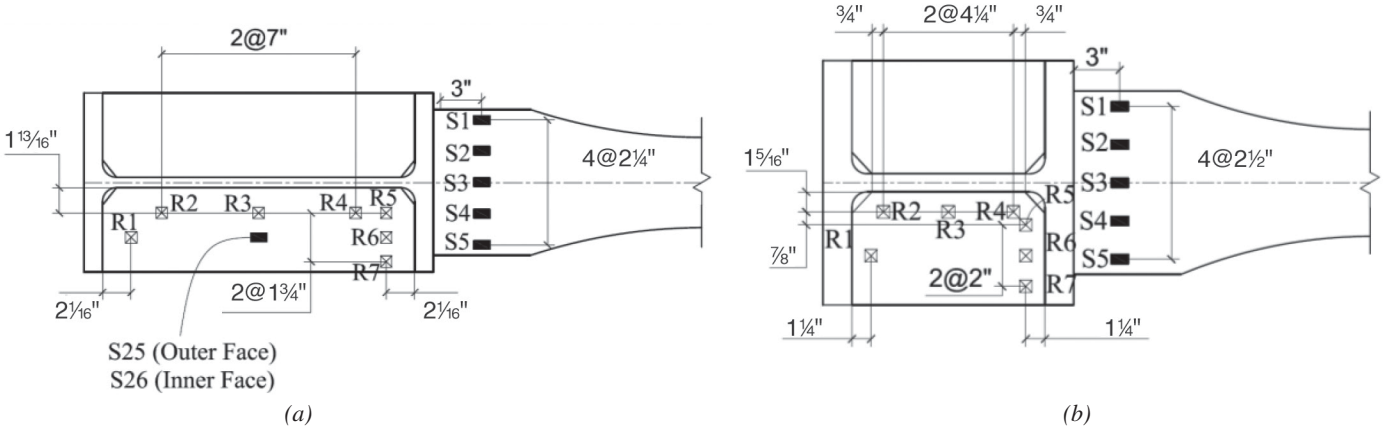

Fig. 13. Strain gage and rosette layout (beam top flange level): (a) specimen C1; (b) specimen C2.

Specimen C1 had a deep (W24) column, which experienced twisting due to lateral-torsional buckling of the beam and affected strain readings. Based on the readings of the strain gages that were placed on the loaded column flange, column twisting became significant beyond 1.5% drift when warping stresses started to affect flexural strains in the column flange. Therefore, measured strains of a continuity plate at the top flange level at 1.5% drift are presented. At this load level, which was about 86% that of the peak load experienced by this specimen, Figure 15 shows that the magnitude of the continuity plate normal strains perpendicular to the flange weld was similar to that of the beam flange strains. From the free-body diagram in Figure 1, the force couple produced by the shear force V_{cp} along each flange weld is needed to satisfy moment equilibrium; the shear force is smaller relative to the normal force P_{cp} when the column is deep because the level arm is larger. This is indeed observed in Figure 15, where the normalized shear strain along the flange weld was significantly smaller than that in Figure 14. In a deep column, a longer distance along the column web is available to transmit the P_{cp} force through the web weld to the panel zone. This explains why the shear strain distribution along the web weld is more uniform than that in Figure 14.

FINITE ELEMENT ANALYSES

It is difficult to experimentally construct the free-body diagram of the continuity plate from strain gage measurements. Instead, finite element analysis (FEA) by using the commercial software ABAQUS (2014) was conducted. Free-body diagrams established from the FEA are then compared with those established from the proposed procedure.

Four-node, thick-shell brick elements (type S4R in ABAQUS) were used to model the specimens. Typical steel properties (E = 29,000 ksi, ν = 0.3) were used in the model to describe elastic material characteristics. Also for inelastic behavior, following the work of Chaboche (1986), material parameters that can simulate both the kinematic and isotropic hardening responses of an ASTM A992/A572 steel coupon under cyclic loading were incorporated. Figure 16 compares the experimental and predicted global response of each specimen; the correlation is satisfactory.

Figures 17 and 18 compare the free-body diagrams of two specimens. For these two one-sided moment connections, the proposed procedure assumes that the left (i.e., the nonloaded column flange) side has no normal force; the normal force from the beam flange is transferred completely to the column web through the continuity plate. The FEA shows that the nonloaded column flange does resist a portion of the

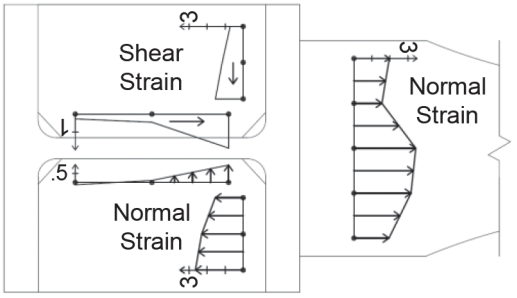

Fig. 14. Specimen C2 beam top flange and continuity plate normalized strain distributions (4% story drift).

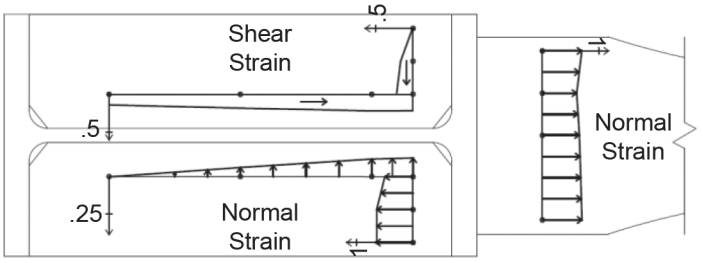

Fig. 15. Specimen C1 beam top flange and continuity plate normalized strain distributions (1.5% story drift).

normal force from the beam flange; the percentage is higher for shallow columns than for deep columns. This will reduce the shear force in the web weld. Because the proposed procedure assumes that all normal force from the beam flange is transmitted to the column web, the web weld design is somewhat conservative. These two figures also show that the shear force along the flange weld is larger when a shallow column is used.

SUMMARY AND CONCLUSIONS

AISC 341-16 requires that continuity plates in an SMF be connected to the column flanges by CJP welds. Tran et al. (2013) have proposed a design procedure that considers the in-plane flexibility (or stiffness) of the continuity plate relative to the out-of-plane flexibility of the column flange being loaded by the beam flange in determining the forces that are transmitted through the continuity plates to the column panel zone. As a pilot study to experimentally verify this design procedure, two full-scale reduced beam section (RBS) connection specimens were tested. Using a slightly modified procedure of that originally proposed by Tran et al., continuity plates in both specimens were fillet-welded to the column flanges. One specimen (C1) used a deep (W24) column, and the other (C2) had a shallow (W14) column. The continuity plate thickness of specimen C2 was undersized to evaluate the effect of yielded continuity plates on the connection performance. While still satisfying the code requirement, the demand-capacity ratio of the panel zone was high (0.90 and 0.95 for C1 and C2, respectively) in order to evaluate the effect of column flange kinking due to significant panel zone yielding on the performance of the fillet welds.

Based on the test results and the associated analytical studies, the following conclusions can be drawn:

1. Both specimens performed very well and met the 0.04-rad story-drift requirement specified in AISC 341-16. As expected, yielding and buckling in the RBS region, as well as significant shear yielding in the panel zone, were observed.
2. Fillet welds designed per the proposed design procedure that connected continuity plates to the column flanges did not show any damage. Therefore, CJP welds as required by AISC 341-16 may not always be necessary.
3. AISC 341-10 specifies a prescriptive requirement for the thickness of the continuity plates: half and full thickness of the beam flange for the exterior and interior moment connections, respectively. (The full thickness requirement has been changed to three-quarter thickness for the interior connection in AISC 341-16.) Test results showed that such a prescriptive requirement may not be needed; the proposed procedure will consider directly the effect of thickness on the forces transmitted to the continuity plates.
4. Edges of the continuity plates connecting to the column flanges are subjected to not only normal force, but also to shear force and moment; the moment is produced by the normal force with an eccentricity (Figures 2 and 3). The moment was ignored by Tran et al. (2013) in the strength check of the continuity plate (Equation 9). The revised procedure used to design the specimens in this study considered the moment effect (Equation 11). The effect of moment and shear can be significant, especially for continuity plates in shallow columns (Table 3).
5. AISC 341-16 implicitly assumes that continuity plates shall remain essentially elastic per the capacity design principles. Because the effect of plate yielding has never been reported in the literature, the plate thickness

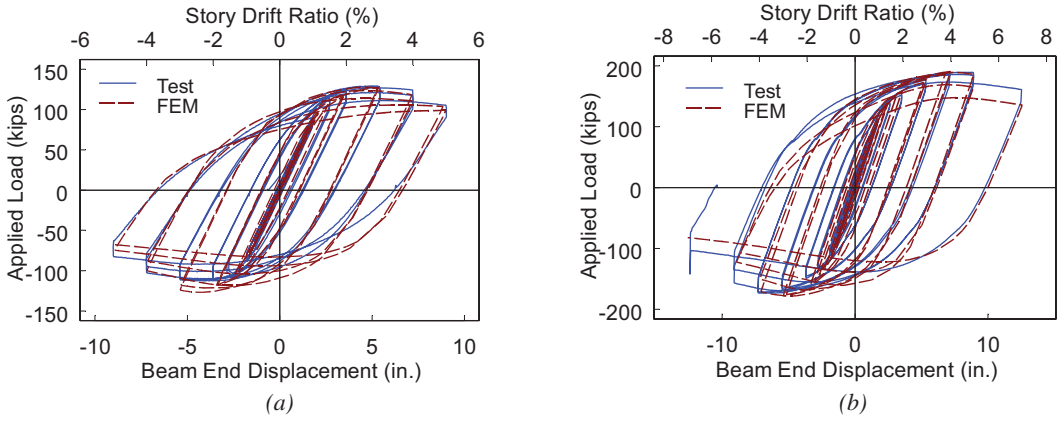

Fig. 16. Correlation of Global Responses: (a) specimen C1; (b) specimen C2.

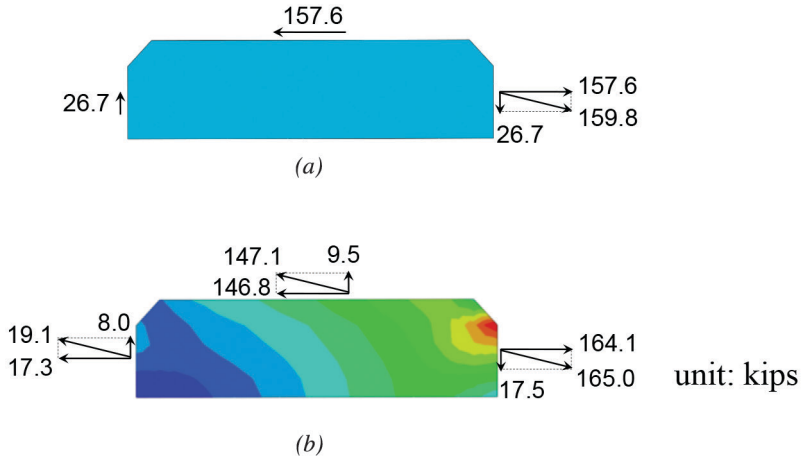

Fig. 17. Specimen C1—comparison of continuity plate free-body diagram: (a) proposed procedure; (b) finite element analysis.

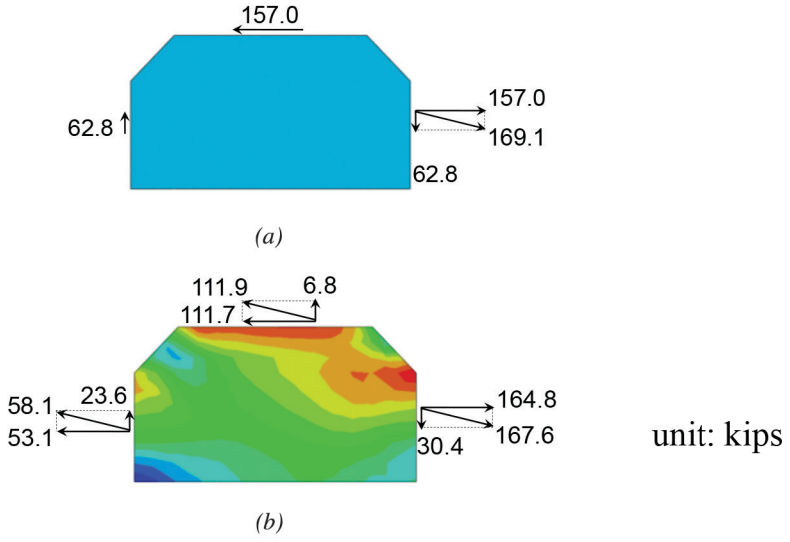

Fig. 18. Specimen C2—comparison of continuity plate free-body diagram: (a) proposed procedure; (b) finite element analysis.

of one specimen (C2) was undersized. Testing did show significant yielding in the plates, but connection performance was not affected.

ACKNOWLEDGMENTS

This project was sponsored by the American Institute of Steel Construction (AISC); Mr. Tom Schlafly served as the project manager for this research. Schuff Steel Company donated the test specimens. AMEC Foster Wheeler in San Diego provided inspection services to this project. Mr. Patrick M. Hassett of Hassett Engineering Inc. reviewed the design of the test specimens.

REFERENCES

ABAQUS (2014), *ABAQUS Standard User's Manual*, Version 6.14, ABAQUS Inc.

AISC (2010a), ANSI/AISC 341-10, *Seismic Provisions for Structural Steel Buildings*, American Institute of Steel Construction, Chicago, IL.

AISC (2010b), ANSI/AISC 358-10, *Prequalified Connections for Special and Intermediate Steel Moment Frames for Seismic Applications,* American Institute of Steel Construction, Chicago, IL.

AISC (2016a), ANSI/AISC 341-16, *Seismic Provisions for Structural Steel Buildings*, American Institute of Steel Construction, Chicago, IL.

AISC (2016b), ANSI/AISC 358-16, *Prequalified Connections for Special and Intermediate Steel Moment Frames for Seismic Applications,* American Institute of Steel Construction, Chicago, IL.

AISC (2016c), ANSI/AISC 360-16, *Specification for Structural Steel Buildings*, American Institute of Steel Construction, Chicago, IL.

AWS (2009), *Structural Welding Code-Seismic Supplement*, AWS D1.8/D1.8M, American Welding Society, Miami, FL.

Bruneau, M., Uang., C.-M. and Sabelli, R. (2011), *Ductile Design of Steel Structures*, 2nd Ed., McGraw-Hill, New York, NY.

Chaboche, J.L. (1986), "Time-Independent Constitutive Theories for Cyclic Plasticity," *International Journal of Plasticity*, Vol. 2, No. 2, pp. 149–188.

Chi, B. and Uang, C.-M. (2002), "Cyclic Response and Design Recommendations of Reduced Beam Section Moment Connections with Deep Columns," *Journal of Structural Engineering*, ASCE, Vol. 128, No. 4, pp. 464–473.

Dowswell, B. (2015), "Plastic Strength of Connection Elements," *Engineering Journal*, AISC, Vol. 52, No. 1, pp. 47–66.

FEMA (2000a), "Recommended Seismic Design Criteria for New Steel Moment-Frame Buildings," FEMA 350, Federal Emergency Management Agency, Washington, DC.

FEMA (2000b), "State-of-the-Art Report on Connection Performance," FEMA-355D, Federal Emergency Management Agency, Washington, D.C.

ICBO (1994), *Uniform Building Code*, International Conference of Building Officials. Whittier, CA.

Lee, D., Cotton, S.C., Hajjar, J.F. and Dexter, R.J. (2005), "Cyclic Behavior of Steel Moment-Resisting Connections Reinforced by Alternative Column Stiffener Details I. Connection Performance and Continuity Plate Detailing," *Engineering Journal*, AISC, Vol. 42, No. 4, pp. 189–213.

Ricles, J.M., Mao. C., Lu, L.W. and J. Fisher, J.W. (2000), "Development and Evaluation of Improved Details for Ductile Welded Unreinforced Flange Connections," SAC BD 00-24, SAC Joint Venture, Sacramento, CA.

Tran, A.T., Hasset, P.M. and Uang, C.-M. (2013), "A Flexibility-Based Formulation for the Design of Continuity Plates in Steel Special Moment Frames," *Engineering Journal*, AISC, Vol. 50, No. 3, pp. 181–200.

Steel Structures Research Update

The Role of Gravity Framing in the Seismic Performance of Steel Buildings

JUDY LIU

INTRODUCTION

Ongoing work on the seismic performance of steel buildings is highlighted. Dr. Michael Engelhardt leads the University of Texas at Austin team of Dr. Patricia Clayton, Dr. Todd Helwig, Dr. Eric Williamson, and Ph.D. student Sean Donahue. Dr. Engelhardt is the Adnan Abou-Ayyash Centennial Professor in Transportation Engineering and director of the Ferguson Structural Engineering Laboratory. Dr. Clayton is an assistant professor who has been awarded both the AISC Milek Fellowship and the AISC Early Career Faculty Award, among other honors. Dr. Helwig is a professor and associate chair for civil engineering, holds the J. Neils Thompson Centennial Teaching Fellowship in civil engineering, and is this year's AISC T.R. Higgins Lecturer. Dr. Williamson is a professor and holds the J. Hugh and Betty Liedtke Centennial Fellowship in Civil Engineering.

The research fills knowledge gaps with respect to the role of the gravity framing in the seismic response of steel buildings. Beam-to-column connections in gravity load-resisting frames are typically designed as "simple shear" or "pin" connections with no flexural strength or stiffness. However, these simple shear connections do have some flexural resistance. With consideration of these connections acting compositely with the floor slab, the flexural strength and stiffness increase. Given the number of gravity frame connections in a typical steel building, their overall contribution to the seismic response of the structure could be significant. However, the available data on cyclic behavior of simple shear connections are limited. The current research is expanding the database with a series of large-scale experiments and developing models and tools to quantify the role of the gravity framing in the seismic performance of steel buildings.

The research described here complements numerical studies conducted by Foutch (2000), Krawinkler (2000), and Foutch and Yun (2002) as part of the post-Northridge SAC-FEMA studies, which included research on the effects of gravity framing on the seismic performance of steel buildings constructed with moment frames. More recently, a study by Flores et al. (2012) also examined the influence of gravity framing on the seismic collapse risk of steel buildings with moment frames, using the FEMA P-695 (2009) methodology. These past studies have shown that gravity framing can contribute significantly to the lateral load resistance of a building. For buildings with lateral force-resisting systems of limited ductility (e.g., similar to older, "pre-Northridge" moment connections), the effects of the gravity framing could mean "the difference between collapse or survival" for a building (Foutch and Yun, 2002). For buildings with ductile moment frames, including the gravity framing in the building model can significantly reduce collapse risk; this reduction can be attributed to the combined effects of the flexural resistance of the gravity connections and the gravity column continuity helping to prevent soft-story mechanisms (Flores et al., 2012). The current research investigates the flexural resistance provided by gravity connections, particularly with consideration of the composite concrete floor slab. To supplement past experimental testing of single plate shear connections with and without concrete slabs tested under cyclic loading by Liu and Astaneh-Asl (2000), the large-scale experimental program in this study focuses on double-angle shear connections with variations in composite floor slab details that are prevalent in existing building construction. Preliminary results from this study are discussed.

RESEARCH OBJECTIVES

Some of the past work on shear connection behavior was motivated by observations after the 1994 Northridge earthquake; damaged steel buildings had significant fractures in the welded moment connections, but none of the buildings collapsed (Anderson et al., 1995). Numerical studies of steel buildings suggested that the gravity frames supplemented the lateral resistance of the moment frames (e.g., Foutch and Yun, 200; Gupta and Krawinkler, 1999). Experimental studies prior to and after Northridge also highlighted the contribution of the floor slab to the flexural strength and stiffness of simple and semi-rigid connections (e.g., Liu and

Judy Liu, Ph.D., Research Editor of the AISC *Engineering Journal*, Professor, Oregon State University, School of Civil & Construction Engineering, Corvallis, OR. Email: judy.Liu@oregonstate.edu

Astaneh-Asl, 2000; Leon, 1990; Azizinamini and Radziminski, 1989). "While those studies have shown that simple shear connections can exhibit significant flexural capacity, especially in the presence of a composite floor slab, the strength, stiffness and ductility of those connections can vary significantly depending on connection and floor system details. Given the large number of different configurations seen in gravity connections, questions still remain as to the behavior of such systems" (Donahue et al., 2017).

The overarching goal of the research is to fill knowledge gaps with respect to the data and models needed to quantify the effect of the gravity framing system on seismic performance. Specific research objectives are to:

- Develop a database of previous experiments on typical simple beam-to-column shear connections used in gravity framing.
- Generate new experimental data from a series of large-scale experiments on simple shear connections under combined gravity and cyclic lateral load.
- Develop gravity connection models at various levels of complexity and detail for use in seismic analysis.

These objectives will be achieved through a large-scale experimental program conducted together with computational modeling, including a component spring model to simulate the cyclic behavior of the gravity framing connections in OpenSees (McKenna et al., 2000). Development and validation of these component spring models is ongoing. For the experimental program, questions related to the connection parameters and floor slab details are addressed. Some of the results and preliminary conclusions from those experiments are highlighted in this article.

TEST PROGRAM

A prototype steel frame building provides the basis for the design of the test set-up, loading and details of the test specimens. Initial testing in this study found that the flexural resistance at the gravity connections can be significant due to the tensile capacity of the metal decking. Therefore, in addition to double-angle and floor slab parameters to better understand moment-rotation behavior, changes in detailing and their effects on the tensile resistance from the floor slab are a primary focus of the study.

Test Set-Up

The test set-up was designed based on the boundary conditions and gravity loading at a typical girder to column joint in a prototype building. The prototype building has W14×22 filler beams framing into W21×55 girders at 7.25-ft intervals. The girders are supported by 11.5-ft story-height W12×96 columns at 29.5-ft spacing. The cruciform test specimen shown in Figure 1 represents a portion of the gravity framing from mid-span to midspan of girder and from

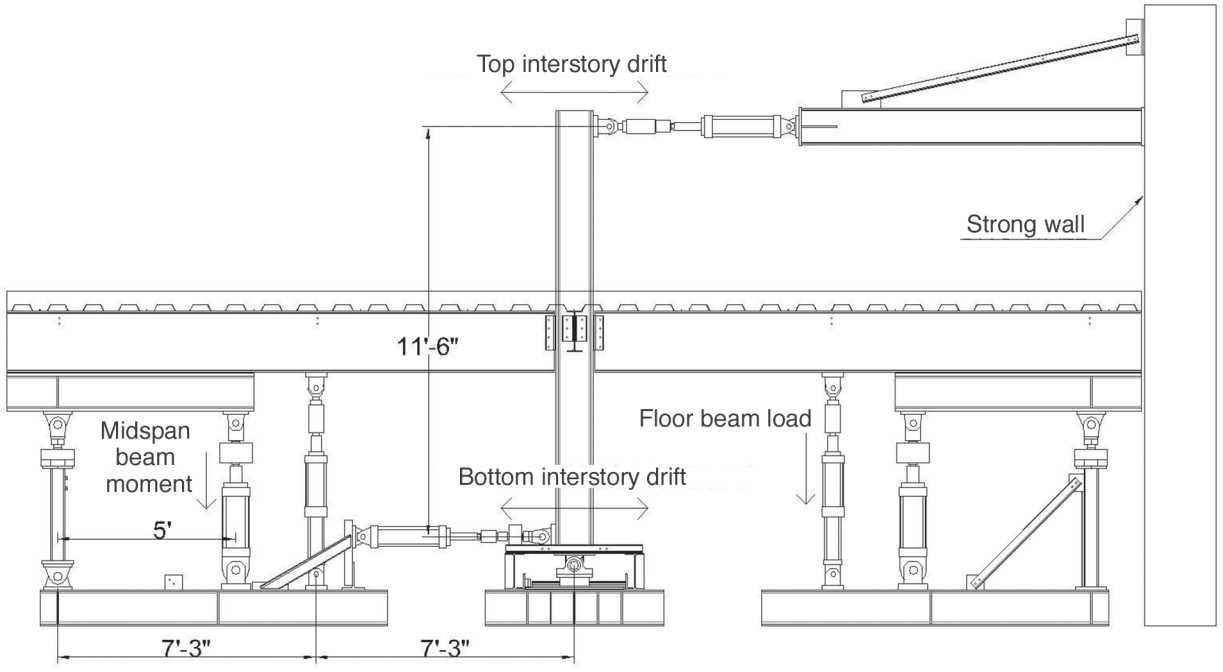

Fig 1. Test set-up.

Table 1. Test Matrix						
Spec. ID	**Number of Bolts**	**Bolt Diameter**	**Angle Size**	**Concrete Slab**	**Deck Rib Orientation**	**Additional Comments**
BS-WB	4[a]	¾ in.	L4×3½×¼	None	N.A.	
BS-BB	4	¾ in.	L4×4×¼	None	N.A.	
S-SC	4	¾ in.	L4×4×¼	N.W.	Par.	
S-LS	4	¾ in.	L4×4×¼	N.W.	Par.	Longitudinal seam in decking at column line
S-HA	6	¾ in.	L4×4×⅝	N.W.	Par.	
W-SC	4	¾ in.	L4×4×¼	N.W.	Perp.	
W-CC	4	¾ in.	L4×4×¼	N.W.	Perp.	Crack control reinforcement at column line
W-RB	4	¾ in.	L4×4×¼	N.W.	Perp.	Ring beam to simulate frame expansion restraint

[a] Angle leg connected to the column is bolted, and angle leg connected to the beam is welded.
N.A. = not applicable; N.W. = normal weight; Par. = ribs parallel to beam; Perp. = ribs perpendicular to beam

mid-height to mid-height of column. The tributary width of the floor slab corresponds to the girder span divided by 4, or 7.25 ft. The vertical actuators closest to the column simulate the gravity loading from each pair of filler beams at those locations. The adjacent actuator and strut assemblies simulate the midspan loading and moment. The gravity loading is applied first and held constant. Then, the actuators at the top and bottom of the column apply equal and opposite displacements to simulate the interstory drifts from a seismic event, following the SAC loading protocol (Clark et al., 1997).

Test Specimens

All specimens have bolted, double-angle shear connections, with the exception of one test specimen for which the angle leg to the column is bolted and the angle leg connected to the beam is welded. Bolts are ¾-in. diameter. Test parameters include angle size, number of bolts, presence of the floor slab with normal-weight concrete, orientation of the metal deck ribs, and other floor slab details. Additional floor slab parameters are used to investigate continuity of the deck and associated tensile capacity of the floor slab, additional tensile capacity in the floor slab from slab reinforcement, and slab confinement simulated by a ring beam to restrain frame expansion. When present, the floor slab has a 6½-in.-thick concrete slab on 20 gage corrugated metal decking with 2-in. ribs; 6×6×2.9 welded wire reinforcement is used for temperature and shrinkage reinforcement. Approximately 25% composite action between the concrete and steel is provided with ¾-in. steel headed stud anchors.

Table 1 provides a summary of the test program. The specimen ID indicates whether it is a bare steel connection (BS), has metal decking oriented in the "strong direction" (S) with the deck ribs parallel to the girder, or has metal decking oriented in the "weak direction" (W) with the deck ribs perpendicular to the beam. For the bare steel connections, WB indicates a welded-bolted angle, and BB indicates a bolted-bolted angle. The bolted-bolted angle is the "standard connection" (SC) for tests with concrete on metal decks, and the metal deck is continuous across the column line. Figure 2 shows a detail of specimen W-SC, an all-bolted, double-angle connection with L4×4×¼ angles, deck ribs perpendicular to the beam, and a continuous deck.

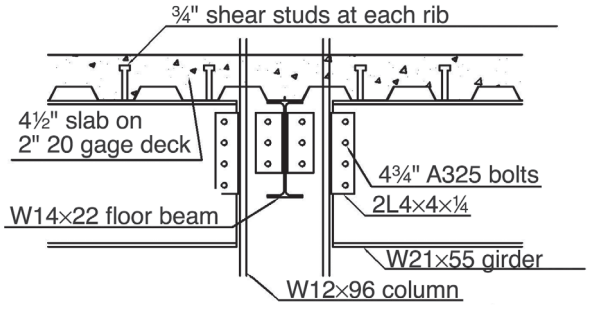

Fig. 2. Detail of specimen W-SC.

Other test specimens include one with a thicker and deeper double-angle connection; specimen S-HA uses a six-bolt connection with L4×4×⅝ angles. S-LS is a test specimen with four-bolt L4×4×¼ angles, deck ribs are parallel, and there is a longitudinal seam in the metal decking at the column line, as shown in Figure 3(a). Specimen W-CC is nominally the same as W-SC but with crack control reinforcement at the column line, a typical detail in steel frame buildings as shown in Figure 3(b). Specimen W-RB has a ring beam around the concrete and metal deck floor to simulate restraint to frame expansion (i.e., beam growth) that might inherently be present in a real building with many bays; the ring beam simulates the confinement to the concrete and is expected to increase the flexural strength of the composite connection.

EXPERIMENTAL RESULTS

Some of the results related to the contribution of the floor slab are highlighted here. The parameters investigated include the deck orientation, the continuity of the deck, reinforcement in the floor slab, and the effects of slab confinement.

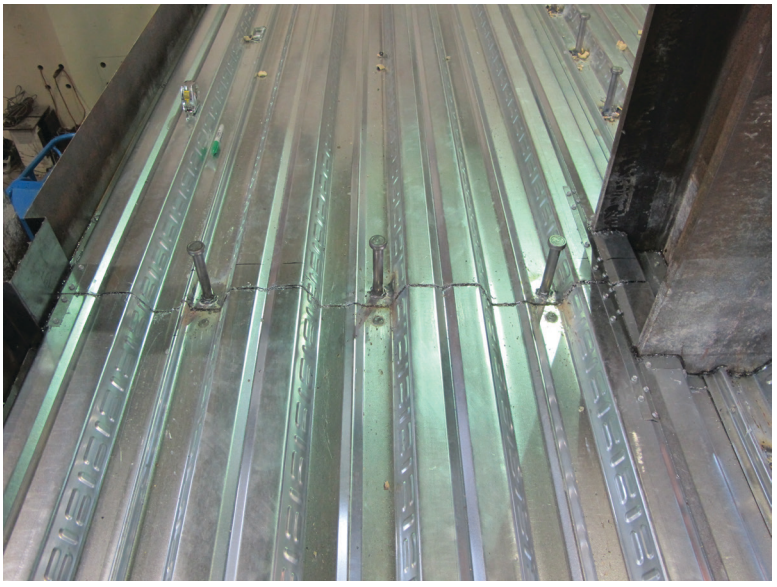

(a)

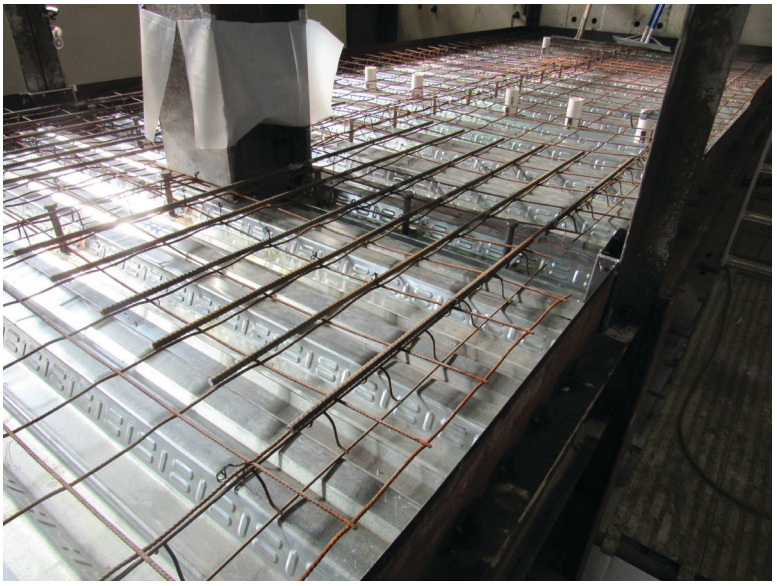

(b)

Fig. 3. Photographs of (a) longitudinal deck seam and (b) crack control reinforcement.

Contribution of the Floor Slab

As observed in previous research (e.g., Liu and Astaneh-Asl, 2000), the floor slab increased the moment capacity of the connection. The composite, standard, strong deck direction connection (S-SC) resisted positive moment through compression in the concrete slab and tension in the angles. The positive moment capacity increased from less than 10% of the girder plastic moment capacity when no floor slab was present (BS-BB) to approximately 25% of the plastic moment capacity of the girder with the concrete slab and metal deck oriented in the strong direction. Concrete crushing governed over the tearing in angles observed for the bare steel specimens and resulted in degradation of the positive moment capacity after 3% drift (Figure 4). The composite, standard, strong deck direction connection (S-SC) initially resisted negative moment through compression in the angle and tension in the metal deck, reaching approximately 20% of the plastic moment capacity of the girder. At about 2.5% drift, binding (or bearing) of the beam bottom flange on the column and tension in the metal deck resulted in moments over 50% of the girder's plastic moment capacity by 4% drift. The connection was able to sustain a similarly large negative moment capacity up to 9% drift, when tearing in the double angles reached almost the entire length of the connection. Comparitively, the bare steel connection (BS-BB) was only able to reach approximately 10% of the girder moment capacity in the negative bending direction, around 5% drift when bottom flange binding occurred. A photo of the BS-BB specimen angle tearing at 9% drift is shown in Figure 5.

Effects of Deck Orientation

Comparisons between the composite, standard, strong deck direction connection (S-SC) and the composite, standard, weak deck direction connection (W-SC) highlighted the importance of the metal deck orientation. Figure 6 shows the normalized moment versus story drift for composite connections with the deck ribs perpendicular and deck ribs parallel. For a positive moment producing compression in the floor slab, the specimen with deck ribs perpendicular (W-SC) was able to develop a capacity of approximately

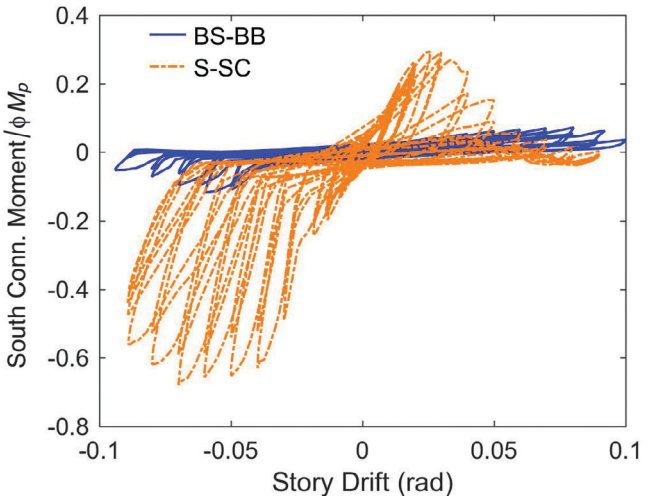

Fig. 4. Comparison of bare steel (BS-BB) and composite test specimen with deck ribs parallel (S-SC); normalized moment vs. story drift.

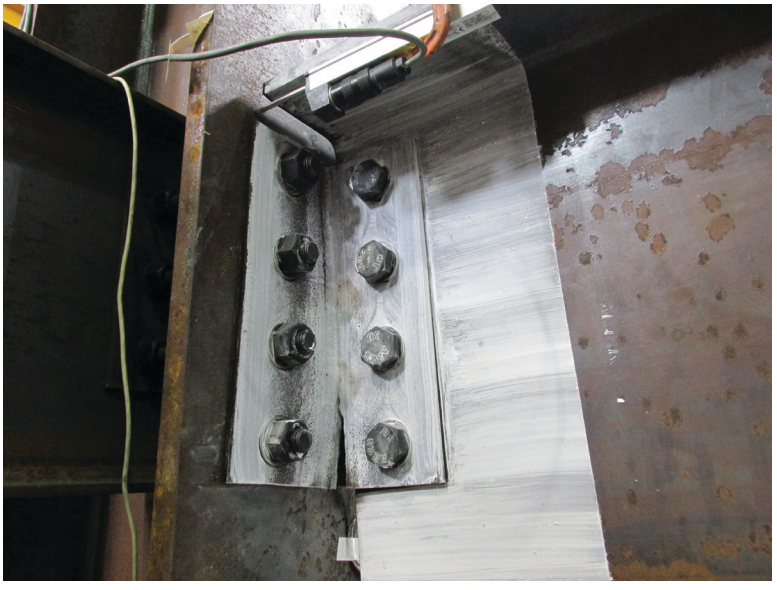

Fig. 5. Tearing in double-angle connection in specimen BS-BB at 9% story drift.

20% of the plastic moment capacity of the girder, compared to 25% for the specimen with deck ribs parallel (S-SC). However, for negative moment, specimen W-SC did not have significant tensile resistance. The concrete cracked, the welded wire reinforcement in the slab fractured, the deck ribs unfolded, and the negative moment capacity was similar to that observed for the bare steel specimen (BS-BB).

Effects of Detailing

Continuity of the metal deck and reinforcement of the floor slab were explored for their effects on the connection moment capacity. Specimen S-LS lacked continuity at the column line, with a longitudinal seam in the metal decking, as shown in Figure 3(a). Specimen W-CC included crack control reinforcement at the column, as shown in Figure 3(b).

In specimen S-LS, the seam was able to transfer some tensile stresses at low drifts but began to fail at the deck-to-beam puddle welds at approximately 2.5% drift. By 5% drift, the negative moment capacity for specimen S-LS had approached that of specimen W-SC, as shown in Figure 7. The higher positive moment capacity for specimen S-LS as compared to specimen W-SC is attributed to the increased contribution of the concrete in compression.

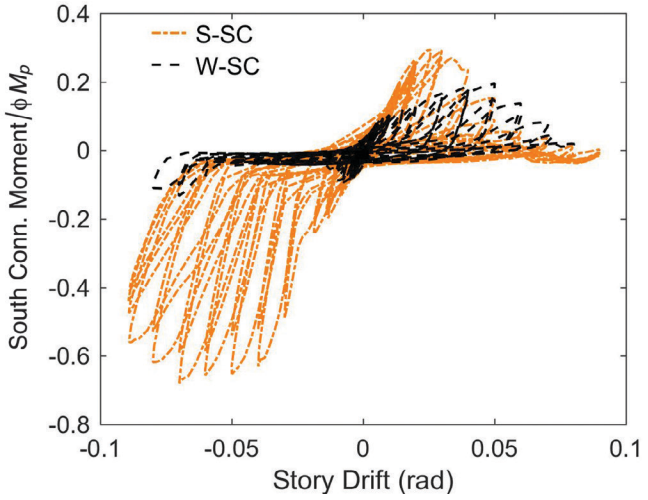

Fig. 6. Comparison of composite test specimens with deck ribs parallel (S-SC) and perpendicular (W-SC); normalized moment vs. story drift.

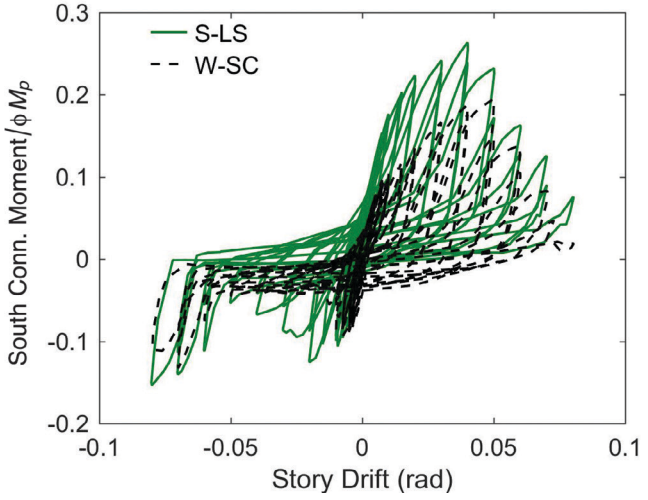

Fig. 7. Comparison of strong direction–longitudinal seam (S-LS) and weak direction composite test specimen (W-SC); normalized moment vs. story drift.

Specimen W-CC was nominally the same as specimen W-SC aside from the crack control reinforcement at the column line. As noted earlier, the weak orientation of the deck resulted in a negative moment capacity for W-SC that was comparable to that of the bare steel specimen. Specimen W-CC did see an initial increase in the negative bending connection resistance. However, cracking in the concrete at the ends of the reinforcement began by 1% drift, and by 3% drift, the reinforcement was considerably less effective in transferring tensile forces. Figure 8 shows a comparison of normalized moment versus story drift for the specimens with and without crack control reinforcement.

Effects of Slab Confinement

In specimen W-RB, a ring beam around the floor slab simulated restraint to frame expansion (i.e., beam growth) that might inherently be present in a real building with many bays. The resulting confinement to the concrete increased the flexural strength of the composite connection. Recall that the standard composite specimen with deck ribs perpendicular (W-SC) had low negative moment capacity relative to the composite specimen with continuous, parallel deck

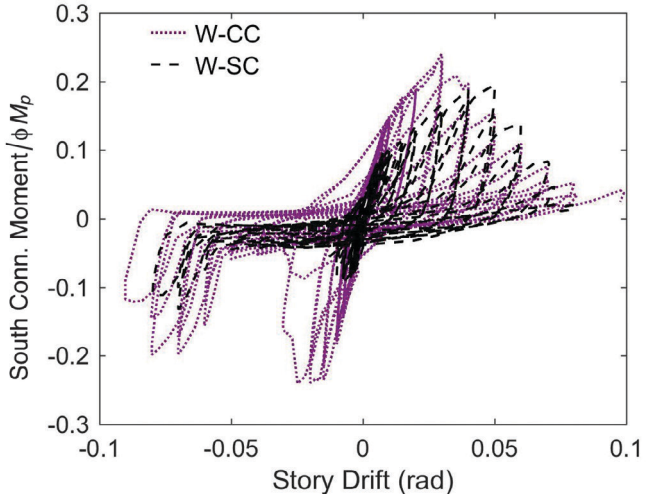

Fig. 8. Comparison of weak direction composite test specimens with and without crack control reinforcement (W-CC and W-SC); normalized moment vs. story drift.

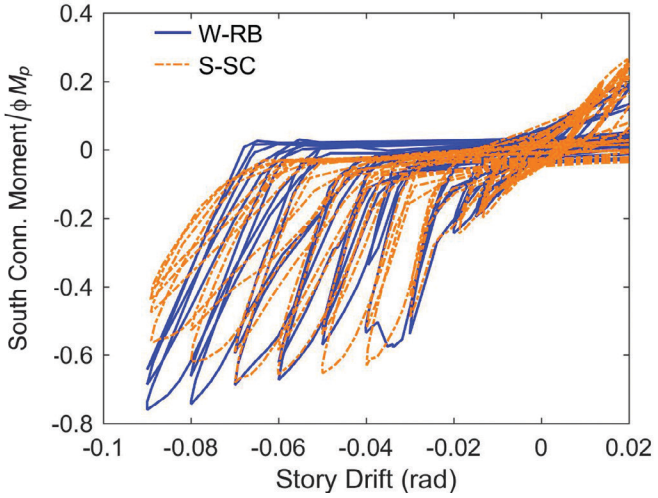

Fig. 9. Comparison of composite test specimens, strong direction (S-SC) and weak direction with ring beam (W-RB); normalized moment vs. story drift.

ribs (S-SC), as shown in Figure 6. Figure 9 shows that with prevention of the frame expansion and deck ribs unfolding in the weak direction, the negative moment capacity of the confined slab specimen (W-RB) approaches that of the specimen with deck ribs continuous and oriented in the strong direction (S-SC).

SUMMARY AND FUTURE WORK

Consistent with findings from previous experimental research programs, these tests have shown that the presence of the composite concrete slab has a major impact on the gravity connection response. Additionally, the direction and detailing of the metal decking has a significant effect on the flexural resistance of the connection. This finding suggests that the additional resistance provided by the presence of the composite slab may not only be attributed to the concrete compressive strength, as was assumed in past studies, but that the tensile resistance of the metal decking plays an important role in the flexural resistance of the connection. These tests also highlighted the importance of the test specimen boundary conditions, particularly related to the effects of unrestrained frame expansion observed in cruciform subassembly test set-ups. When frame expansion is restrained, which may be more representative of the boundary conditions in a multibay gravity framing system, the flexural capacity of the gravity connection can increase significantly.

Ongoing research efforts include development of numerical connection models of varying levels of complexity from more detailed finite element models to simpler component spring-based models. These models will be used to explore system-level behavior, including investigation of restraint to frame expansion in a multibay, multistory system that may affect gravity connection capacity and, ultimately, seismic performance of the steel building.

ACKNOWLEDGMENTS

Special thanks to Dr. Patricia Clayton for her many contributions to this article and to Dr. Michael Engelhardt for the discussions and direction. Funding for the research was provided by the National Science Foundation (Award CMMI 1344592) through the Network for Earthquake Engineering Simulation. Any opinions, findings, conclusions and recommendations presented in this paper are those of the researchers and do not necessarily reflect the views of the sponsor.

REFERENCES

Anderson, J.C., Gourley, B.C., Green, M., Hajjar, J.F., Johnston, R., Leon, R.T., O'Sullivan, D.P. and Partridge, J.E. (1995), "Case Studies of Steel Moment Frame Performance in the Northridge Earthquake of January 17th, 1994," Report SAC 95-07, SAC Joint Venture.

Azizinamini, A. and Radziminski, J. (1989), "Static and Cyclic Performance of Semirigid Steel Beam-to-Column Connections," *Journal of Structural Engineering*, Vol. 115, No. 124.

Clark, P., Frank, K., Krawinkler, H. and Shaw, R. (1997), "Protocol for Fabrication, Inspection, Testing and Documentation of Beam-Column Connection Tests and Other Experimental Specimens," Report SAC/BD-97/02, SAC Steel Project Background Document, October.

Donahue, S., Engelhardt, M., Clayton, P., Williamson, E. and Helwig, T. (2017), "Role of the Floor System in the Cyclic Response of Steel Gravity Framing," 39th IABSE Symposium—Engineering the Future, September 21–23 2017, Vancouver, Canada.

FEMA (2009), "Quantification of Building Seismic Performance Factors," Report FEMA P-695, Federal Emergency Management Agency, Washington, DC.

Flores, F.X., Jarrett, J.A. and Charney, F.A. (2012), "The Influence of Gravity-Only Framing on the Performance of Steel Moment Frames," 15th World Conference on Earthquake Engineering, Lisbon, Portugal, September 24–28, 2012.

Foutch, D.A. (2000), "State of the Art Report on Performance Predication and Evaluation of Steel Moment-Frame Buildings," Report FEMA-355F, Federal Emergency Management Agency, Washington, DC.

Foutch, D.A. and Yun, S.Y. (2002), "Modeling of Steel Moment Frames for Seismic Loads," *Journal of Constructional Steel Research*, Vol. 58, pp. 529–564.

Gupta, A. and Krawinkler, H. (1999), "Seismic Demands for Performance Evaluation of Steel Moment Resisting Frame Structures," Report 132, John A. Blume Earthquake Engineering Center, Stanford University, Stanford, CA, https://stacks.stanford.edu/file/druid:fm826wn5553/TR132_Gupta.pdf.

Krawinkler, H. (2000), "State of the Art Report on Systems Performance of Steel Moment Frames Subject to Earthquake Ground Shaking," Report FEMA-355C, Federal Emergency Management Agency, Washington, DC.

Leon, R.T. (1990), "Semi-Rigid Composite Construction," *Journal of Constructional Steel Research*, Vol. 15, No. 1–2, pp. 99–120.

Liu, J. and Astaneh-Asl, A. (2000), "Cyclic Testing of Simple Connections Including Effects of Slab," *Journal of Structural Engineering*, Vol. 126, No. 1, pp. 32–39.

McKenna, F., Fenves, G.L., Scott, M.H. and Jeremić, B. (2000), "Open System for Earthquake Engineering Simulation," http://opensees.berkeley.edu.

ERRATA

Local Stability of Double-Coped Beams

Bo Dowswell and Robert Whyte

Vol. 51, No. 1, 2014

On page 48, Equations 25 and 26 should be revised to:

$$C_b = \left[3 + \ln\left(\frac{L_b}{d}\right)\right]\left(1 - \frac{d_{ct}}{d}\right) \geq 1.84 \tag{25}$$

$$C_b = \left(\frac{c_b}{c_t}\right)\left[3 + \ln\left(\frac{L_b}{d}\right)\right]\left(1 - \frac{d_{ct}}{d}\right) \geq 1.84 \tag{26}$$

ERRATA

Stability of Rectangular Connection Elements

Bo Dowswell

Vol. 53, No. 4, 2016

The design examples have been revised based on the errata to Dowswell and Whyte (2014), where Equation 25 was revised to:

$$C_b = \left[3 + \ln\left(\frac{L_b}{d}\right)\right]\left(1 - \frac{d_{ct}}{d}\right) \geq 1.84 \qquad (25)$$

REFERENCE

Dowswell, B. and Whyte, R. (2014), "Local Stability of Double-Coped Beams," *Engineering Journal*, AISC, Vol. 51, No. 1.

DESIGN EXAMPLES

Coped Beam Example 1

In this example, the cope buckling strength will be calculated for a double-coped W18×50 beam subjected to shear and axial compression. The cope is 42 in. long × 12 in. deep at both flanges as shown in Figure 16. The beam material is ASTM A992, and the beam is braced laterally by a floor slab at the face of the top-flange cope.

ASTM A992: $F_y = 50$ ksi
W18×50: $t_w = 0.355$ in. $d = 18.0$ in.

Cope length: $c = c_t = c_b = 4\frac{1}{2}$ in.
Cope depth: $d_c = d_{ct} = d_{cb} = 1\frac{1}{2}$ in.

Distance from the face of the cope to the end reaction: $e = 4\frac{1}{2}$ in.

Reduced depth of web, $h_o = 18.0 \text{ in.} - (2)(1\frac{1}{2} \text{ in.}) = 15.0$ in.

The vertical and horizontal reactions are:

LRFD	ASD
$R_u = 90$ kips	$R_a = 60$ kips
$F_{tu} = 120$ kips	$F_{ta} = 80$ kips

The moment at the face of the cope is:

LRFD	ASD
$M_u = R_u e = (90 \text{ kip})(4\frac{1}{2} \text{ in.})$	$M_a = R_a e = (60 \text{ kip})(4\frac{1}{2} \text{ in.})$
= 405 kip-in.	= 270 kip-in.

Flexural Strength

From Dowswell and Whyte (2014), for beams with equal cope lengths at the top and bottom flange, C_b is

$$C_b = \left[3 + \ln\left(\frac{L_b}{d}\right)\right]\left(1 - \frac{d_{ct}}{d}\right) \geq 1.84$$

$$= \left[3 + \ln\left(\frac{4\text{½ in.}}{18.0 \text{ in.}}\right)\right]\left(1 - \frac{1\text{½ in.}}{18.0 \text{ in.}}\right) \geq 1.84$$

$$= 1.84$$

AISC *Specification* Section F11 is used with $C_b = 1.84$, $L_b = c_t = 4\text{½}$ in., $t = t_w = 0.355$ in., and $d = h_o = 15.0$ in. (Dowswell and Whyte, 2014).

$$M_y = (50 \text{ ksi})\left[\frac{(0.355 \text{ in.})(15.0 \text{ in.})^2}{6}\right]$$

$$= 666 \text{ kip-in.}$$

$$M_p = (50 \text{ ksi})\left[\frac{(0.355 \text{ in.})(15.0 \text{ in.})^2}{4}\right] \tag{35}$$

$$= 998 \text{ kip-in.}$$

$$\frac{L_b d}{t^2} = \frac{(4\text{½ in.})(15.0 \text{ in.})}{(0.355 \text{ in.})^2}$$

$$= 536$$

$$\frac{0.08E}{F_y} = \frac{(0.08)(29{,}000 \text{ ksi})}{(50 \text{ ksi})}$$

$$= 46.4$$

$$\frac{1.9E}{F_y} = \frac{(1.9)(29{,}000 \text{ ksi})}{(50 \text{ ksi})}$$

$$= 1{,}100$$

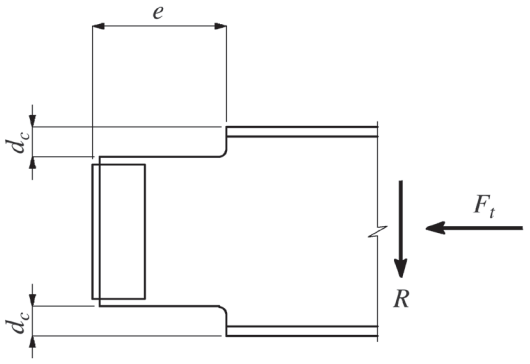

Fig. 16. Coped beam for Examples 1 and 2.

Because $\frac{0.08E}{F_y} < \frac{L_b d}{t^2} < \frac{1.9E}{F_y}$, the nominal flexural strength is:

$$M_n = C_b\left[1.52 - 0.274\left(\frac{L_b d}{t^2}\right)\frac{F_y}{E}\right]M_y \le M_p \tag{36}$$

$$= (1.84)\left[1.52 - (0.274)(536)\left(\frac{50 \text{ ksi}}{29{,}000 \text{ ksi}}\right)\right](666 \text{ kip-in.}) \le 998 \text{ kip-in.}$$

$$= 998 \text{ kip-in.}$$

The available flexural strength is:

LRFD	ASD
$\phi M_n = (0.90)(998 \text{ kip-in.})$ $= 898 \text{ kip-in.}$	$\frac{M_n}{\Omega} = \frac{998 \text{ kip-in.}}{1.67}$ $= 598 \text{ kip-in.}$

Axial Strength

$$A_g = h_o t_w$$

$$= (15.0 \text{ in.})(0.355 \text{ in.})$$

$$= 5.33 \text{ in.}^2$$

$$\frac{KL}{r} = \frac{(0.5)(4\text{½ in.})}{(0.355 \text{ in.})/\sqrt{12}}$$

$$= 22.0 < 25$$

Therefore, according to Specification Section J4.4, the nominal compressive strength is:

$$P_n = F_y A_g \qquad \text{(}Spec\text{. Eq. J4-6)}$$

$$= (50 \text{ ksi})(5.33 \text{ in.}^2)$$

$$= 267 \text{ kips}$$

And the available compressive strength is:

LRFD	ASD
$\phi P_n = (0.90)(267 \text{ kips})$ $= 240 \text{ kips}$	$\frac{P_n}{\Omega} = \frac{267 \text{ kips}}{1.67}$ $= 160 \text{ kips}$

Stability Interaction

When $0.12 < \lambda_y \le 0.33$ ($KL/r \le 25$ for $F_y = 50$ ksi) and $M_n = M_p$, the effects of stability can be neglected, and the interaction equation in AISC *Specification* Section H1.1 is applicable.

LRFD	ASD
$\frac{P_r}{P_c} = \frac{P_u}{\phi P_n}$ $= \frac{120 \text{ kips}}{240 \text{ kips}}$ $= 0.500$	$\frac{P_r}{P_c} = \frac{P_a}{P_n/\Omega}$ $= \frac{80 \text{ kips}}{160 \text{ kips}}$ $= 0.500$

Because $\frac{P_r}{P_c} > 0.2$, *Specification* Section H1.1(a) is applicable,

$$\frac{P_r}{P_c} + \frac{8}{9}\left(\frac{M_{rx}}{M_{cx}}\right) \le 1.0 \tag{53}$$

LRFD	ASD
$0.500 + \frac{8}{9}\left(\frac{405 \text{ kip-in.}}{898 \text{ kip-in.}}\right) = 0.901 < 1.0$	$0.500 + \frac{8}{9}\left(\frac{270 \text{ kip-in.}}{598 \text{ kip-in.}}\right) = 0.901 < 1.0$

Therefore, the cope is adequate for the limit state of local stability.

Coped Beam Example 2

In this example, the cope buckling strength will be calculated for a double-coped W18×50 beam subjected to shear and axial compression. The cope is 18 in. long × 1½ in. deep at both flanges as shown in Figure 16. The beam material is ASTM A992, and the beam is braced laterally by a floor slab at the face of the top-flange cope.

ASTM A992: $F_y = 50$ ksi
W18×50: $t_w = 0.355$ in. $d = 18.0$ in.

Cope length: $c = c_t = c_b = 18$ in.
Cope depth: $d_c = d_{ct} = d_{cb} = 1½$ in.

Distance from the face of the cope to the end reaction: $e = 18$ in.

Reduced depth of web, $h_o = 18.0 \text{ in.} - (2)(1½ \text{ in.}) = 15.0$ in.

The vertical and horizontal reactions are:

LRFD	ASD
$R_u = 15$ kips	$R_a = 10$ kips
$F_{tu} = 45$ kips	$F_{ta} = 30$ kips

The moment at the face of the cope is:

LRFD	ASD
$M_u = R_u e$ $= (15 \text{ kip})(18 \text{ in.})$ $= 270$ kip-in.	$M_a = R_a e$ $= (10 \text{ kip})(18 \text{ in.})$ $= 180$ kip-in.

Flexural Strength

From Dowswell and Whyte (2014), for beams with equal cope lengths at the top and bottom flange, C_b is:

$$C_b = \left[3 + \ln\left(\frac{L_b}{d}\right)\right]\left(1 - \frac{d_{ct}}{d}\right) \geq 1.84$$

$$= \left[3 + \ln\left(\frac{18 \text{ in.}}{18.0 \text{ in.}}\right)\right]\left(1 - \frac{1\text{½ in.}}{18.0 \text{ in.}}\right) \geq 1.84$$

$$= 2.75$$

AISC *Specification* Section F11 is used with $C_b = 2.75$, $L_b = c_t = 18$ in., $t = t_w = 0.355$ in., and $d = h_o = 15.0$ in. (Dowswell and Whyte, 2014).

$$S_x = \frac{(0.355 \text{ in.})(15.0 \text{ in.})^2}{6}$$

$$= 13.3 \text{ in.}^3$$

$$M_p = (50 \text{ ksi})\left[\frac{(0.355 \text{ in.})(15.0 \text{ in.})^2}{4}\right]$$

$$= 998 \text{ kip-in.}$$

$$\frac{L_b d}{t^2} = \frac{(18 \text{ in.})(15.0 \text{ in.})}{(0.355 \text{ in.})^2}$$

$$= 2{,}140$$

$$\frac{1.9E}{F_y} = \frac{(1.9)(29{,}000 \text{ ksi})}{(50 \text{ ksi})}$$

$$= 1{,}100$$

Because $\frac{1.9E}{F_y} < \frac{L_b d}{t^2}$, the critical stress is:

$$F_{cr} = \frac{1.9EC_b}{\frac{L_b d}{t^2}} \tag{38}$$

$$= \frac{(1.9)(29{,}000 \text{ ksi})(2.75)}{2{,}140}$$

$$= 70.8 \text{ ksi}$$

And the nominal flexural strength is:

$$M_n = F_{cr} S_x \leq M_p \tag{37}$$

$$= (70.8 \text{ ksi})(13.3 \text{ in.}^3) \leq 998 \text{ kip-in.}$$

$$= 942 \text{ kip-in.}$$

The available flexural strength is:

LRFD	ASD
$\phi M_n = (0.90)(942 \text{ kip-in.})$ $= 848 \text{ kip-in.}$	$\frac{M_n}{\Omega} = \frac{942 \text{ kip-in.}}{1.67}$ $= 564 \text{ kip-in.}$

Axial Strength

$$A_g = h_o t_w$$
$$= (15.0 \text{ in.})(0.355 \text{ in.})$$
$$= 5.33 \text{ in.}^2$$

$$\frac{KL}{r} = \frac{(0.5)(18 \text{ in.})}{(0.355 \text{ in.})/\sqrt{12}}$$
$$= 87.8 > 25$$

Therefore, the axial strength will be calculated according to AISC *Specification* Chapter E. The elastic buckling stress is:

$$F_e = \frac{\pi^2 E}{\left(\frac{KL}{r}\right)^2} \quad \text{(Spec. Eq. E3-4)}$$
$$= \frac{\pi^2 (29{,}000 \text{ ksi})}{(87.8)^2}$$
$$= 37.1 \text{ ksi}$$

The slenderness parameter is:

$$4.71\sqrt{\frac{E}{F_y}} = 4.71\sqrt{\frac{29{,}000 \text{ ksi}}{50 \text{ ksi}}}$$
$$= 113$$

Because $\frac{KL}{r} < 4.71\sqrt{\frac{E}{F_y}}$, the critical buckling stress is calculated using AISC *Specification* Equation E3-2:

$$F_{cr} = \left[0.658^{\left(\frac{F_y}{F_e}\right)}\right] F_y$$
$$= \left[0.658^{\left(\frac{50 \text{ ksi}}{37.1 \text{ ksi}}\right)}\right] (50 \text{ ksi})$$
$$= 28.4 \text{ ksi}$$

And the nominal compressive strength is:

$$P_n = F_{cr} A_g \quad \text{(Spec. Eq. E3-1)}$$
$$= (28.4 \text{ ksi})(5.33 \text{ in.}^2)$$
$$= 151 \text{ kips}$$

The available compression strength is:

LRFD	ASD
$\phi P_n = (0.90)(151 \text{ kips})$ $= 136 \text{ kips}$	$\frac{P_n}{\Omega} = \frac{151 \text{ kips}}{1.67}$ $= 90.4 \text{ kips}$

Stability Interaction

When $0.33 < \lambda_y$ ($KL/r > 25$ for 50 ksi) or $M_n < M_p$, the effects of stability must be included in the design, and the interaction equation in AISC *Specification* Section H2 is applicable. Due to the high flexural stiffness in the strong-axis direction, the strong-axis second-order moment is neglected.

$$\frac{P_r}{P_c} + \frac{M_{rx}}{M_{cx}} \le 1.0 \qquad \text{(from Eq. 57)}$$

LRFD	ASD
$\frac{45 \text{ kip}}{136 \text{ kip}} + \frac{270 \text{ kip-in.}}{848 \text{ kip-in.}} = 0.649 < 1.0$	$\frac{30 \text{ kip}}{90.4 \text{ kip}} + \frac{180 \text{ kip-in.}}{564 \text{ kip-in.}} = 0.651 < 1.0$

Therefore, the cope is adequate for the limit state of local stability.

Coped Beam Example 3

In this example, the cope buckling strength will be calculated for a double-coped W18×50 beam subjected to shear and axial tension. The cope is 18 in. long × 1½ in. deep at both flanges as shown in Figure 17. The beam material is ASTM A992, and the beam is braced laterally by a floor slab at the face of the top-flange cope.

ASTM A992: $F_y = 50$ ksi
W18×50: $t_w = 0.355$ in. $\quad d = 18.0$ in.

Cope length: $c = c_t = c_b = 18$ in.
Cope depth: $d_c = d_{ct} = d_{cb} = 1½$ in.

Distance from the face of the cope to the end reaction: $e = 18$ in.

Reduced depth of web, $h_o = 18.0 \text{ in.} - (2)(1½ \text{ in.}) = 15.0$ in.

The vertical and horizontal reactions are:

LRFD	ASD
$R_u = 21$ kips	$R_a = 14$ kips
$F_{tu} = 120$ kips	$F_{ta} = 80$ kips

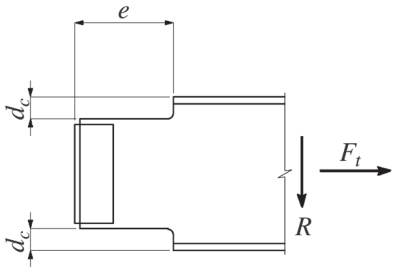

Fig. 17. Coped beam for Example 3.

The moment at the face of the cope is:

LRFD	ASD
$M_u = R_u e$ $= (21 \text{ kip})(18 \text{ in.})$ $= 378 \text{ kip-in.}$	$M_a = R_a e$ $= (14 \text{ kip})(18 \text{ in.})$ $= 252 \text{ kip-in.}$

Flexural Strength

From Dowswell and Whyte (2014), for beams with equal cope lengths at the top and bottom flange, C_b is

$$C_b = \left[3 + \ln\left(\frac{L_b}{d}\right)\right]\left(1 - \frac{d_{ct}}{d}\right) \geq 1.84$$
$$= \left[3 + \ln\left(\frac{18 \text{ in.}}{18.0 \text{ in.}}\right)\right]\left(1 - \frac{1\text{½ in.}}{18.0 \text{ in.}}\right) \geq 1.84$$
$$= 2.75$$

AISC *Specification* Section H1.2 will be used to calculate the effect of the tension load on the lateral-torsional buckling strength.

$$I_y = \frac{h_o t_w^3}{12}$$
$$= \frac{(15.0 \text{ in.})(0.355 \text{ in.})^3}{12}$$
$$= 0.0559 \text{ in.}^4$$

$$P_{ey} = \frac{\pi^2 E I_y}{L_b^2} \tag{56}$$
$$= \frac{\pi^2 (29{,}000 \text{ ksi})(0.0559 \text{ in.}^4)}{(18 \text{ in.})^2}$$
$$= 49.4 \text{ kips}$$

According to Equation 55, $C_b' = C_b\sqrt{1 + \frac{\alpha P_r}{P_{ey}}}$:

LRFD	ASD
$C_b' = 2.75\sqrt{1 + \frac{(1.0)(120 \text{ kips})}{49.4 \text{ kips}}}$ $= 5.09$	$C_b' = 2.75\sqrt{1 + \frac{(1.6)(80 \text{ kips})}{49.4 \text{ kips}}}$ $= 5.21$

AISC *Specification* Section F11 is used with $C_b = 5.09$ (LRFD), $C_b = 5.21$ (ASD), $L_b = c_t = 18$ in., $t = t_w = 0.355$ in., and $d = h_o = 15.0$ in. (Dowswell and Whyte, 2014).

$$S_x = \frac{(0.355 \text{ in.})(15.0 \text{ in.})^2}{6}$$
$$= 13.3 \text{ in.}^3$$

$$M_p = (50 \text{ ksi})\left[\frac{(0.355 \text{ in.})(15.0 \text{ in.})^2}{4}\right]$$
$$= 998 \text{ kip-in.}$$

$$\frac{L_b d}{t^2} = \frac{(18 \text{ in.})(15.0 \text{ in.})}{(0.355 \text{ in.})^2}$$
$$= 2{,}140$$

$$\frac{1.9E}{F_y} = \frac{(1.9)(29{,}000 \text{ ksi})}{(50 \text{ ksi})}$$
$$= 1{,}100$$

Because $\frac{1.9E}{F_y} < \frac{L_b d}{t^2}$, the critical stress is:

LRFD	ASD
$F_{cr} = \frac{1.9EC_b'}{\frac{L_b d}{t^2}}$ $= \frac{(1.9)(29{,}000 \text{ ksi})(5.09)}{2{,}140}$ $= 131 \text{ ksi}$	$F_{cr} = \frac{1.9EC_b'}{\frac{L_b d}{t^2}}$ $= \frac{(1.9)(29{,}000 \text{ ksi})(5.21)}{2{,}140}$ $= 134 \text{ ksi}$

The nominal flexural strength is:

$$M_n = F_{cr} S_x \le M_p \quad (37)$$
$$= (131 \text{ ksi})(13.3 \text{ in.}^3) \le 998 \text{ kip-in.}$$
$$= 998 \text{ kip-in.}$$

The available flexural strength is:

LRFD	ASD
$\phi M_n = (0.90)(998 \text{ kip-in.})$ $= 898 \text{ kip-in.}$	$\frac{M_n}{\Omega} = \frac{998 \text{ kip-in.}}{1.67}$ $= 598 \text{ kip-in.}$

Axial Strength

$$A_g = h_o t_w$$
$$= (15.0 \text{ in.})(0.355 \text{ in.})$$
$$= 5.33 \text{ in.}^2$$

The nominal tensile strength is:

$$P_n = F_y A_g$$
$$= (50 \text{ ksi})(5.33 \text{ in.}^2)$$
$$= 267 \text{ kips}$$

The available tensile strength is:

LRFD	ASD
$\phi P_n = (0.90)(267 \text{ kips})$ $= 240 \text{ kips}$	$\frac{P_n}{\Omega} = \frac{267 \text{ kips}}{1.67}$ $= 160 \text{ kips}$

Interaction

For axial tension loads with $M_n = M_p$, plastic interaction according to Equation 62 is applicable.

$$\left(\frac{P_r}{P_c}\right)^2 + \frac{M_{rx}}{M_{cx}} \le 1.0$$

LRFD	ASD
$\left(\frac{120 \text{ kip}}{240 \text{ kip}}\right)^2 + \frac{378 \text{ kip-in.}}{898 \text{ kip-in.}} = 0.671 < 1.0$	$\left(\frac{80 \text{ kip}}{160 \text{ kip}}\right)^2 + \frac{252 \text{ kip-in.}}{598 \text{ kip-in.}} = 0.671 < 1.0$

Therefore, the cope is adequate for the limit state of local stability.

Guide for Authors

Scope

Engineering Journal is dedicated to the improvement and advancement of steel construction. Its pages are open to all who wish to report on new developments or techniques in steel design, research, the design and/or construction of new projects, steel fabrication methods, or new products of significance to the uses of steel in construction. Only original papers should be submitted.

General

Papers intended for publication should be submitted by email Margaret Matthew, Editor, at matthew@aisc.org.

The articles published in the *Engineering Journal* undergo peer review before publication for (1) originality of contribution; (2) technical value to the steel construction community; (3) proper credit to others working in the same area; (4) prior publication of the material; and (5) justification of the conclusion based on the report.

All papers within the scope outlined above will be reviewed by engineers selected from among AISC, industry, design firms, and universities. The standard review process includes outside review by an average of three reviewers, who are experts in their respective technical area, and volunteers in the program. Papers not accepted will not be returned to the author. Published papers become the property of the American Institute of Steel Construction and are protected by appropriate copyrights. No proofs will be sent to authors. Each author receives three copies of the issue in which his contribution appears.

Manuscripts

Manuscripts must be provided in Microsoft Word format. Include a PDF with your submittal so we may verify fonts, equations and figures. View our complete author guidelines at **www.aisc.org/ej**.

Smarter. Stronger. Steel.

Engineering Journal
American Institute of Steel Construction
130 E Randolph St., Ste. 2000, Chicago, IL 60601
312.670.2400 | www.aisc.org